NOVEL CONCEPTS IN PHASE SHIFITING INTERFEROMETRY AND THEIR APPLICATIONS TO HOLOGRAPIC MOIRÉ

THÈSE N$^{\text{O}}$ 3597 (2006)

PRÉSENTÉE LE 27 JUILLET 2006
À LA FACULTÉ DE L'ENVIRONNEMENT NATUREL, ARCHITECTURAL ET CONSTRUIT
Laboratoire d'informatique et de mécanique appliquées à la construction
SECTION GÉNIE CIVIL

ÉCOLE POLYTECHNIQUE FÉDÉRALE DE LAUSANNE

POUR L'OBTENTION DU GRADE DE DOCTEUR ÈS SCIENCES

PAR

Abhijit PATIL

Master of technology in electrical engineering, Indian Institute of Technology, Bombay, Inde
de nationalité indienne

acceptée sur proposition du jury:

Prof. M. Hirt, président du jury
Prof. P. Rastogi, directeur de thèse
Prof. A. Ijspeert, rapporteur
Dr E. Hack, rapporteur
Prof. A. Poggialini, rapporteur

ÉCOLE POLYTECHNIQUE
FÉDÉRALE DE LAUSANNE
Lausanne, EPFL
2006

Abstract

To date, no phase shifting technique has been implemented that accommodates the requirements inherent in holographic moiré . In the present form of measurement, only the value of one component of difference in displacement carried on moiré is quantified, whereas information carried on the carrier is lost. However, in several interferometers, incorporation of this information would add value to the systems as in many applications the capacity for registering simultaneously information carried on moiré and on carrier is essential. A technique capable of achieving this objective represents a substantial advancement in phase shifting as it would circumvent limitations exhibited by the present crop of phase shifting techniques of measuring only one displacement component at any given instant of time.

The aim of this work is to design novel phase shifting algorithms which would add the capability to measure simultaneously values of displacement components carried on the moiré and on the carrier. The proposed research thus envisages developing new concepts in phase shifting and imparting stimulus to the measurement techniques in comparative holographic moiré which in spite of having immense potential have largely remained unexploited because of the unavailability of powerful data-analysis techniques.

The introduction of high-resolution methods for the first time in phase shifting interferometry and their ability to successfully estimate multiple phase information in holographic moiré are among the salient features of this research.

Keywords: Interferometry, Holography interferometry, Holographic moiré, Phase measurement, High resolution methods

Résume

A ce jour, aucune technique de déphasage applicable aux spécifications inhérentes au moiré holographique n'a été mise en oeuvre. Sous la forme actuelle des mesures, seule la valeur d'une composante de diffrence dans le déplacement obtenue par moiré est quantifiée, alors que d'autres informations véhiculée par l'interferogramme est perdue. Cependant, dans plusieurs interféromtres, l'incorporation de cette information amènerait une valeur ajoutée aux systèmes étant donné que, dans multiples applications, la capacité d'enregistrer simultanément l'ensemble d'information véhiculée par la figure de moiré est essentielle. Une technique capable d'atteindre cet objectif représente une avancée substantielle dans le décalage de phase car elle circonviendrait les limites démontrées par les techniques de déphasage présentes qui ne mesurent seulement qu'une composante de déplacement à un instant de temps donné.

Le but de ce travail de recherche est de concevoir de nouveaux algorithmes de déphasage qui permettraient de mesurer simultanément les composantes de déplacement véhiculées par la figure de moiré .

La recherche proposée envisage de développer de nouveaux concepts dans le décalage de phase afin de redonner un nouvel essor aux techniques de mesures par moiré holographique comparatif, qui en dépit de leur immense potentiel, sont restées en grande partie inexploitées en raison de l'absence de techniques d'analyses de données efficaces.

Pour la première fois dans l'interféromtrie de décalage de phase, l'introduction de méthodes à haute résolution et leur capacité d'estimer avec succès des informations de phases multiples dans le moiré holographique sont parmi les éléments notables de cette recherche.

Mots clés: Interférométrie, Interférométrie holographique, Moiré holographique, Mesure de phase, Méthodes haute résolution

Acknowledgements

Before I acknowledge those who are directly involved in the successful completion of this PhD work, I would like to thank my secondary school teachers without whom I would not have come to this stage. My special thanks goes to PGT teacher S. P. John for teaching me mathematics and PGT teacher K. Basavraj for teaching me science. My special thanks also goes to Prof. P. C. Pandey, IIT Bombay and Prof. C. P Gadgil, IIT Bombay, for always inspiring me and showing confidence in my abilities. I had fruitful discussions with them before joining the PhD program. I am highly indebted to Prof. P. C. Pandey for supervising my masters dissertation, where I actually started organizing myself and understood how the research needs to be carried out. He also taught me for the first time how to write a technical report and which has substantially helped me in writing journal papers and of course this thesis.

I would like to very sincerely thank Prof. Pramod Rastogi, my thesis supervisor, for his many suggestions and constant support during this research. The thesis topic is in fact the continuation of work initially pursued by him in the early and mid 90's. I am highly indebted to him for his constant encouragement and moral support during the research work. Professor Rastogi supplied me with the preprints of some of his research work and suggested me to develop novel algorithms which will break through the limitation of the use of single phase shifting devices hitherto imposed on phase shifting interferometry. He always showed interest in new ideas and was patient enough to give me time even during my initial failures in the research. He was quick to understand my weaknesses and suggested me to channelize my efforts in the areas where I could contribute more effectively. I would also like to thank him for spending weekends and many evenings in correcting journal papers and technical reports.

I would like to thank Mr. Patrice Gallay for preparing a high precision mechanical assembly for conducting the experiments. I would like to thank my colleague Rajesh Langoju for providing me many useful insights while designing novel algorithms.

I would like to thank the Swiss National Science Foundation for supporting me with a research grant for the period 2002-2006. I would also like to thank Prof. Ian Smith for allowing me to conduct research at IMAC.

Finally, I am grateful to my parents, brother, wife, and little daughter Vedika for their patience and encouragement throughout the research work. I owe a lot to them for their support and understanding through this period which saw me working late nights and on weekends.

Table of Contents

List of Figures

List of Tables

Chapter 1

Moving ahead with Phase

1.1 Introduction

The classical experiment by Thomas Young in 1801 to show the interference phenomenon between two wavefronts has contributed significantly to various fields of engineering and sciences. Human ingenuity combined with technological advances in electronics, information storage, and optical and image processing have led to exploring the coherent processing of the interference beams where in the majority of cases, the quantity of immense importance is the phase of the interference beams which is known to carry the key information. For instance, physical quantities such as the surface profile in interferometry, wavefront distortion in adaptive optics [4–6], temperature distribution in an oil bath [7], the degree of magnetic field inhomogeneity in water/fat separation problem of magnetic resonance imaging [8], and seismic processing [9] are related to the phase of the interference beams. Areas of interest to engineers such as measurements and non destructive testing of components have also relied heavily on the determination of phase [10–33].

Over the years several concepts have been developed for measuring the phase information. For instance, inclusion of phase shifting procedures, in interferometry has strengthened this technique by enabling measurements and testing with high accuracy ranging between a fraction of a micron to a few nanometers [34]. This development has also led to the real time implementation and automation of interferometers. Phase shifting interferometry (PSI) has primarily been applied [35] for measuring surface flatness of plano elements such as mirrors, prisms etc., for measuring surface roughness, strain, deformation, displacement, vibrations, and even to optimize the design in manufacturing industry. Researchers in companies, such as, Optical Systems Engineering and Ford Motor Co. have demonstrated that experimental measurements using phase shifting interferometry techniques when complemented by computer-aided engineering can optimize the product design [36]. The next section discusses in detail the various phase measurement approaches.

1.2 State-of-the-art in Phase Measurement

The need to measure phase accurately has led to adapting different viewpoints in its measurement. Considered broadly, the phase of the interfering beams can be processed by either spatial or temporal techniques. In spatial techniques a single interferogram is sufficient to extract the phase information by applying spatially the signal processing tools such as Fourier transform and wavelet transform to process the spatially modulated data. Whereas in temporal techniques a series of data frames are acquired to compute the phase. Both these techniques are effective in estimating the phase. Whether it is spatial or temporal technique, each have their typical limitations. Their selection is mainly made on the basis of the users familiarity with these techniques, available resources, and desired accuracy in the measurement of phase. The following subsections provide an overview of these techniques.

1.2.1 Spatial Technique

Fourier transform technique functions by transforming the intensity data into the Fourier domain. Fringe analysis using this technique involves the addition of carrier fringe to the intensity data in order to separate the zero-order spectrum corresponding to the background intensity from the first-order spectrum, which typically carries the phase information. The phase information is then computed by processing the first-order spectrum. Unfortunately, the Fourier transform technique is basically a global frequency transformation technique and the signal in one position affects the signal in other positions during the spectral analysis. In addition, the discontinuity in the spatial fringe pattern causes the sidelobes to expand into the entire frequency domain. This problem can exacerbate further if a finite size of the filter is applied to isolate the sidelobes. To address this concern, wavelet transform has been introduced which also allows for direct phase demodulation by doing away with the need for phase unwrapping [37]. However, this technique has met with limited success because of the need to add carrier fringes in both the horizontal and vertical directions. If the fringes are added in the horizontal direction, only one dimensional wavelet transform is possible. Moreover, the need to introduce an optimization algorithm to minimize the wavelet ridge is one of the potential bottlenecks in accessing its optimal performance. Recently, Kemao [38–40] has demonstrated through several illustrations that a fringe pattern processed locally or block by block using windowed Fourier transform (WFT) method removes artifacts in phase measurements as compared to the simple carrier based Fourier transform method. The author has further shown an elegant comparison of the WFT method with various other spatial techniques that have been applied to phase measurements, such as, windowed Fourier ridges, wavelet transform, and regularized phase tracking. Presently, WFT appears to be a promising tool among the spatial techniques for phase measurement.

1.2.2 Temporal Technique

A research in parallel has also developed over the years by which the phase is extracted by acquiring more than one data frame. The technique functions primarily by acquiring a number of intensity images with phase increments between successive frames. The phase increment correspond to the relative change in the phase difference between the object and the reference beams. These phase increments can typically be obtained in various ways such as by the frequency modulation of the laser diodes, or by a ferroelectric liquid-crystal and a combination of quarter and half- wave plates, or by a piezoelectric device (PZT). Temporal techniques for extracting phase are known to offer advantages over the spatial techniques in terms of improved noise immunity, high-spatial-frequency resolution, and insensitivity to spatial variations in the detector response.

Given the advantages possessed by the temporal techniques, efforts have been mounted to apply temporally the well known spatial techniques, such as the Fourier transform. Goldberg *et al.* [41] have shown that the phase steps could be estimated globally if the Fourier transform were to be applied temporally. In such a spatio-temporal method, the global phase step is estimated by comparing the phase of the first-order maximum of one of the interferograms in the Fourier domain to the first-order maximum of the subsequent interferogram. Once the phase steps between successive data frames have been determined, the least squares fit technique is applied for phase measurement. This method however, is highly dependent on the distribution of the zeroth- and the first-order spectrum. In such a case, the selection of higher carrier frequency to separate spectral components would seem to be a solution but its feasibility is limited by the spectral resolution of the detectors. The method is also sensitive to noise occurring during the acquisition of successive data frames. To overcome this problem, Guo *et al.* [42] have suggested an algorithm based on energy-minimum for estimating the global phase steps between the frames. Although this algorithm is less sensitive to noise, it is iterative and requires an initial guess for minimizing the energy. Moreover, both these concepts assume that the phase step is uniform over the entire data frame. These methods also require the addition of carrier fringes.

Before discussing the well known contemporary algorithms based on temporal techniques, it would be worthwhile to summarize the various methods by which phase shifts can be produced. As stated earlier, one of the ways by which the phase shifts can be realized is by varying the injection current and/or the temperature of the active regions in the laser diode. By doing so, the laser diode frequency can be changed [43–47]. An increase of current, however, gives rise to an increase of the power of the laser diode, which violates the assumption of constant intensity in the phase extraction algorithm [44]. Tatsuno *et al.* [45], have shown that the use of a photodiode can minimize this problem; while Ishii *et al.* [43] have proposed a numerical approach to minimize the variation in intensity. Another approach which has been suggested [46] uses an amplitude stabilizer with the objective to stabilize the laser diode source. A computational approach has also been proposed [44] in which six-data frames are shown to be sufficient to extract phase in the presence of changes in laser power. Recently, a stabilized closed-loop phase shifting interferometer [48] has been proposed that uses direct frequency modulation of laser. The interferometer is servo controlled in the phase domain, and the optical phases are detected by two-frequency optical heterodyning. Although the proposed concept offers both phase shifting and fringe stabilization simultaneously, the interferometer requires a large amount of instrumentation to be incorporated and hence does not seem to provide a cost effective solution for phase extraction. Bitou *et al.* [47] have shown that frequency tunable laser diode and a Fabry-Perot cavity in an interferometer can yield a high degree of equality in the phase steps. It would be worth noting here that a necessary condition for the algorithms proposed by Carré [49] and by Stoilov and Dragostinov [50] to work requires the use of equal phase steps.

Recently, a switchable phase shifter has been proposed [51] that uses a pair of ferroelectric liquid-crystal devices with nominal retardations of quarter wave and a switching angle of 45° to produce a phase shifts of 0° and ±90°. The advantage of the proposed concept lies in the fact that the phase shifts of 0° and ±90° are almost independent of the wavelength over the visible range of 450nm to 700nm. Phase shifts have also been produced through non-mechanical phase shifting devices such as quarter-wave plates and polarizers [52], or through a combination of polarizers, waveplates and a liquid crystal retarder [34], or through mechanical gratings [53]. Ngoi *et al.* [52] have proposed instantaneous phase shifting in which where a near common path is achieved between the object and the reference beams. This method is shown to be immune to the vibration if the vibration frequency is lower than the typical data acquisition rate. A method based on a similar approach has also been proposed by Smythe and Moore [54]. However, one of the common problems associated with some of the configurations involving common path interferometers has been to separate the reference and the object beams.

Kwon [53] exploited the diffraction phenomenon of the grating and proposed a point diffraction interferometer for a real time phase analysis. In this case, the diffraction order is found to contain the desired phase shifts. The intensity equations corresponding to the three phase shifts can then be solved to yield the phase. Mercer [55] *et al.* have proposed a different approach in point diffraction interferometer by which the phase shifts are imparted by embedding a microsphere in a thin liquid-crystal layer. The microsphere yields reference beams while the liquid-crystal layer induces a variable phase shift. On the other hand, Medecki *et al.* [56] also proposed a point diffraction interferometer in which the beam from the object under study is split into two beams with a small angular separation created by a grating. The zero-order beam is focused on to a pin-hole and acts as a reference beam while the first-order beam is allowed to pass through a slightly bigger hole than the pin hole. The phase shift in this case is created by laterally shifting the grating. Huang *et al.* [57], Su and Shyu [58], and Morris *et al.* [34] have also proposed a point diffraction interferometer with slight modifications in the optical elements so that variable phase shifts can be produced. Particularly interesting is the method suggested by Morris *et al.* in which phase shifting is achieved by exploiting the polarization characteristics of a birefringent scatterplate. In this method, a birefringent scatterplate along with polarizers and a quarter-wave plate produces two beams with orthogonal polarizations. A variable phase shift can then be induced between these two beams by a liquid crystal retarder.

Inspite of the presence of a large number of phase shifting elements, the one device which has caught the attention of the researchers is the piezoelectric device, commonly known as PZT (acronym for Lead Zirconate Titanate). PZT is a ceramic perovskite material that shows a piezoelectric effect. Piezoelectricity is the ability of certain crystals to generate a voltage in response to applied mechanical stress. Piezoelectric materials also show the opposite effect, called converse piezoelectricity, by which the application of an electrical field creates a mechanical deformation in the crystal. A deformation of about 0.1% of the original dimension can yield displacements of the orders of nanometers [59].

Unfortunately, the PZT is also one of the major sources of errors in phase measurement. In practice, this device exhibits a non-linear response to the applied voltage and also a mechanical vibration during its translation. In addition, the device has the characteristics of non-repeatability, and suffers from ageing-effect. One of the most common errors during its usage is the so-called miscalibration error [60]. To make the matters worse, the device is known to be sometimes responsible for the presence of higher order harmonics in the recorded fringe intensity [60, 61].

Numerous algorithms have been designed which aim at minimizing the errors arising due to the PZT and also those arising due to vibrations, stray reflections, temperature fluctuations, quantization errors in the intensity, etc. Although three frames are normally sufficient for estimating the phase, it has now become a well established fact that additional data frames need to be acquired to minimize the effect of various systematic [60–72] and random errors [**?**, 73–77]. The use of large number of data frames has been shown to decrease the sensitivity to these errors. These algorithms in general can be broadly classified to fall into two categories: conventional and generalized. While the step widths are typically multiples of $\pi/2$, in the former case, these are arbitrary phase values in the latter case [78, 79]. As far as the conventional techniques are concerned, several algorithms have been reported to compensate for errors that are introduced during phase evaluation. Most of these algorithms aim at minimizing the errors arising due to the nonlinear characteristic inherent in the piezoelectric device. These algorithms termed as self-compensating [49, 64–66] have proved to be effective in compensating deterministic phase shift error, and in compensating even second [80–82] order nonlinearities. Some of these algorithms minimize the effect of other systematic errors such as optical system aberrations [72,83], parasitic fringes [62, 84], photodetection errors [82, 85] and quantization errors [71, 86]. Random errors due to thermal or shot noise have also been observed to influence the phase measurement [74]. Random errors in measurement of phase can also crop up because of turbulent and laminar air flows in the optical path [85], vibrations [73, 75, 80], electronic noise [87] originating in the photodetection during amplification, and optical noise commonly known as speckle [88]. The statistical properties of phase-shift algorithms have been investigated for the case of additive Gaussian intensity noise. It has been shown that some advanced systematic-error-compensating algorithms are sensitive to random noise [74]. The error in phase measurement can also arise if the fringe profile is not purely sinusoidal because of detector nonlinearity or multiple-beam interference. The algorithm proposed by Hibino *et al.* [61] offers the possibility of reducing calibration errors in the presence of higher order harmonics. Hibino *et al.* [61] and Surrel [60] have shown that $2\kappa + 3$ and $2\kappa + 2$ samples are, respectively, necessary to minimize the effect of the κ^{th} order harmonic, with the phase step of $2\pi/(\kappa + 2)$ between two successive samples. The restriction on the free use of phase steps represents a drawback and a possible limitation for the methods wide spread application.

While conventional phase shifting has demonstrated its ability to overcome various sources of systematic errors, generalized phase shifting technique though flexible as far as the selection of phase steps is concerned hasn't been successful in overcoming most of the systematic errors discussed earlier. Although the algorithm proposed by Carré [49] is insensitive to first order calibration error and enables the use of arbitrary phase steps, the study imposes a restriction on the choice of the phase step value in order to minimize certain other error sources referred to in [89]. The algorithm proposed by Lai and Yatagai [90] requires first, an additional optical setup for the generation of Fizeau fringes and second, is only able to handle fringes that are not straight and equally spaced [91]. Farrell and Player [92, 93] describe an ellipse fitting technique that uses Bookstein algorithm [94] - a forced fit method - to fit the data set into an ellipse. The data set fits into a hyperbole for noisy data [95]. The statistical approach proposed by Cai *et al.* [96] to extract reference phase steps imposes requirements on the spatial resolution of the CCD camera (which in turn dictates the sampling number of the speckle intensity). The max-min algorithm proposed by Chen *et al.* is computationally exhaustive and requires a large number of data frames (15 or more) for reliable operation [97]. The algorithm based on iterative least squares estimation proposed by Han and Kim is suitable only for compensating linear first order errors in PZT and requires the initial guess of the phase step to be as close as possible to its true value [98]. The concept of identifying the reference phase steps proposed by Jüptner *et al.* is suitable only for linear miscalibration error and can produce a large number of outliers for noisy interferograms [99]. Although the five frame algorithm proposed by Stoilov and Dragostinov gives the flexibility of using arbitrary phase steps, its use is limited only to compensate linear errors encountered in the PZT [50].

The next significant step in phase measurement would be to extend its capabilities to optical configurations, providing multiple channel capabilities. Incorporation of multiple PZTs appears to be a feasible solution to achieve this objective. The research in this direction is still in its nascent stage and the scope of phase shifting interferometry can be expected to be enhanced manifolds if this area of research was to be actively pursued. In effect, Rastogi [100, 101] has shown that when two PZTs are placed symmetrically across an object in a holographic moiré [102] configuration, two orthogonal displacement components can be determined simultaneously.

1.3 Multiple Phase Shifting Interferometry

The use of a single PZT in an optical setup has become a common practice, and which allows classical interferometers to quantify the information encoded in the phase. However, the amount of information that can be measured is limited in this case, as information corresponding to only one component of displacement can be measured at a time. Rastogi [100, 101] was the first to introduce the incorporation of dual PZTs in an optical interferometer. He showed that in holographic moiré when two PZTs are placed symmetrically across an object in an optical configuration, two orthogonal displacement components can be measured simultaneously.

The next subsections discuss in brief the concept of holographic interferometry and holographic moiré and present limitations associated with these methods.

1.3.1 Holographic Interferometry

Holographic interferometry basically involves comparison of two or more wave fields interferometrically, in which at least one of them must be holographically recorded and reconstructed. This technique offers the possibility to measure displacements, deformations, vibrations, and shapes of rough objects but does not allow comparison of their mechanical behaviors or shapes in a direct interferometric way. The technique however, fails to address an area of significant interest to engineers: the direct interferometric comparison of granular wave fields scattered from two rough surfaces. In absence of any real time procedure to obtain direct interferometric comparison of two different objects, the technique of comparative holographic moiré has tended to fill the gap by providing indirect visualization of difference fringes with interferometric precision. Comparative holographic moiré has a strong potential in non-destructive testing, such as the comparison of the mechanical behavior of produced components against a flaw-free master component. The following section discusses the development in the field of comparative holographic moiré .

1.3.2 Comparative Holographic Interferometry

Holographic interferometric techniques have been applied over the years for comparison of smooth surfaces such as lens and mirrors. However, the comparison of two rough objects is a complicated task because of the difference in the microstructures of the objects to be compared. In 1980, Neümann [103], proposed a procedure to compare the deviations of two objects with different microstructures. He termed the technique as Comparative Holography. The technique involves the coherent illumination of every state of the sample with the conjugated wave front of the corresponding state of the master. The adaptive illumination of the sample is performed by the coherent mask of the master. In 1983, Gyimesi and Füzessy [104] implemented the Holographic technique proposed by Neümann. This technique makes the direct holographic comparison possible with an added advantage of also extending the practical range of holographic interferometry. In this technique, the test object (the object to be examined) is illuminated with the holographically recorded and reconstructed real images of the master object (the object serving as the base of comparison). The test object is illuminated in its initial state with the initial image of the master object and in its final state with the final image of the master object. However, the technique in spite of having interferometric sensitivity has not been used widely because of its tedious experimental procedure and poor fringe quality.

The concept of Comparative Holographic Moiré, was introduced by Rastogi [105, 106]. This method is based on the incoherent superposition of the interferograms and the evaluation of the resulting moiré pattern. The moiré fringes so produced are indicative of the difference between the two objects. The technique also requires introduction of complementary steps such as the introduction of auxiliary carrier fringes to improve the fringe visibility by moving the plate or the reference or the objects, followed by optical filtering in order to eliminate the carrier. By its ability to display the differences of surface deformations of two nominally identical components in response to the same loads, the comparative holographic technique has a strong potential to find use in applications in non-destructive testing of produced components by comparing their strength against a flaw-free master component.

1.4 Practical Aspects in Multiple Phase Shifting

Unfortunately, the phase shifting algorithms have not kept pace with the complex needs in comparative holographic moiré. To date, no phase shifting technique has been implemented that accommodates the requirements inherent in holographic moiré . In the present form of measurement, only the value of one component corresponding to the difference in displacement carried on moiré is quantified, whereas the information carried on the carrier is lost. However, in several interferometers, incorporation of this information would add value to the systems as in many applications the capacity for registering simultaneously information carried on moiré and on carrier is essential. A technique capable of achieving this objective represents a substantial advancement in phase shifting as it would circumvent limitations exhibited by the present crop of phase shifting techniques of measuring only one displacement component at any given instant of time. Moreover, the dual phase-shifting algorithms for holographic moiré [100,101] produces a corrupted wrapped phase of moiré corrupted with carrier. Hence, there is a need to extract *sans* interference, the information conveyed by the carrier and the moiré , so that the two orthogonal displacement components corresponding to the out-of-plane and in-plane displacement components can be obtained.

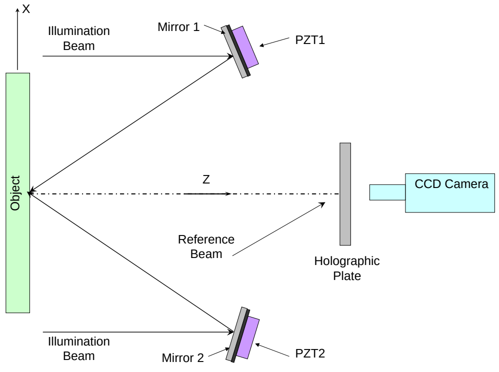

Fig. 1.1: Schematic of holographic moiré.

Figure (1.1) shows the configuration for the holographic moiré setup. The intensity equation for moiré is given by [100,101]

$$I(P) = I_{dc}\{1 + V[\cos\varphi_1(P) + \cos\varphi_2(P)]\} \tag{1.1}$$

where, I_{dc} is the mean intensity, V is the visibility, and $\varphi_1(P)$ and $\varphi_2(P)$ are the interference phases at a point P on the object surface along the two arms of the interferometer. The sum of phases can be extracted by introducing appropriate phase shifts in the two arms of the interferometer and recording the corresponding intensities. Equation (1.1) thus becomes

$$I(P) = I_{dc}\{1 + V[\cos(\varphi_1(P) + \alpha) + \cos(\varphi_2(P) + \beta)]\} \tag{1.2}$$

where, α and β are the phase steps introduced in the two arms of the interferometer. In order to recover the sum of phase term $\Phi_+ = \varphi_1(P) + \varphi_2(P)$, we apply pairs of phase steps $(-2\alpha, -2\beta)$, $(-\alpha, -\beta)$, $(0, 0)$, (α, β), and $(2\alpha, 2\beta)$ to the PZTs. Frames I_1, I_2, I_3, I_4, and I_5 corresponding to these phase steps are recorded in the computer [100,101]. Assuming, $\alpha = \beta = \pi/2$, the term corresponding to the sum of phases is given by

$$\Phi_+ = 2\tan^{-1}\left[\frac{2(I_2 - I_4)}{2I_3 - I_1 - I_5}\right] \tag{1.3}$$

Similarly, in order to recover the difference of phase term, $\Phi_- = \varphi_1(P) - \varphi_2(P)$, we apply pairs of phase steps $(-2\alpha, 2\beta)$, $(-\alpha, \beta)$, $(0, 0)$, $(\alpha, -\beta)$, and $(2\alpha, -2\beta)$ to the PZTs. Frames I_1, I_2, I_3, I_4, and I_5 corresponding to these phase steps are recorded in the computer. Assuming, $\alpha = \beta = \pi/2$, the term corresponding to the difference of phases is given by

$$\Phi_- = 2\tan^{-1}\left[\frac{2(I_2 - I_4)}{2I_3 - I_1 - I_5}\right] \tag{1.4}$$

However, the wrapped sum and difference of phases obtained from Eqs. (1.3) and (1.4), respectively, are corrupted even in the absence of any noise. The problems associated with these dual phase shifting algorithms will be evident by simulating the moiré fringe pattern. For this, let the phase terms recorded at a pixel (n', j') on the CCD for Eq. (1.2) be written as

$$\varphi_1(n', j') = \frac{2\pi\sqrt{(n' - n_0)^2 + (j' - j_0)^2}}{\lambda_1} + \Phi_{ran1} \tag{1.5a}$$

$$\varphi_2(n', j') = \frac{2\pi\sqrt{(n' - n_0)^2 + (j' - p_0)^2}}{\lambda_2} + \Phi_{ran2} \tag{1.5b}$$

where, (n_0, j_0) is the origin for the intensity image of $n' \times j'$ pixels corresponding to phase in Eq. (1.5a), and (n_0, p_0) is the origin for the intensity image of $n' \times j'$ pixels corresponding to phase in Eq. (1.5b). Here, Φ_{ran1} and Φ_{ran2} represent the random phase terms 0 to 2π because of the rough nature of the object surface. Assuming the visibility V to be unity, Figs. (1.2a) and (1.2b) show the fringe pattern (512 × 512 pixels) corresponding to Eq. (1.2), under the assumption $\Phi_{ran1} = \Phi_{ran2} = 0$ and $\Phi_{ran1} = \Phi_{ran2} \neq 0$, respectively. The wrapped phase maps corresponding to Φ_+ using Eq. (1.3) –for Figs. (1.2a) and (1.2b) –are shown in Figs. (1.3a) and (1.3b), respectively. The figures show that the information carried by the sum of phases is corrupted by the moiré fringes. Similarly, the wrapped difference of phases corresponding to Φ_- using Eq. (1.4) –for Figs. (1.2a) and (1.2b) –are shown in Figs. (1.4a) and (1.4b), respectively. The figures show that the information carried by the difference of phases is corrupted by the carrier fringes. The same phenomenon is also observed for the three-frame [101] and seven-frame [100] algorithms.

The point which needs to be emphasized here is that the straightforward adaptation of these conventional algorithms to dual phase stepping is not possible. This limitation motivates us to explore if generalized algorithms can be designed for multiple phase shifting interferometry. As mentioned earlier, the generalized data reduction technique for simple phase shifting [78,79]

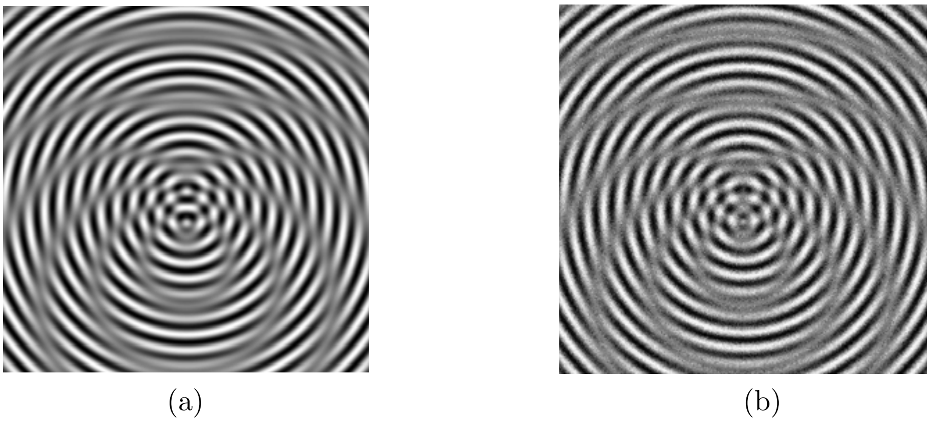
(a) (b)

Fig. 1.2: Moiré fringes (512 × 512 pixels) corresponding to Eq. (1.2). In (a) the random phases $\Phi_{ran1} = \Phi_{ran2} = 0$, while in (b) φ_1 and φ_2 are assumed to be random.

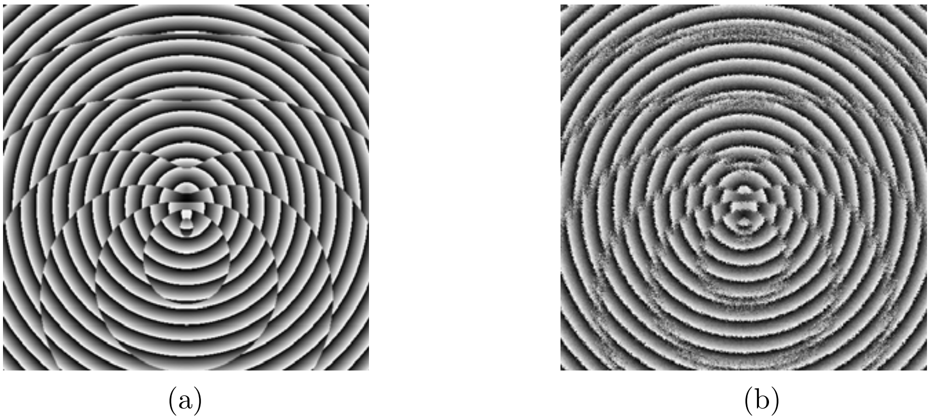
(a) (b)

Fig. 1.3: The map corresponding to the wrapped sum of phases $\varphi_1 + \varphi_2$ obtained using Eq. (1.3) for the fringe map in (a) Fig. (1.2a) and (b) Fig. (1.2b).

offers flexibility in selecting the phase steps, which can be arbitrary, but the procedure for determining the exact value of the phase step in least squares fit is critical. The iterative algorithms suggested are designed only for simple phase shifting [98, 107]. As far as we know, no generalized phase shifting technique has been developed in holographic moiré which enables the accurate determination of the dual phase steps provided by the PZTs during the recording of a same frame. The spatial technique developed by Lai and Yatagai [90] for determining the phase shift of the reference beam while acquiring the data frames is only applicable to single phase stepping configuration.

One approach which seems to be tempting is to minimize the objective function in Eq. (1.2) so that the phase steps α and β can be estimated. Once these phase steps are estimated any linear regression technique can be applied to estimate the phases φ_1 and φ_2. However, it is important to study the topology of the objective function to be minimized so that difficulties in identifying the phase steps can be gauged. For Eq. (1.2), the objective function can be written as

$$\mathbf{E} = \sum_{n=0}^{N-1} (I(P) - I_{dc}\{1 + V[\cos(\varphi_1(P) + \alpha) + \cos(\varphi_2(P) + \beta)]\})^2 \tag{1.6}$$

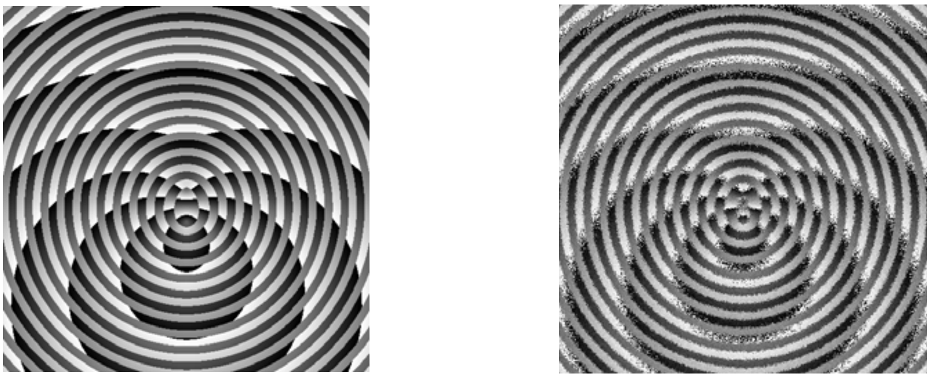

(a) (b)

Fig. 1.4: The map corresponding to the wrapped difference of phases $\varphi_1 - \varphi_2$ obtained using Eq. (1.4) for the fringe map in (a) Fig. (1.2a) and (b) Fig. (1.2b).

Figure (1.5) shows a plot for objective function in Eq. (1.6) at any arbitrary pixel location (n', j') for $N = 10$ data frames with x-axis representing the phase step α and y-axis representing the phase φ_2. For plotting the curve we have assumed $\varphi_1 = 2.0943$ radians; $\varphi_2 = 1.04719$ radians; $\beta = 0.78539$ radians; $V = 1$; and $I_{dc} = 1$. The intensity $I(P)$ at the same pixel location for ten data frames is then determined with step increments $\alpha = 1.57079$ radians or 90° between each data frame assuming linear response of the phase shifter. Note that for phase step α between 0 and 2π, we find two global minima's and many local minima. The topology of the objective function looks very complicated and in such cases any local search technique does not seem to be a feasible solution. Even, the global search techniques such as Genetic algorithm (GA), Simulated Annealing (SA), or Probabilistic Global Search Lausanne (PGSL), etc. to name a few, may not be an attractive solution, and moreover, these algorithms although successful will increase the computational overhead. These algorithms are also very sensitive to noise which is bound to influence the measurement and in such circumstances, there is a need to propose a method which is a robust performer in the estimation of phase even in the presence of noise.

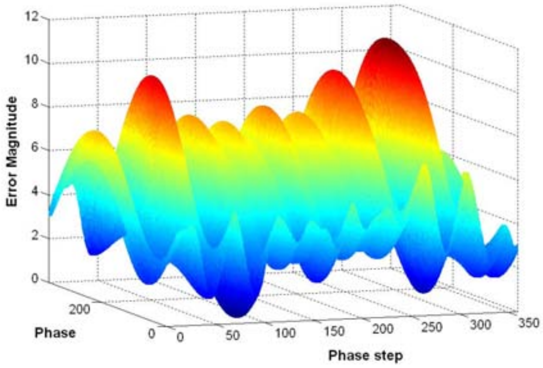

Fig. 1.5: Plot shows the magnitude of error for objective function defined in Eq. (1.6) when the phase φ_2 and phase step α, are varied from 0 to 2π. The plot shows the presence of two global minima.

In this context, the objective of the thesis is to present novel phase shifting algorithms which would enable quantitative estimation of data extracted from interference fringes. These algorithms not only allow the use of multiple PZTs in the optical setup but also exhibit the possibility to minimize systematic and random error sources. Throughout the thesis the algorithms will be explained with reference to holographic interferometry or holographic moiré , however, these algorithms can also be applied to other techniques for phase extraction.

1.5 Research Objective

To the best of the author's knowledge no generalized phase shifting technique has been reported so far which at a time

- caters to the presence of multiple PZTs in an optical configuration
- is insensitive to errors due to nonsinusoidal waveforms
- immune to PZT miscalibration
- minimizes additive white Gaussian intensity noise
- has the ability to work with diverging as well as converging beam
- allows the use of arbitrary phase steps.

With the field of phase shifting interferometry advancing rapidly, the possibility of incorporating multiple PZTs in an interferometric configuration is a significant conceptual progress which should be useful for developing multiple channel measurement capabilities in moiré based interferometers.

1.6 Thesis Focus

The first aim of this thesis is to present methods which

- cater to the presence of multiple PZTs in an optical configuration,
- are capable of handling harmonics,
- are insensitive to errors arising from PZT miscalibration,
- are applicable to spherical beams, and
- are robust performer even in the presence of white Gaussian intensity noise.

The second aim of this thesis is

- to compare the developed methods so that an efficient approach for estimating the phase information is determined.

The third aim of this thesis is

- to show the experimental feasibility of the proposed methods in a holographic moiré setup involving two PZTs

1.7 Outline of Thesis

The estimation of multiple phase information is realized by the introduction of high resolution methods in phase shifting interferometry. We first derive the phase information by directly working with the design of a Hankel matrix from the intensity data recorded temporally at (n', j') pixel of the data frames. Chapter 2 presents the concept of annihilation filter in the estimation of phase information.

Chapter 3 introduces a state-space approach where the concept of annihilation filter still remains the basis for the estimation of phase. However, in this case, the phase is extracted from the covariance matrix rather than the signal directly. We also introduce a new denoising procedure for the estimation of phase at lower signal-to-noise ratio (SNR).

Chapter 4 focuses on the estimation of phase from the design of a sample covariance matrix and on performing the eigenvalue decomposition to yield the noise and the signal subspaces. The phase steps are estimated from the noise subspace using the method commonly known as MUltiple-SIgnal Classification method (MUSIC).

Chapter 5 presents a minimum-norm method based on MUSIC but which is computationally less exhaustive. The chances of spurious phase step estimates are greatly reduced using this method.

Chapter 6 presents the estimation of phase from the signal subspace using an elegant method known as Estimation of Signal Parameter using Rotational Invariance (ESPRIT).

Chapter 7 introduces an optimally efficient Maximum-likelihood method based on the spectral estimation theory.

Chapter 8 discusses the various constraint associated with the estimation of dual phase estimation in holographic moiré .

Chapter 9 presents a statistical study and experimental verification of these methods in the estimation of phase information in the case of a single as well as dual PZTs.

Chapter 10 summarizes the salient features of the research work.

Chapter 2

Phase Estimation by Design of an Annihilation Filter

In this chapter we first, present a novel approach [1, 108] based on the design of an *annihilation filter* for estimating the phase step imparted to the PZT, and second, propose the design of a Vandermonde system of equations for estimating the phase distribution. This approach is next extended for determining multiple phases in holographic moiré . We also describe a denoising procedure which is to be incorporated before the estimation of phase step values.

2.1 Introduction

The intensity for the N data frames acquired on the CCD camera at a pixel (n', j') for n^{th} phase step in an optical configuration involving single PZT can be written as

$$I(n', j'; n) = I_{dc} + \sum_{k=-1}^{-\kappa} a_k \exp[jk(\varphi + n\alpha)] + \sum_{k=1}^{\kappa} a_k \exp[jk(\varphi + n\alpha)]; \qquad \text{for } n = \ 0, 1, 2, ..., N-1. \tag{2.1}$$

where, a_k is the complex Fourier coefficient of the κ^{th} order harmonic, $j = \sqrt{-1}$ and I_{dc} is the local average value for intensity; and pairs φ and α, represent phase difference and phase shift, respectively, in the interferometer. The coefficient a_k is in fact real and are related to the appropriate choice of phase origin at a point where the intensity reaches a maximum. In order to understand the basics of the annihilation filter method let us rewrite Eq. (2.1) in the following form

$$I_n(n', j') = I_{dc} + \sum_{k=1}^{\kappa} \ell_k u_k^n + \sum_{k=1}^{\kappa} \ell_k^* (u_k^*)^n; \qquad \text{for } n = \ 0, 1, 2, ..., N-1. \tag{2.2}$$

where, $\ell_k = a_k \exp(jk\varphi)$, $u_k = \exp(jk\alpha)$ and superscript $*$ denotes the complex conjugate. Note that throughout the text, the subscript n (denoted as I_n) and index n (denoted as $I(n)$) will be used interchangeably. Equation (2.2) represents the complex valued sinusoidal signals where,

I_{dc}, $\alpha, ...,\kappa\alpha; -\alpha, ...,-\kappa\alpha$ represent the frequencies embedded in the signal, and by estimating them, the phase step α imparted to the PZT can be determined. Frequency estimation of sinusoids is a classical problem in spectral estimation and can be better handled using a annihilation filter method. In this method [1] we first transform the discrete time domain signal in Eq. (2.2) into a complex frequency domain by taking its Z-transform. Let the Z-transform of I_n be denoted by $\mathbf{I}(z)$. The objective here is to design another polynomial $\mathbf{P}(z)$ termed as annihilating filter which has zeros at frequencies associated with $\mathbf{I}(z)$, which in turn would result in $\mathbf{I}(z)\mathbf{P}(z) = 0$. Since the frequencies translate into zeros, spectral estimates feature high resolution. In what follows we will derive the expression for $\mathbf{P}(z)$ and explore the condition for which the multiplication of $\mathbf{P}(z)$ and $\mathbf{I}(z)$ is zero. The Z-transform of Eq. (2.2) is written as

$$\mathbf{I}(z) = \sum_{n=0}^{N-1} I_n z^{-n} = \sum_{n=0}^{N-1} I_{dc} z^{-n} + \sum_{n=0}^{N-1}\sum_{k=0}^{\kappa} \ell_k u_k^n z^{-n} + \sum_{n=0}^{N-1}\sum_{k=0}^{\kappa} \ell_k^* (u_k^*)^n z^{-n} \tag{2.3}$$

which after expansion and simplification can be written as

$$\begin{aligned}\mathbf{I}(z) =& I_{dc}\left(\frac{1-z^{-N}}{1-z^{-1}}\right) + \sum_{k=1}^{\kappa} \ell_k[1-\exp(jk\alpha N)z^{-N}]\left[\frac{D_1(z)}{P_1(z)}\right] + \\ & \sum_{k=1}^{\kappa} \ell_k^*[1-\exp(-jk\alpha N)z^{-N}]\left[\frac{D_2(z)}{P_2(z)}\right]\end{aligned} \tag{2.4}$$

where, $D_1(z) = \prod_{r=1,r\neq k}^{\kappa}[1-\exp(jr\alpha N)z^{-1}] = \sum_{r=0}^{\kappa-1} d_{1r}z^{-r}$; $D_2(z) = \prod_{r=1,r\neq k}^{\kappa}[1-\exp(-jr\alpha N)z^{-1}] = \sum_{r=0}^{\kappa-1} d_{2r}z^{-r}$; $P_1(z) = \prod_{k=1}^{\kappa}[1-\exp(jk\alpha N)z^{-1}]$; and $P_2(z) = \prod_{k=1}^{\kappa}[1-\exp(-jk\alpha N)z^{-1}]$. Taking into account the terms $D's$ and $P's$ and substituting them in Eq. (2.4), we obtain

$$\begin{aligned}\mathbf{I}(z) =& I_{dc}\left(\frac{1-z^{-N}}{1-z^{-1}}\right) + \\ & \left\{\frac{\sum_{k=1}^{\kappa}\ell_k\left[\sum_{r=0}^{\kappa-1} d_{1r}z^{-r} - \sum_{r=0}^{\kappa-1} d_{1r}\exp(jk\alpha N)z^{-(r+N)}\right]}{\prod_{k=1}^{\kappa}[1-\exp(jk\alpha)z^{-1}]}\right\} + \\ & \left\{\frac{\sum_{k=1}^{\kappa}\ell_k^*\left[\sum_{r=0}^{\kappa-1} d_{2r}z^{-r} - \sum_{r=0}^{\kappa-1} d_{2r}\exp(-jk\alpha N)z^{-(r+N)}\right]}{\prod_{k=1}^{\kappa}[1-\exp(-jk\alpha)z^{-1}]}\right\}\end{aligned} \tag{2.5}$$

Equation (2.5) can be represented as

$$\mathbf{I}(z)\mathbf{P}(z) = \mathbf{D}(z) \tag{2.6}$$

where, $\mathbf{D}(z)$ represents the numerator and $\mathbf{P}(z)$ the denominator in the right hand side of Eq. (2.5), with the latter being given by

$$\begin{aligned}\mathbf{P}(z) =&(1-z^{-1})\prod_{k=1}^{\kappa}[1-\exp(jk\alpha)z^{-1}][1-\exp(-jk\alpha)z^{-1}]\\ =&\sum_{k=0}^{2\kappa+1} p_k z^{-k}\end{aligned} \tag{2.7}$$

Given the complex form of $\mathbf{D}(z)$, let us consider for the sake of simplicity writing only its first term,

$$\begin{aligned}\mathbf{C_1}(z) =&\sum_{k=1}^{\kappa} I_{dc}(1-z^{-N})\mathbf{P_1}(z)\mathbf{P_2}(z)\\ =&\sum_{r=0}^{2\kappa}\mathbf{C1}_r z^{-r}-\sum_{r=0}^{2\kappa}\mathbf{C1}_{r+N}z^{-(r+N)}\end{aligned} \tag{2.8}$$

From Eq. (2.8) we observe that some coefficients of $\mathbf{C_1}(z)$, specifically, $\mathbf{C1}_0$, $\mathbf{C1}_1$, $\mathbf{C1}_2$,...,$\mathbf{C1}_{2\kappa}$, and $\mathbf{C1}_N$, $\mathbf{C1}_{N+1}$, $\mathbf{C1}_{N+2}$,..., $\mathbf{C1}_{N+2\kappa}$, depend upon the unknown amplitude and frequency. We observe that the coefficients $\mathbf{C1}_{2\kappa+1}$, $\mathbf{C1}_{2\kappa+2}$, $\mathbf{C1}_{2\kappa+3}$,...,$\mathbf{C1}_{N-1}$, are identically zero for $N \geq 2\kappa+1$. This condition is at the essence of the design of annihilating filter $\mathbf{P}(z)$. In what follows we show that the $(2\kappa+1)^{th}$ degree polynomial $\mathbf{P}(z)$, when discretely convolved with $\mathbf{I}(z)$ yields zero. Since the multiplication of two signals in frequency domain corresponds to its discrete convolution in time domain, inverse Z-transform of Eq. (2.6) gives

$$I_n \otimes p_n = D_n \tag{2.9}$$

where, $\otimes$ represents the convolution operator. In Eq. (2.9), p_n is the inverse Z-transform of $\mathbf{P}(z)$ defined by

$$p_n = p_0\delta(n)+p_1\delta(n-1)+p_2\delta(n-2)+.....+p_{2\kappa+1}\delta(n-2\kappa-1) \tag{2.10}$$

where, $\delta(n)$ is the unit impulse signal. Equation (2.10) can be further written as

$$\sum_{k=0}^{2\kappa+1} I_{n-k}p_k = D_n;\ \text{ for } n=0,1,2,....,N,.....,N+2\kappa. \tag{2.11}$$

Using the fact,

$$\begin{aligned}I_n =&\begin{cases}0, & \text{for } n<0\\ I_n, & 0\leq n\leq N-1\\ 0, & n\geq N\end{cases}\\ \delta(n) =&\begin{cases}1, & \text{for } n=0\\ 0, & \text{else where}\end{cases}\end{aligned} \tag{2.12}$$

we can express Eq. (2.11) in a matrix form as

$$\left[\begin{array}{ccccc} I_0 & 0 & 0 & \dots & 0 \\ I_1 & I_0 & 0 & \dots & 0 \\ \cdot & \cdot & \cdot & \cdot & \cdot \\ \cdot & \cdot & \cdot & \cdot & \cdot \\ \hline I_{2\kappa+1} & I_{2\kappa} & 0 & \dots & I_0 \\ I_{2\kappa+2} & I_{2\kappa+1} & 0 & \dots & I_1 \\ \cdot & \cdot & \cdot & \cdot & \cdot \\ I_{N-2} & I_{N-3} & 0 & \dots & I_{N-2\kappa-3} \\ I_{N-1} & I_{N-2} & 0 & \dots & I_{N-2\kappa-2} \\ \hline 0 & I_{N-1} & I_{N-2} & \dots & \cdot \\ 0 & 0 & \cdot & \dots & \cdot \\ \cdot & \cdot & \cdot & \cdot & \cdot \\ 0 & \cdot & \cdot & \cdot & I_{N-2} \\ 0 & 0 & 0 & \dots & I_{N-1} \end{array}\right] \times \left[\begin{array}{c} p_0 \\ p_1 \\ p_2 \\ \cdot \\ p_{2\kappa+1} \end{array}\right] = \left[\begin{array}{c} D_0 \\ D_1 \\ \cdot \\ D_{2\kappa} \\ \hline 0 \\ 0 \\ \cdot \\ 0 \\ \hline D_N \\ \cdot \\ D_{N+2\kappa} \end{array}\right] \tag{2.13}$$

We partition the first matrix on the left hand side of Eq. (2.13), select the middle $N-2\kappa-2$ rows equations corresponding to zero row values in the matrix on the right hand side, and form a new matrix as follows:

$$\underbrace{\begin{bmatrix} I_{2\kappa+1} & I_{2\kappa} & 0 & \dots & I_0 \\ I_{2\kappa+2} & I_{2\kappa+1} & 0 & \dots & I_1 \\ \vdots & \vdots & \vdots & \vdots & \vdots \\ I_{N-2} & I_{N-3} & 0 & \dots & I_{N-2\kappa-3} \\ I_{N-1} & I_{N-2} & 0 & \dots & I_{N-2\kappa-2} \end{bmatrix}}_{\mathbf{R}} \times \underbrace{\begin{bmatrix} p_0 \\ p_1 \\ p_2 \\ \vdots \\ p_{2\kappa+1} \end{bmatrix}}_{\mathbf{P}} = \begin{bmatrix} 0 \\ 0 \\ \vdots \\ \vdots \\ 0 \end{bmatrix} \tag{2.14}$$

We can infer from Eq. (2.14) that the polynomial $\mathbf{P}(z)$ is an annihilating filter which when convolved with the intensity signal yields zero. It can further be deduced that at least $N \geq 2\kappa+2$ samples are required to extract the roots of the polynomial $\mathbf{P}(z)$. This enables us to find the unknown value u_k. The phase step α can hence be computed using $\alpha = \Re(\ln u_1/j)$. One of the important aspect in phase shifting interferometry is to first identify the number of harmonics present in the wavefront so that appropriate annihilation filter can be designed. Next section discusses in detail the method to identify the number of harmonics.

2.2 Detection of Nonsinusoidal Waveform

The occurrence of nonsinusoidal waveform - a consequence of detector nonlinearity or multiple reflections in laser cavity - results in an error in the computation of phase. This section explains how to deduce the number of harmonics κ present in the signal, which can subsequently be applied in the design of the Vandermonde system of equations in Section 2.4 for the determination of phase value φ. Let us rewrite Eq. (2.1), for the case $\kappa = 1$ (i.e. pure sinusoidal wave) and noiseless signal, as

$$\begin{aligned} I(n', j'; n) = I_{dc} + a_{-1}\exp[-jk(\varphi + n\alpha)] + a_1 \exp[jk(\varphi + n\alpha)]; \\ \text{for } n = \ 0, 1, 2, ..., N-1. \end{aligned} \tag{2.15}$$

Fourier transform of $I(n', j'; n)$ for $n = 0, 1, 2, 3, ..., N-1$ should result in three peaks in frequency domain corresponding to I_{dc}, α, and $-\alpha$. However, with limited data samples, the resolution of closely spaced frequencies is troublesome in the presence of noise. Also because of the "leakage" phenomenon, energy in the main lobe can leak into the side lobes obscuring and distorting other spectral responses.

Interestingly, the singular value decomposition (SVD) of $\mathbf{R}$ in Eq. (2.14), represented as $\mathbf{R} = \mathbf{USV}^T$, yields more reliable information than the Fourier transform method regarding the number of harmonics present in the signal, where $\mathbf{S}$ is a diagonal matrix with M nonzero and $N-M$ zero singular values; $\mathbf{U}$ and $\mathbf{V}$ are unitary matrices [109]. In Eq. (2.14), for a noiseless case, the number of nonzero diagonal entries in S is $M = 3$ (corresponding to I_{dc}, α, and $-\alpha$). In the presence of noise, M principal values of $\mathbf{S}$ would still tend to be larger than the $N - M$ values which were originally zero. In addition, the M eigenvectors corresponding to the M eigen values of $\mathbf{R}^T\mathbf{R}$ are less susceptible to noise perturbations in comparison to the remaining eigenvectors.

Figure (2.1) illustrates typical singular values for $\mathbf{S}$ obtained from the SVD of $\mathbf{R}$ for noise at a signal-to-noise ratio (SNR) of 10 dB and without noise, and when $\kappa = 2$. Although eighteen frequencies were assumed to be present during the estimation, only five principal values of $\mathbf{S}$ for noisy and noiseless signals show a distinctly larger magnitude than the remaining values. The plot thus permits a reliable estimation of the number of harmonics.

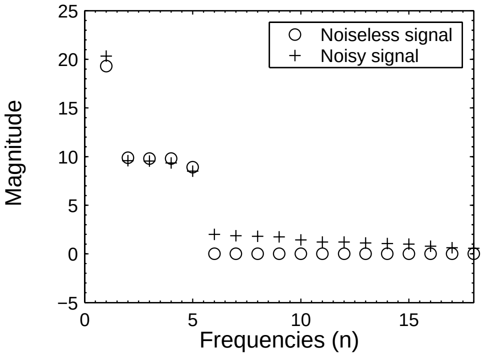

Fig. 2.1: Plot showing the magnitude of diagonal values in matrix $\mathbf{S}$ versus N data points. From the plot the number of harmonics κ in the signal can be computed using $M = 2\kappa + 1$. In figure (o) and (+) represent the diagonal values for noiseless and noisy (SNR=10 dB) signals, respectively.

2.3 Denoising the Signal

There are various sources of noise in optical interferometry and the relative contribution of each noise source depends on the particular system and its application [110]. Denoising is thus an important step towards reducing the effect of noise. We consider white Gaussian noise to contaminate the signal; the reason being that many distributions can be approximated by a Gaussian function. It should also be noted that many noise sources are known to follow a Gaussian noise source in accordance to the central limit theorem [74]. To enhance the signal in the presence of white Gaussian noise, we apply the concept of truncated singular value decomposition. In the present case, number of data frames $N \geq 4\kappa + 2$ are needed for applying the denoising procedure. The concept of TSVD involves the following steps [111, 112]. The matrix $\mathbf{R}$ is first written in Hankel matrix form, say $\hat{\mathbf{R}}$, and its singular value decomposition $\hat{\mathbf{R}} = \hat{\mathbf{U}}\bar{\mathbf{S}}\hat{\mathbf{V}}^T$ shows the nonsingular principal values of $\bar{\mathbf{S}}$ which are significantly different from zero. After setting the non significant $N - M$ singular values of $\bar{\mathbf{S}}$ to zero, a matrix $\hat{\mathbf{S}}$ is formed. A denoised matrix $\mathbf{Z}_M = \hat{\mathbf{U}}\hat{\mathbf{S}}\hat{\mathbf{V}}^T$ which approximates $\bar{\mathbf{R}}$ in the least squares sense is then obtained by using the first M columns of $\hat{\mathbf{U}}$, $\hat{\mathbf{S}}$ and $\hat{\mathbf{V}}$; $\hat{\mathbf{U}}$ and $\hat{\mathbf{V}}$ being unitary matrices. Finally, a denoised signal $\bar{I}_n$ is retrieved by arithmetic averaging along the anti-diagonals (or diagonals) of $\mathbf{Z}_M$ using

$$\bar{I}_n = \frac{1}{r - q + 1} \sum_{s=0}^{N-1} \mathbf{Z}_M(n - s + 1, s + 1); \text{ for } n = \ 0, 1, 2, ..., N - 1. \tag{2.16}$$

where, $r = max[1, n-\text{number of rows}(\hat{\mathbf{R}})+1]$ and $q = min[\text{number of rows}(\hat{\mathbf{R}}), n]$. The denoised signal $\hat{I}_n$ is subsequently applied in Eq. (2.14).

2.4 Evaluation of Phase Step and Phase Distribution in Presence of Noise

The next step after denoising the signal is to extract the phase step. The concept of design of annihilation filter for intensity is tested by simulating fringe pattern in Eq. (2.1); we assume $\kappa = 2$, $\alpha = pi/4$, $a_{\pm 1, \pm 2} = 0.5$, and $I_{dc} = 1$. Additive white Gaussian noise with SNR between 0 and 100 dB is added to Eq. (2.1) and for each noise level phase step is computed at every pixel of the data frame without and with the application of the denoising procedure described in the previous section. Figures (2.2a) and (2.2b), respectively, show plots for phase step α at any arbitrary pixel location, without and with denoising procedure for fifteen data frames. Figure (2.2b) shows that denoising is an important step in extracting information from a noisy data. The accuracy in the determination of the number of harmonics κ and the phase step α in the presence of increasing noise can be improved with an increase in the redundancy of the data frames. Once the phase step α is estimated using the annihilation filter method, the parameter ℓ_k can be solved using the linear Vandermonde system of equations obtained from Eq. (2.2). Recall that $\ell_k = a_k \exp(jk\varphi)$ in Eq. (2.2). A Vandermonde matrix usually arises in

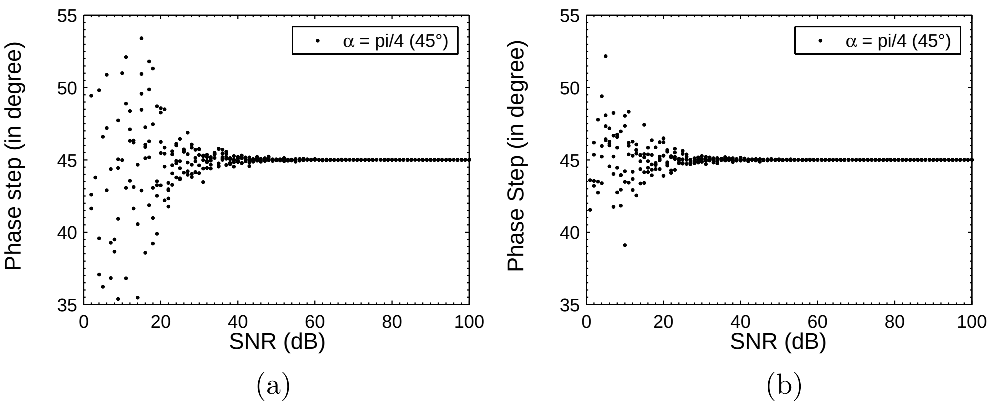

(a)

(b)

Fig. 2.2: The plot of phase step α (in degree) at arbitrary pixel locations versus SNR (in dB) a) without and b) with application of the denoising procedure.

the polynomial least squares fitting, Lagrange interpolating polynomials, or in the statistical distribution of the distribution moments [113, 114]. A Vandermonde matrix of order l can be written as

$$\begin{bmatrix} 1 & 1 & 1 & \dots & 1 \\ x_1 & x_2 & x_3 & \dots & x_l \\ x_1^2 & x_2^2 & x_3^2 & \dots & x_l^2 \\ \vdots & \vdots & \vdots & \vdots & \vdots \\ x_1^{l-1} & x_2^{l-1} & x_3^{l-1} & \dots & x_l^{l-1} \end{bmatrix} \tag{2.17}$$

In some references, the transpose of the matrix in Eq. (2.17) is also known as Vandermonde matrix. The solution of $l \times l$ Vandermonde matrix requires l^2 operations. The advantage of Vandermonde matrix is that its determinant is always nonzero (hence invertible) for different values of $x = (x_1, x_2, x_3, ..., x_l)$. In our case the matrix for the phase step α can be written in the following convenient form

$$\begin{bmatrix} \exp(j\kappa\alpha_0) & \exp(-j\kappa\alpha_0) & \exp[j(\kappa-1)\alpha_0] & \dots & 1 \\ \exp(j\kappa\alpha_1) & \exp(-j\kappa\alpha_1) & \exp[j(\kappa-1)\alpha_1] & \dots & 1 \\ \vdots & \vdots & \vdots & \vdots & \vdots \\ \exp[j\kappa\alpha_(N-1)] & \exp[-j\kappa\alpha_(N-1)] & \exp[j(\kappa-1)\alpha_(N-1)] & \dots & 1 \end{bmatrix} \times \begin{bmatrix} \ell_\kappa \\ \ell_\kappa^* \\ \vdots \\ I_{dc} \end{bmatrix} = \begin{bmatrix} I_0 \\ I_1 \\ \vdots \\ I_{N-1} \end{bmatrix} \tag{2.18}$$

where, α_1, α_2,..,α_N are phase steps in frames I_0, I_1, I_2,...,I_{N-1}, respectively. The phase φ is subsequently computed from the argument of ℓ_1. Figures (2.3a) and (2.3b) show typical errors in the computation of unwrapped phase maps, without and with denoising step, respectively, and assuming a SNR of 30 dB. The next step is to extend this concept to holographic moiré so that two phases can be extracted simultaneously. In what follows we discuss applying annihilation filter method to holographic moiré .

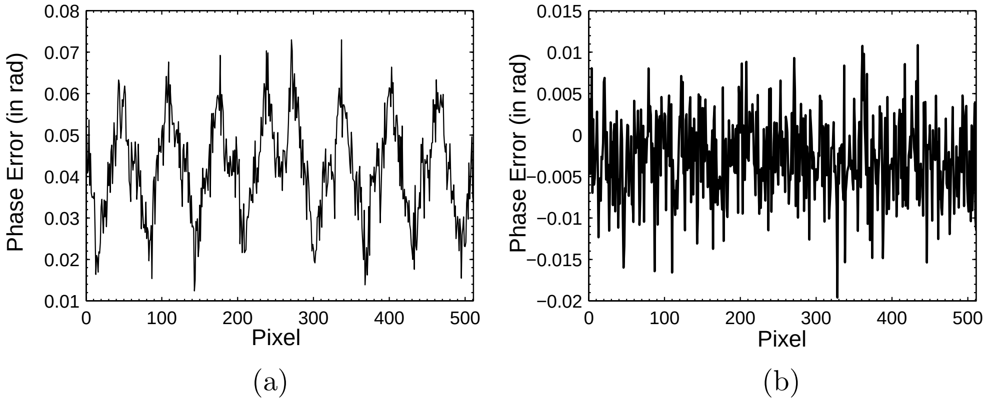

(a) (b)

Fig. 2.3: The plot of error in phase computation versus pixel (in presence of signal, having SNR=30 dB a) without and b) with application of the denoising procedure.

2.5 Design of Annihilation Filter for Holographic Moiré

Holographic moiré is essentially an incoherent superposition of two interferometric systems which result in the formation of a moiré pattern. Figure (1.1) illustrates a typical optical setup for holographic moiré [101]. In the optical setup moiré carries information regarding the in-plane displacement component along the x-direction and carrier carries the information regarding the out-of-plane displacement component. However, in conventional holographic moiré setup, the information carried by the carrier is lost. There are two drawbacks to conventional holographic moiré ; first, simple phase shifting cannot be applied to holographic moiré , not even for measuring in real-time the displacement information carried by moiré , and second, the method is unable to obtain even optically simultaneous measurement of in-plane and out-of-plane displacement distributions. Incorporation of two phase shifting devices in the holographic moiré configurations enables to overcome both the drawbacks. Two distinct phase steps are applied simultaneously to the two arms of the moiré setup. The method consists of acquiring data while voltages are simultaneously applied to the two PZTs.

The intensity for the N data frames acquired on the CCD camera at a pixel (n', j') for n^{th} phase step is given by

$$\begin{aligned} I(n',j';n) = & I_{dc} + \sum_{k=-1}^{-\kappa} a_k \exp[jk(\varphi_1 + n\alpha)] + \sum_{k=1}^{\kappa} a_k \exp[jk(\varphi_1 + n\alpha)] + \\ & \sum_{k=-1}^{-\kappa} b_k \exp[jk(\varphi_2 + n\beta)] + \sum_{k=1}^{\kappa} b_k \exp[jk(\varphi_2 + n\beta)]; \\ & \text{for } n = \ 0, 1, 2, ..., N-1. \end{aligned} \tag{2.19}$$

where, a_k and b_k are the complex Fourier coefficients of the κ^{th} order harmonic, $j = \sqrt{-1}$ and I_{dc} is the local average value for intensity; and pairs φ_1 and φ_2, and α and β, represent phase differences and phase shifts, respectively, in the two arms of the holographic moiré . The coefficients a_k and b_k are in fact real and are related to the appropriate choice of phase origin at a point where the intensity reaches a maximum. Let us rewrite Eq. (2.19) in the following form

$$\begin{aligned} I_n(n',j') = I_{dc} + \sum_{k=1}^{\kappa} \ell'_k u_k^n + \sum_{k=1}^{\kappa} {\ell'_k}^{*} (u_k^*)^n + \sum_{k=1}^{\kappa} \wp_k v_k^n + \sum_{k=1}^{\kappa} \wp_k^* (v_k^*)^n; \\ \text{for } n = \ 0, 1, 2, ..., N-1. \end{aligned} \tag{2.20}$$

where, $\ell'_k = a_k \exp(jk\varphi_1)$, $u_k = \exp(jk\alpha)$, $\wp_k = b_k \exp(jk\varphi_2)$, and $v_k = \exp(jk\alpha)$; $I_n(n', j'; m)$ corresponds to the n^{th} frame, where $n = 0$ refers to the data frame corresponding to the first phase shifted holographic moiré intensity pattern. Equation (2.20) represents the complex valued sinusoidal signals where, I_{dc}, α,...,$\kappa\alpha$;$-\alpha$,...,$-\kappa\alpha$; $-\beta$,...,$-\kappa\beta$ represent the frequencies embedded in the signal, and by estimating them, the phase steps α and β imparted to the PZT's can be determined [108]. We first transform the discrete time domain signal in Eq. (2.20) into a complex frequency domain by taking its Z-transform. The Z-transform of Eq. (2.20) is written as

$$\begin{aligned}\mathbf{I}(z) = \sum_{n=0}^{N-1} I_n z^{-n} = &\sum_{n=0}^{N-1} I_{dc} z^{-n} + \sum_{n=0}^{N-1}\sum_{k=0}^{\kappa} \ell_k' u_k^n z^{-n} + \sum_{n=0}^{N-1}\sum_{k=0}^{\kappa} {\ell_k'}^* (u_k^*)^n z^{-n} + \\ &\sum_{n=0}^{N-1}\sum_{k=0}^{\kappa} \wp_k v_k^n z^{-n} + \sum_{n=0}^{N-1}\sum_{k=0}^{\kappa} \wp_k^* (v_k^*)^n z^{-n}\end{aligned} \tag{2.21}$$

which after expansion and simplification can be written as

$$\begin{aligned}\mathbf{I}(z) =& I_{dc}\left(\frac{1-z^{-N}}{1-z^{-1}}\right) + \sum_{k=1}^{\kappa} \ell_k'[1-\exp(jk\alpha N)z^{-N}]\left[\frac{D_1(z)}{P_1(z)}\right] + \\ &\sum_{k=1}^{\kappa} {\ell_k'}^*[1-\exp(-jk\alpha N)z^{-N}]\left[\frac{D_2(z)}{P_2(z)}\right] + \\ &\sum_{k=1}^{\kappa} \wp_k[1-\exp(jk\beta N)z^{-N}]\left[\frac{D_3(z)}{P_3(z)}\right] + \\ &\sum_{k=1}^{\kappa} \wp_k^*[1-\exp(-jk\beta N)z^{-N}]\left[\frac{D_4(z)}{P_4(z)}\right]\end{aligned} \tag{2.22}$$

where, $D_1(z)$, $D_2(z)$, $P_1(z)$ and $P_2(z)$ have been defined in Eq. (2.4), and $D_3(z) = \prod_{r=1,r\neq k}^{\kappa}[1-\exp(jr\beta N)z^{-1}] = \sum_{r=0}^{\kappa-1} d_{1r}z^{-r}$; $D_4(z) = \prod_{r=1,r\neq k}^{\kappa}[1-\exp(-jr\beta N)z^{-1}] = \sum_{r=0}^{\kappa-1} d_{2r}z^{-r}$; $P_3(z) = \prod_{k=1}^{\kappa}[1-\exp(jk\beta N)z^{-1}]$; and $P_4(z) = \prod_{k=1}^{\kappa}[1-\exp(-jk\beta N)z^{-1}]$. Taking into account the terms $D's$ and $P's$ and substituting them in Eq. (2.22), we obtain

$$\begin{aligned}\mathbf{I}(z) =& I_{dc}\left(\frac{1-z^{-N}}{1-z^{-1}}\right) + \\ &\left\{\frac{\sum_{k=1}^{\kappa} \ell_k'\left[\sum_{r=0}^{\kappa-1} d_{1r}z^{-r} - \sum_{r=0}^{\kappa-1} d_{1r}\exp(jk\alpha N)z^{-(r+N)}\right]}{\prod_{k=1}^{\kappa}[1-\exp(jk\alpha)z^{-1}]}\right\} + \\ &\left\{\frac{\sum_{k=1}^{\kappa} {\ell_k'}^*\left[\sum_{r=0}^{\kappa-1} d_{2r}z^{-r} - \sum_{r=0}^{\kappa-1} d_{2r}\exp(-jk\alpha N)z^{-(r+N)}\right]}{\prod_{k=1}^{\kappa}[1-\exp(-jk\alpha)z^{-1}]}\right\} + \\ &\left\{\frac{\sum_{k=1}^{\kappa} \wp_k\left[\sum_{r=0}^{\kappa-1} d_{3r}z^{-r} - \sum_{r=0}^{\kappa-1} d_{3r}\exp(jk\beta N)z^{-(r+N)}\right]}{\prod_{k=1}^{\kappa}[1-\exp(jk\beta)z^{-1}]}\right\} + \\ &\left\{\frac{\sum_{k=1}^{\kappa} {\wp_k'}^*\left[\sum_{r=0}^{\kappa-1} d_{4r}z^{-r} - \sum_{r=0}^{\kappa-1} d_{4r}\exp(-jk\beta N)z^{-(r+N)}\right]}{\prod_{k=1}^{\kappa}[1-\exp(-jk\beta)z^{-1}]}\right\}\end{aligned} \tag{2.23}$$

Equation (2.23) can be represented in a similar form as Eq. (2.6), where, $\mathbf{P}(z)$ the denominator in the right hand side of Eq. (2.23) is given by

$$\begin{aligned}\mathbf{P}(z) =&(1-z^{-1})\prod_{k=1}^{\kappa}[1-\exp(jk\alpha)z^{-1}][1-\exp(-jk\alpha)z^{-1}]\times \\ &[1-\exp(jk\beta)z^{-1}][1-\exp(-jk\beta)z^{-1}] \\ =&\sum_{k=0}^{4\kappa+1} p_k z^{-k}\end{aligned} \tag{2.24}$$

Given the complex form of $\mathbf{D}(z)$, let us consider for the sake of simplicity writing only its first term,

$$\begin{aligned}\mathbf{C_1}(z) =&\sum_{k=1}^{\kappa} I_{dc}(1-z^{-N})\mathbf{P_1}(z)\mathbf{P_2}(z)\mathbf{P_3}(z)\mathbf{P_4}(z) \\ =&\sum_{r=0}^{4\kappa}\mathbf{C1}_r z^{-r}-\sum_{r=0}^{4\kappa}\mathbf{C1}_{r+N}z^{-(r+N)}\end{aligned} \tag{2.25}$$

From Eq. (2.25) we observe that some coefficients of $\mathbf{C_1}(z)$, specifically, $\mathbf{C1}_0$, $\mathbf{C1}_1$, $\mathbf{C1}_2$,...,$\mathbf{C1}_{4\kappa}$, and $\mathbf{C1}_N$, $\mathbf{C1}_{N+1}$, $\mathbf{C1}_{N+2}$,...,$\mathbf{C1}_{N+4\kappa}$, depend upon the unknown amplitude and frequency. We observe that the coefficients $\mathbf{C1}_{4\kappa+1}$, $\mathbf{C1}_{4\kappa+2}$, $\mathbf{C1}_{4\kappa+3}$,...,$\mathbf{C1}_{N-1}$, are identically zero for $N \geq 4\kappa+1$. This condition is at the essence of the design of annihilating filter $\mathbf{P}(z)$. In what follows we show that the $(4\kappa+1)^{th}$ degree polynomial $\mathbf{P}(z)$, when discretely convolved with $\mathbf{I}(z)$ yields zero. As mentioned earlier, the multiplication of two signals in frequency domain corresponds to its discrete convolution in time domain, and its inverse Z-transform is given in Eq. (2.9), where, p_n is

$$p_n = p_0\delta(n)+p_1\delta(n-1)+p_2\delta(n-2)+.....+p_{4\kappa+1}\delta(n-4\kappa-1) \tag{2.26}$$

Equation (2.26) can be further written as

$$\sum_{k=0}^{4\kappa+1} I_{n-k}p_k = D_n;\ \text{ for } n=0,1,2,....,N,.....,N+4\kappa. \tag{2.27}$$

Again, using the fact in Eq. (2.12), we obtain

$$\left[\begin{array}{ccccc} I_0 & 0 & 0 & \dots & 0 \\ I_1 & I_0 & 0 & \dots & 0 \\ \cdot & \cdot & \cdot & \cdot & \cdot \\ \cdot & \cdot & \cdot & \cdot & \cdot \\ \hline I_{4\kappa+1} & I_{4\kappa} & 0 & \dots & I_0 \\ I_{4\kappa+2} & I_{4\kappa+1} & 0 & \dots & I_1 \\ \vdots & \vdots & \vdots & \vdots & \vdots \\ I_{N-2} & I_{N-3} & 0 & \dots & I_{N-4\kappa-3} \\ I_{N-1} & I_{N-2} & 0 & \dots & I_{N-4\kappa-2} \\ \hline 0 & I_{N-1} & I_{N-2} & \dots & \cdot \\ 0 & 0 & \cdot & \dots & \cdot \\ \cdot & \cdot & \cdot & \cdot & \cdot \\ 0 & \cdot & \cdot & \cdot & I_{N-2} \\ 0 & 0 & 0 & \dots & I_{N-1} \end{array}\right] \times \begin{bmatrix} p_0 \\ p_1 \\ p_2 \\ \vdots \\ p_{4\kappa+1} \end{bmatrix} = \left[\begin{array}{c} D_0 \\ D_1 \\ \cdot \\ D_{4\kappa} \\ \hline 0 \\ 0 \\ 0 \\ \cdot \\ 0 \\ \hline D_N \\ \cdot \\ D_{N+4\kappa} \end{array}\right] \tag{2.28}$$

We partition the first matrix on the left hand side of Eq. (2.28), select the middle $N-4\kappa-2$ rows equations corresponding to zero row values in the matrix on the right hand side, and form a new matrix as follows:

$$\underbrace{\begin{bmatrix} I_{4\kappa+1} & I_{4\kappa} & 0 & \dots & I_0(1) \\ I_{4\kappa+2} & I_{4\kappa+1} & 0 & \dots & I_1 \\ \vdots & \vdots & \vdots & \vdots & \vdots \\ I_{N-2} & I_{N-3} & 0 & \dots & I_{N-4\kappa-3} \\ I_{N-1} & I_{N-2} & 0 & \dots & I_{N-4\kappa-2} \end{bmatrix}}_{\mathbf{R}} \times \underbrace{\begin{bmatrix} p_0 \\ p_1 \\ p_2 \\ \vdots \\ p_{4\kappa+1} \end{bmatrix}}_{\mathbf{P}} = \begin{bmatrix} 0 \\ 0 \\ \vdots \\ \vdots \\ 0 \end{bmatrix} \tag{2.29}$$

We can infer from Eq. (2.29) that the polynomial $\mathbf{P}(z)$ is an annihilating filter which when convolved with the intensity signal yields zero. It can further be deduced that at least $N \geq 4\kappa+2$ samples are required to extract the roots of the polynomial $\mathbf{P}(z)$. This enables us to find the unknown values u_k and v_k. The phase steps α and β can hence be computed using $\alpha = \Re(\ln u_1/j)$ and $\beta = \Re(\ln v_1/j)$, respectively. The denoising procedure explained in Section 2.3 can further be applied to minimize the influence of noise occurring during the measurement. Next section presents application of annihilation filter method in the extraction of phases in holographic moiré .

2.6 Evaluation of Phase Step and Phase Distribution in Holographic Moiré

The annihilation filter designed in Section 2.5 is applied to the simulated moiré fringe so that the phase steps α and β; and subsequently the phase distributions φ_1 and φ_2 can be estimated by modifying the Vandermonde matrix presented in Section 2.4. Let us consider the following equation for the moiré fringe pattern

$$
\begin{aligned}
I(n', j'; n) = I_{dc} + & \sum_{k=-2}^{2} a_k \exp\left(j\left\{\frac{2\pi[(n'-n_0)^2+(j'-j_0)^2]}{\lambda_1\xi}+n\alpha\right\}\right)+ \\
& \sum_{k=-2}^{2} b_k \exp\left(j\left\{\frac{2\pi[(n'-p_0)^2+(j'-j_0)^2]}{\lambda_2\xi}+n\beta\right\}\right); \\
& \text{for } n = \; 0,1,2,....,N-1.
\end{aligned}
\tag{2.30}
$$

where,(n_0, j_0) is the origin of the $n' \times j'$ pixels for fringe pattern with pitch λ_1; (p_0, j_0) is the origin of the $N' \times J'$ pixels for fringe pattern with pitch λ_2; ξ is some arbitrary constant; $\kappa = 2$ and the phase steps are selected as $\alpha = \pi/4$ and $\beta = \pi/3$. A white Gaussian noise with SNR from 0 to 100 dB is added to test the robustness of the proposed concept. Fringes shown in Figures (2.4a),(2.4c), and (2.4e) correspond to Eq. (2.30) for $\kappa = 1$ and for three different noise levels. On the other hand, fringes shown in Figs. (2.4b),(2.4d), and (2.4f) corresponds to Eq. (2.30) for $\kappa = 2$ and for same noise levels as in Figs. (2.4a)-(2.4c), respectively. These fringes have been generated under the assumption $a_{0,\pm1,\pm2} = b_{0,\pm1,\pm2} = 0.5$.

Figure (2.5a) shows the plot for phase step extraction when the noise level is considered from 0 to 100 dB; eighteen data frames are used to obtain this plot. As can be seen from the plot, the phase steps cannot be accurately determined for SNR level below 40 dB. In order to extract the phase steps reliably at a lower SNR, additional data frames are mandatory so that denoising procedure explained in Section 5 can be successfully applied. Figures (2.5b) and (2.5c) show a plot for the phase step extraction when twenty seven and thirty six data frames are used in the computation of phase steps and denoising procedure is applied. The plot shows an increase in reliability in the computation of phase steps with a larger number of frames. Large data frames can induce unwanted noise in the measurement, if controlled environment is not used. Our denoising technique works well when random noise follows a Gaussian profile, which is the case most of time. For noise which does not follow a Gaussian profile (air turbulence, or vibrations), reference 30 provides an insight into the measures which can be taken to minimize their influence on the measurement of phase distribution.

Once the phase steps are estimated the parameters ℓ'_k and $\wp_k$ can be solved using the linear Vandermonde system of equations obtained from Eq. (2.20). The matrix thus obtained can be written as

$$
\begin{bmatrix}
\exp(j\kappa\alpha_0) & \exp(-j\kappa\alpha_0) & \exp(j\kappa\beta_0) & \cdot & \exp[j(\kappa-1)\alpha_0] & \dots & 1 \\
\exp(j\kappa\alpha_1) & \exp(-j\kappa\alpha_1) & \exp(j\kappa\beta_1) & \cdot & \exp[j(\kappa-1)\alpha_1] & \dots & 1 \\
\vdots & \vdots & \vdots & \vdots & \vdots & \vdots & \vdots \\
\exp[j\kappa\alpha_{(N-1)}] & \exp[-j\kappa\alpha_{(N-1)}] & \exp[j\kappa\beta_{(N-1)}] & \cdot & \exp[j(\kappa-1)\alpha_{(N-1)}] & \dots & 1
\end{bmatrix} \times
$$

$$
\begin{bmatrix} \ell_\kappa \\ \ell_\kappa^* \\ \wp_\kappa \\ \vdots \\ I_{dc} \end{bmatrix}
=
\begin{bmatrix} I_0 \\ I_1 \\ I_2 \\ \vdots \\ I_{N-1} \end{bmatrix}
\tag{2.31}
$$

where, (α_1, β_1), (α_2, β_2),..,(α_N, β_N) are phase steps in frames I_0, I_1, I_2,...,I_{N-1}, respectively. The

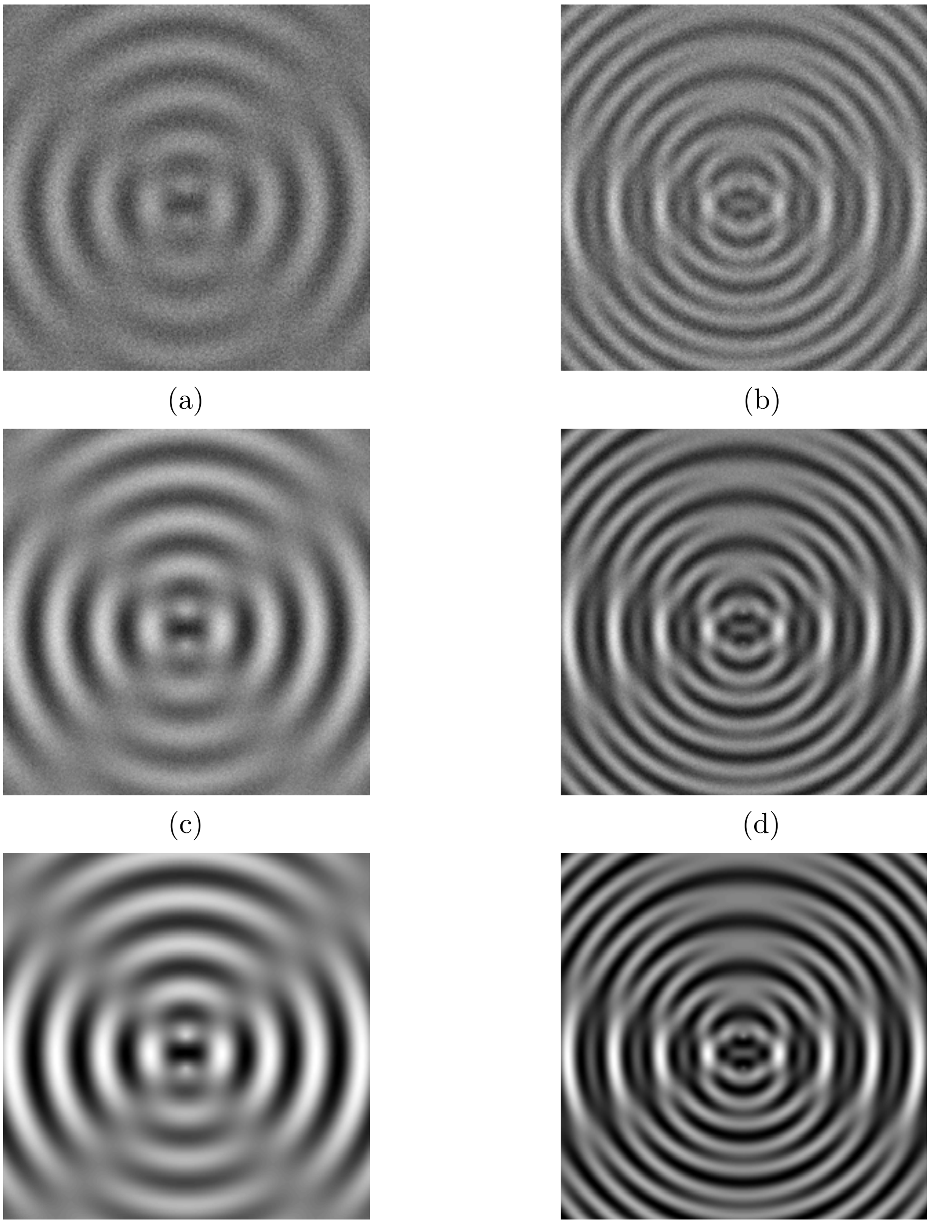

(a) (b) (c) (d) (e) (f)

Fig. 2.4: Holographic moiré for $\kappa = 1$ and SNR (a) 0 dB, (c) 10 dB, (e) 60 dB, and for $\kappa = 2$ and SNR (b) 0 dB, (d) 10 dB, and (f) 60 dB additive white Gaussian noise.

phases φ_1 and φ_2 are subsequently computed from the argument of ℓ_1' and $\wp_1$. Figures (2.6a) and (2.6b) show typical errors in the computation of phase φ_1, without and with denoising step, respectively, and assuming a SNR of 30 dB.In this simulation phase steps obtained in Fig. (2.5c) are used for the computation of phases. Similarly Figs. (2.7a) and (2.7b) show errors in the computation of phase φ_1 without and with the application of the denoising step, respectively, all the other parameters remaining the same. Figure (2.8) shows the wrapped phases obtained with the denoising step.

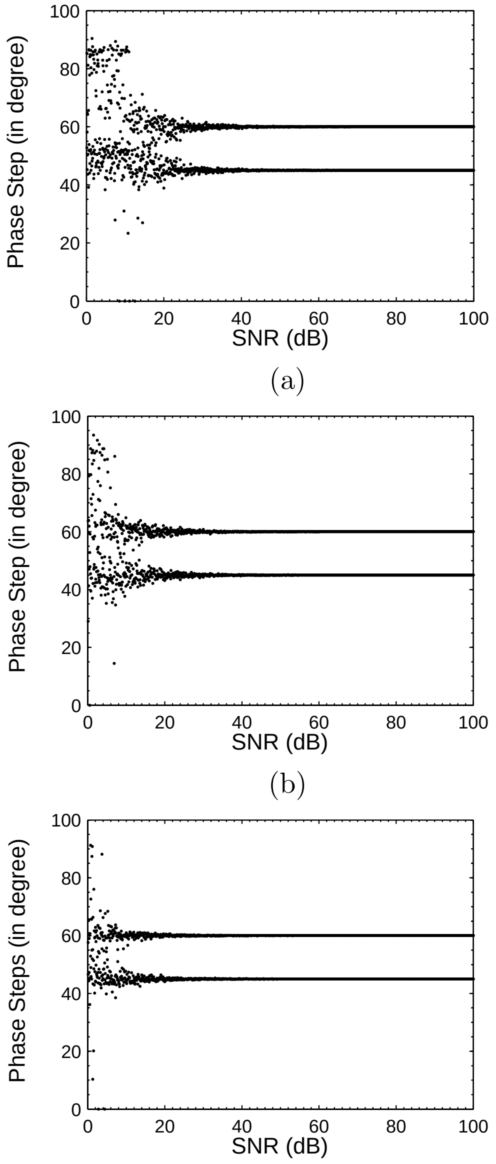

(a)

(b)

(c)

Fig. 2.5: Plot of phase steps α and β versus SNR when computation is done over (a) eighteen (b) twenty seven, and (c) thirty six frames. Plots in (b) and (c) are obtained after applying the denoising procedure. Large number of frames are due to the presence of two PZTs $H = 2$ and two harmonics $\kappa = 2$, which in turn impose lower limit on data samples $(4H\kappa + 2)$ as eighteen for phase step estimation.

2.7 Discussion on Annihilation Filter Method

To conclude, we have presented a novel integral approach - based on the use of a super-resolution frequency estimation method - to phase shifting interferometry, starting from phase step estimation to phase evaluation at each point on the object surface. A significant advantage of this approach is that it also offers the possibility to identify the harmonic content of the signal. The described method holds promise for determining simultaneously multiple phase distributions in

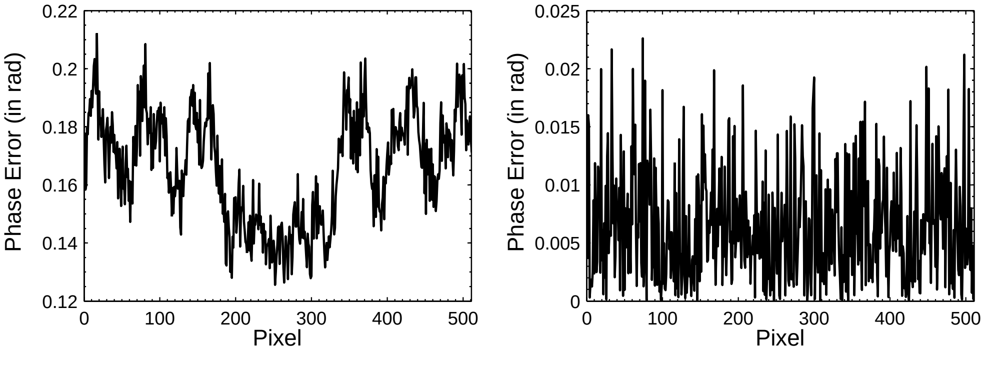

(a) (b)

Fig. 2.6: Plot of error in the computation of phase φ_1 when SNR = 30 dB obtained a) without and b) with the application of the denoising procedure.

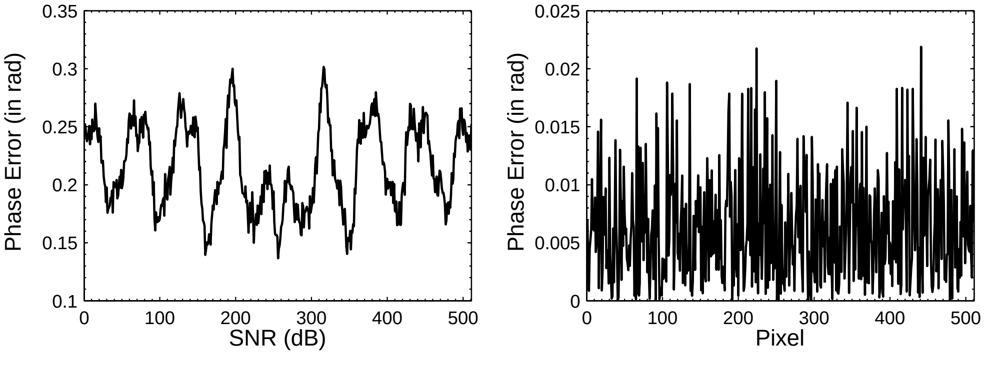

(a) (b)

Fig. 2.7: Plot of error in the computation of phase φ_2 when SNR = 30 dB obtained a) without and b) with the application of the denoising procedure.

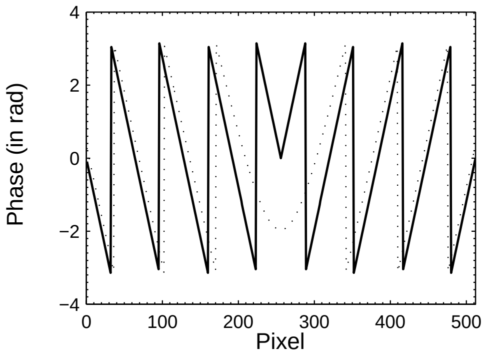

Fig. 2.8: Wrapped phase distributions φ_1 (solid line) and φ_2 (broken line) as functions of pixel position when SNR = 30 dB. Denoising procedure has been applied for obtaining these results.

the presence of higher order harmonics and in optical configurations with multiple PZTs. The technique works well with the spherical beams since the phase steps are retrieved pixel-wise. The robustness of the algorithm to white Gaussian noise is enhanced by the incorporation of a denoising step before the extraction of the phase step.

Chapter 3

A State Space Approach in Phase Shifting Interferometry

The previous chapter dealt with the design of an annihilation filter for the estimation of multiple phase information. However, the method works directly on the signal matrix [Eqs. (2.14) and (2.29)]. Since numerically robust tools such as eigenvalue decomposition can be applied on the covariance matrix for the estimation of phase steps, the design of a covariance matrix is liable to yield better results than the direct polynomial rooting method. This chapter presents first, a state space approach for the estimation of phase steps pixelwise and second, a improved denoising method so that the phase steps could be better estimated even at low SNR's. In this chapter, we apply the state space approach to estimate phase from an interferogram before extending it to estimating multiple phases in holographic moiré .

3.1 Introduction

The state space approach presented in this chapter consists of forming a state-feedback matrix following a low rank approximation of the Toeplitz covariance matrix obtained via singular value decomposition (SVD). The Toeplitz covariance matrix is formed from the intensity fringes recorded temporally at a pixel (n', j') on the CCD. The state space approach explores a numerically robust technique such as eigen decomposition of a well-conditioned state feedback matrix for estimating the phase steps pixel-wise as compared to the classical polynomial (annihilation filter) method which requires polynomial rooting [1,108] for estimating the same quantity. Besides being a direct estimation method, the state space approach is superior to polynomial rooting method at least as far as its performance in estimating spectral frequencies is concerned [2]. The approach shows the effect of an increase in the number of data frames in retrieving the phase information in the presence of noise. A novel denoising procedure is presented which yields a precise estimation of the phase step values, and in consequence an improved phase estimation at low signal to noise ratios.

3.2 State Space Realization

In state space approach, the first step involves retrieving the phase step imparted to the PZT. The fringe intensity recorded at a pixel (n', j') for n^{th} phase step in an optical configuration involving single PZT in the presence of Gaussian noise is given by Eq. (2.1). State space approach is based on the foundation of the design of an annihilation filter and Eqs. [(2.3) - (2.9)] holds the key in understanding the state space approach. Recall that the polynomial $\mathbf{P}(z)$ in Eq. (2.7) when discretely convolved with $\mathbf{I}(z)$ yields zero, where $\mathbf{I}(z)$ is the Z-transform of I_n. The inverse Z-transform of this fact is given in Eq. (2.9). Further closer look at Eqs. (2.3) - (2.9) reveals that

$$\begin{aligned} 0 =& I_n - \sum_{k=1}^{\kappa} I(n-k)\rho_k \\ I_n =& \sum_{k=1}^{\kappa} I(n-k)\rho_k \\ & \text{for } n = \ 2\kappa+1, 2\kappa+2, ..., 4\kappa+2. \end{aligned} \tag{3.1}$$

Note that for the sake of convenience we are interchangeably using the subscript n (denoted as I_n and index n (denoted as $I(n)$). It can be inferred from Eq. (3.1) that the intensity at the n^{th} data frame can be predicted from its past p samples. Therefore, in the absence of the noise, the exponential signal such as the one in Eq. (2.1) is exactly predictable as a linear combination of its past $p = 2\kappa + 1$ samples given by

$$I_n = \sum_{k=1}^{p} \rho_k I(n-k) \tag{3.2}$$

Hence, this linear prediction formulation converts the nonlinear problem of frequency estimation to the linear parameter estimation problem where parameters ρ_1, ρ_2,...,ρ_p are to be estimated. Usually, the parameters ρ_1, ρ_2,...,ρ_p can be estimated using the classical methods such as the annihilation filter [1] or the transfer function parameterization [2]. On the contrary the state space approach uses more robust tools such as eigenvalue decomposition of well-conditioned matrices to extract the desired quantities. Also, the advantage of the state space approach lies in its ability to indicate the harmonics present in the intensity signal unlike the polynomial rooting method where *a priori* knowledge of the number of the harmonics is necessary.

In state space representation, the phase step can be estimated [115] by designing a state vector $\mathbf{I}(n)$ consisting of past p data frames:

$$\mathbf{I}(n) = \begin{bmatrix} I(n-1) & I(n-2) & I(n-3) & \dots & I(n-p) \end{bmatrix}^T \tag{3.3}$$

Using the state space vector and the linear predictability of the sinusoidal signals, the state propagation equation can be written as [2]

$$\mathbf{I}(n+1) = \mathbf{F}\mathbf{I}(n) \tag{3.4}$$

and the output equation as

$$I(n) = \mathbf{H}\mathbf{I}(n) \tag{3.5}$$

where $\mathbf{F}$ and $\mathbf{H}$, the state transition and observation matrices, respectively, are given by

$$\mathbf{F} = \begin{bmatrix} \rho_1 & \rho_2 & \dots & \rho_p \\ 1 & 0 & \dots & 0 \\ 0 & 1 & \dots & 0 \\ \vdots & \vdots & \vdots & \vdots \\ 0 & 0 & 0 & 0 \end{bmatrix} \text{and } \mathbf{H} = \begin{bmatrix} \rho_1 & \rho_2 & \dots & \rho_p \end{bmatrix} \tag{3.6}$$

The eigenvalues of **F** contain the information regarding the phase step applied to the PZT. In fact, we have $I(n) = \mathbf{HF}^n\mathbf{I}(0)$, $n \geq 0$, for some non zero initial condition $\mathbf{I}(0)$ and the covariance $r(a) = \mathbf{HF}^a\mathbf{PH}^T$, $a \geq 0$, where **P** is the state-covariance matrix. It can also be shown that $\mathbf{P} = \mathbf{FPF}^T$ and $r(-a) = \mathbf{HF}^{-a}\mathbf{PH}^T$. Therefore, the Toeplitz covariance matrix can be formulated from $r(a)$ and $r(-a)$ as

$$\mathbf{R} = \begin{bmatrix} r(0) & r(-1) & \dots & r(-L) \\ r(1) & r(0) & \dots & r(-L+1) \\ \vdots & \vdots & \vdots & \vdots \\ r(L) & r(L-1) & \dots & r(0) \end{bmatrix} \tag{3.7}$$

The matrix in Eq. (3.6) can be factored as

$$\mathbf{R} = \underbrace{\begin{bmatrix} \mathbf{H} \\ \mathbf{HF} \\ \vdots \\ \mathbf{HF}^L \end{bmatrix}}_{\Theta} \underbrace{\begin{bmatrix} \mathbf{PH}^T & \mathbf{F}^{-1}\mathbf{PH}^T & \dots & \mathbf{F}^{-L}\mathbf{PH}^T \end{bmatrix}}_{\Psi} \tag{3.8}$$

From Eq. (3.7), we observe that the χ^{th} row of Θ is $\mathbf{HF}^{\chi-1}$ and the χ^{th} column is $\mathbf{F}^{-\chi+1}\mathbf{PH}^T$. Thus, **F** can be obtained by solving the overdetermined system of equations $\Theta_1\mathbf{F} = \Theta_2$, where $\Theta_1(\Theta_2)$ is obtained by deleting first (last) row of Θ. The phase step α is evaluated from the eigenvalues of **F**. However, the estimation of phase step can be improved at lower SNR by incorporating a denoising procedure different from the one proposed earlier [1]. Next section discusses the denoising procedure.

3.3 Denoising in State Space Approach

The presence of Gaussian noise perturbs the eigenvalues. This is contrary to the eigenvectors which are insensitive to the noise. It is also observed that the eigenvalues are shifted by a fixed quantity, σ^2 (noise variance), and hence if this quantity is removed before computing the eigenvalues of **F**, a better estimate for phase step can be obtained. In our modified approach, we first form the Toeplitz covariance matrix shown in Eq. (3.6). The eigendecomposition of this matrix yields, $\mathbf{R} = \mathbf{USV}^T$, where **U** and **V** are unitary matrices, such that $\mathbf{UU}^T = \mathbf{I} = \mathbf{VV}^T$, where **I** is the identity matrix. The diagonal values of the **S** matrix show some entries that are substantial in magnitude as compared to the rest of the entries. These high values are in fact indicative of the number of frequencies present in an interferogram. For instance, for $\kappa = 2$, we observe five entries $(\lambda_0 > \lambda_1 > ..., \lambda_4)$ which are significant in magnitude while the rest ($\lambda_5 > \lambda_6 > ..., \lambda_{L-1}$) are equal to zero for the noiseless case. In the presence of noise, the principal entries are shifted as ($\lambda_0 + \sigma^2 > \lambda_1 + \sigma^2 > ..., \lambda_4 + \sigma^2$) , while the rest are ($\lambda_5 \approx \lambda_6 \approx ..., \lambda_{L-1} \approx \sigma^2$). Hence we first compute the mean of the nonsignificant entries in the matrix as $1/(L-p)\sum_{d=p+1}^{L-1}\lambda_d$. This mean is subtracted from the diagonal entries of the $\mathbf{S}$ matrix and a new matrix $\hat{\mathbf{S}}$ is designed. Finally a denoised matrix $\hat{\mathbf{R}} = \mathbf{U}\hat{\mathbf{S}}\mathbf{V}^T$ is constructed. The rest of the procedure for determining the eigenvalues of $\mathbf{F}$ is then followed. A slightly different approach has been suggested by us in [1].

Figure (3.1a) shows the eigenvalues for the $\mathbf{S}$ matrix for pure and noisy intensity signal,(SNR = 10dB), where we have chosen $\alpha = \pi/4$ and $\kappa = 1$ in Eq. (2.2). In the plot three principal values indicate $\kappa = 1$. The plot shows that the eigenvalues for the noisy signal is raised as compared to the pure signal. Figure (3.1b) shows the mean squared error in the computation of the phase step α without applying the denoising procedure and with applying the denoising procedure presented in this paper. For this plot, Monte-Carlo simulation is performed with 500 realizations at each and for $N = 12$. The study shows an improvement in the performance using the present approach for SNR = 6dB and above as compared to our previously suggested denoising procedure. In normal experiments, the SNR can be expected to lie between 10 to 30dB.

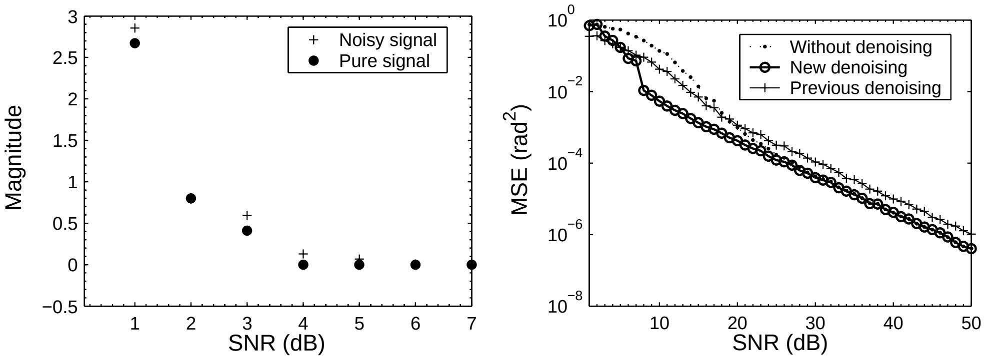

(a) (b)

Fig. 3.1: Plot shows a) eigenvalues for the $\mathbf{S}$ matrix for pure and noisy (SNR = 10 dB) intensity signal, b) mean squared error (MSE) in the computation of phase step versus SNR; without denoising, with a modified denoising procedure, and with the denoising procedure in Reference [1]

3.4 State Space Approach for Phase Step and Phase Estimation

This section shows the feasibility of the proposed concept. For this we study the influence of noise on the extraction of phase step by simulating a fringe pattern. The phase step is chosen as $\alpha = \pi/4$. The analysis is performed for $\kappa = 1$ and $\kappa = 2$. The fringe pattern is generated using Eq. (1.5). Since the number of frequencies in the signal, for $\kappa = 1$, we get $f = 3$ (corresponding to 0, and $\pm\alpha$), the minimum number of data frames required is $N = 6$. Similarly, for $\kappa = 2$, we have $f = 5$ (corresponding to 0, $\pm\alpha$, and $\pm 2\alpha$), the minimum number of data frames required is $N = 10$. However, the presence of noise necessitates acquiring more number of data frames to extract phase steps at lower SNRs. Figures (3.2a)-(3.2f) show the influence of the number of data frames on estimating the phase step value at a pixel for SNR = 0 to 70 dB and for $\kappa = 1$ and $\kappa = 2$. The simulations are performed for values of SNR between 0 and 70 dB in steps of

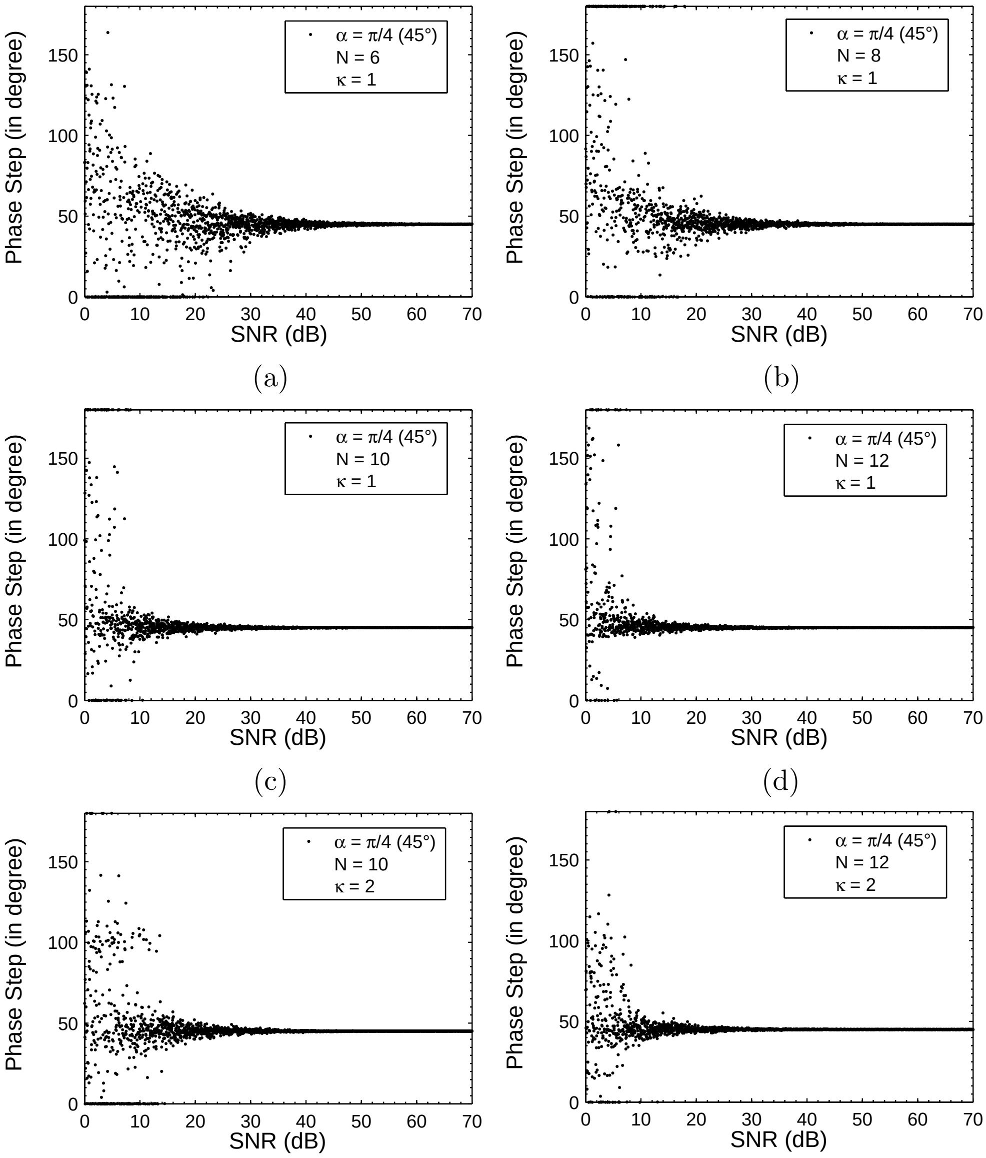

(a) (b) (c) (d) (e) (f)

Fig. 3.2: Plot of phase step α (in degree) versus SNR using Eq. (3.7) at an arbitrary pixel location on a data frame for $\kappa = 1$ and $\kappa = 2$ for different number of data frames. The phase step α is assumed to be 45° during the simulation.

SNR = 0.3 dB. Figure (3.2a) shows that the phase step can be estimated reliably for SNR = 50 dB and above for $N = 6$, while as the number of data frames increases, for instance $N = 6$, 8, and 12, the phase steps can be extracted for SNR = 45, 30 and 25 dB and above, respectively. These results are shown in Figs. (3.2b)-(3.2d). Figures (3.2e)-(3.2f) show the estimation of phase step for $\kappa = 2$. We observe that $N = 12$ frames are sufficient for the estimation of phase step at SNR = 30 dB and for second order harmonics. Once, the phase step has been estimated linear Vandermonde system of equations as defined in Eq. (2.18) can be designed to estimate the wrapped phase. The mean squared error in computation of wrapped phase will be explained in Chapter 9.

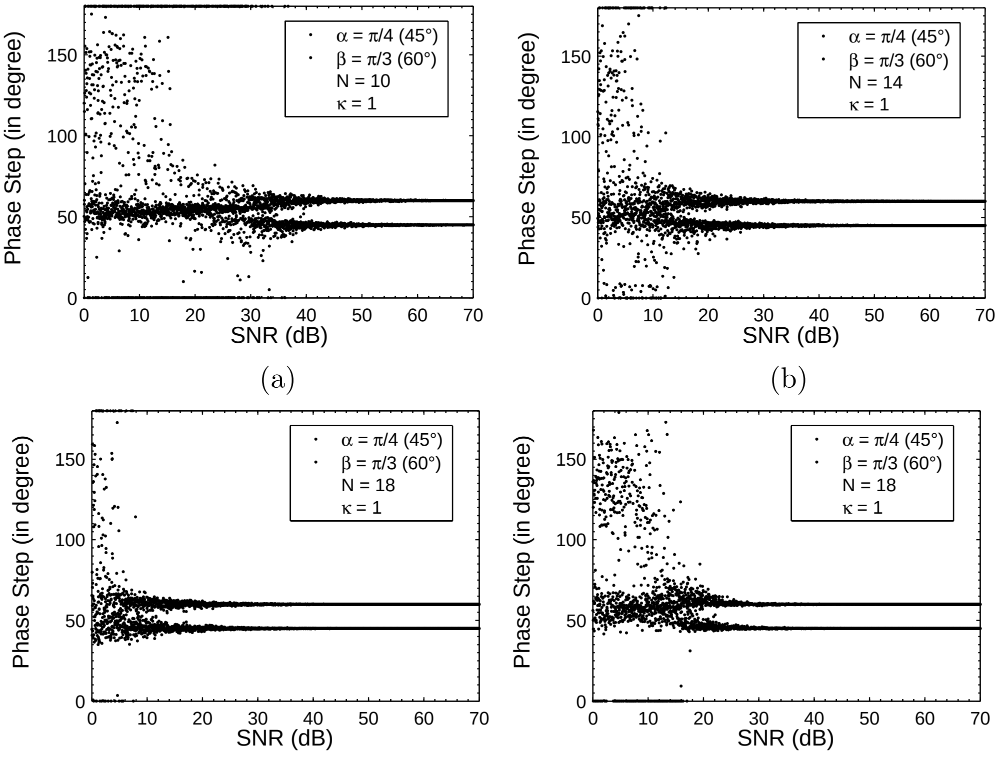

(a) (b)

(c) (d)

Fig. 3.3: Plots of phase steps α and β (in degree) for the number of data frames: a) 10, b) 14, c) 18 (with modified denoising method, and d) 18 [original Toeplitz approximation method (TAM) [2]] with respect to SNR.

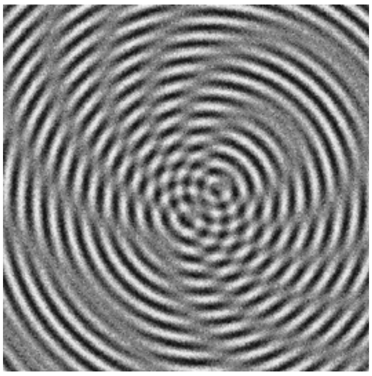

Fig. 3.4: Example of a holographic moiré fringe map.

3.5 State Space Approach for Dual Phase Step and Multiple Phase Estimation in Holographic Moiré

The concept of state space approach presented in Section 3.2 is extended further to retrieve phases in the two arms of a holographic moiré interferometer. During the analysis, Eq. (2.19) is considered for holographic moiré . Initially, the Toeplitz covariance matrix given in Eq. (3.6) is formulated from a moiré recorded temporally at pixel (n', j') on the CCD. The procedure

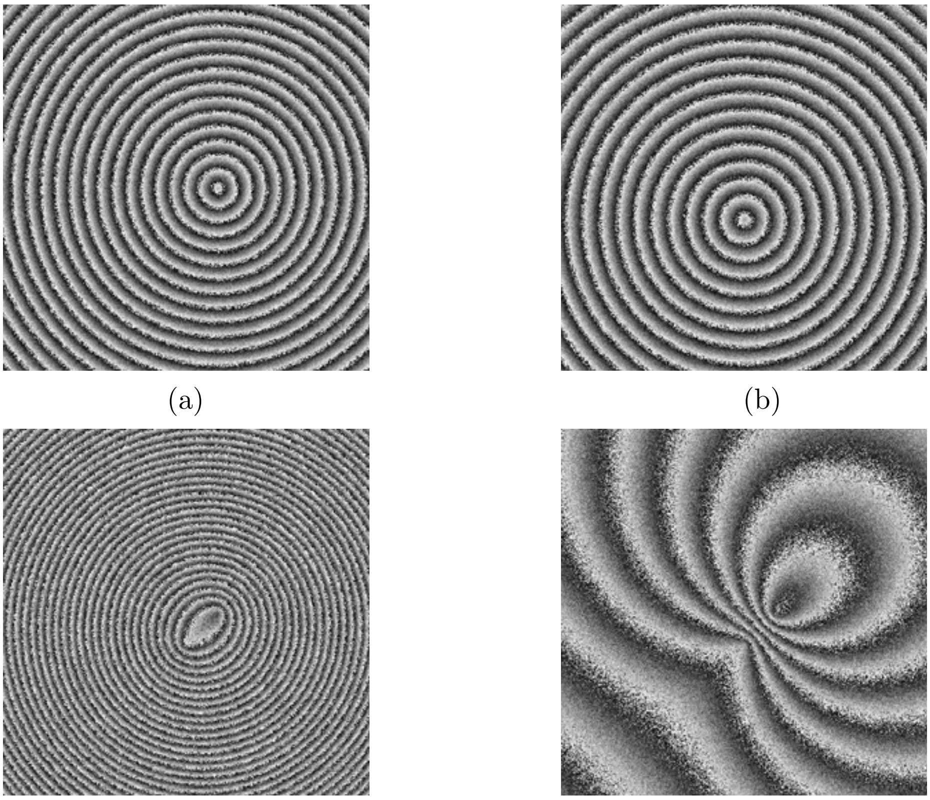

(a) (b)

(c) (d)

Fig. 3.5: Wrapped phase distribution corresponding to a) phase φ_1 b) phase φ_2 c) sum of phases $\varphi_1 + \varphi_2$, and d) difference of phases $\varphi_1 - \varphi_2$.

explained in Section 3.2 is then followed for the estimation of multiple phase steps α and β, followed by applying a linear Vandermonde system of equation in Eq. (2.31) for the estimation of φ_1 and φ_2. During the simulation, in Eq. (2.19), the phase steps are selected as $\alpha = \pi/4$ and $\beta = \pi/3$, and harmonics $\kappa = 1$. The results in the estimation of phase steps obtained using the proposed approach is shown in Fig. (3.3). In fact, only $N = 10$ data frames are required for moiré setup consisting of two PZT's and for $\kappa = 1$ (since $f = 4\kappa + 1 = 5$). However, the presence of noise necessitates acquiring $N > 10$ frames. Figures (3.3a)-(3.3c) show the influence of increase in the number of data frames on the retrieval of phase steps using our approach. As the number of data frame increases, the phase steps can be reliably estimated at lower SNR's. For instance, Fig. (3.3c) shows that the phase steps can be estimated reliably from 28 dB onward, as compared with 38 dB onward in Fig. (3.3b). Figure (3.3d) shows that the phase steps obtained using the original state space method for $N = 18$. From Figs. (3.3c) and (3.3d) it can be clearly seen that the modified approach performs better than the original method.

The phases φ_1 and φ_2 can then be estimated using the linear Vandermonde system of equations given by Eq. (2.31). Figure (3.4) shows a moiré obtained using Eq. (2.19), for SNR = 30 dB and also assuming random phases. Figures (3.5a) and (3.5b) shows the wrapped phase map for φ_1 and φ_2, respectively. Figures (3.5c) and (3.5d) shows the wrapped phase map corresponding to $\varphi_1 + \varphi_2$, and $\varphi_1 - \varphi_2$, respectively. Recall that $\varphi_1 + \varphi_2$ and $\varphi_1 - \varphi_2$, yields the out-of-plane and in-plane displacement components, respectively. Note that $\varphi_1 + \varphi_2$ and $\varphi_1 - \varphi_2$ is obtained from the arguments of $\ell_1\wp_1$ and $\ell_1/\wp_1$, respectively, obtained from Eq. (2.31). The error in the computation of phases φ_1 and φ_2 will be considered in Chapter 9.

3.6 Discussion on State Space Approach

To conclude, we have proposed a novel approach to extract multiple phases in holographic moiré . The sum and difference of phases yield simultaneously the information regarding the out-of-plane and in-plane displacement components. The proposed method offers the flexibility to use multiple PZT's and overcomes the restriction of using fixed phase steps to minimize a particular order harmonics. The modified denoising procedure ensures estimation of phase steps at much lower SNRs as compared to the method suggested in Reference [1]. The use of non-collimated beams is also possible.

Chapter 4

Multiple Signal Classification Technique for Phase Shifting Interferometry

The concepts based on the design of an annihilation filter or that on the state space approach require incorporation of a denoising procedure and which therefore add to the computational cost. Hence, there is a need to eliminate the denoising step and extract the phase information directly from the intensity data recorded temporally at (n', j') pixel of a CCD. One of the approaches can be to work directly on the matrices (*signal* - and *noise subspaces*) obtained from the eigenvalue decomposition of the covariance data matrix. Since, the size of the *noise subspace* is more than that of the *signal subspace*, it would seem more logical to extract the information available from the *noise subspace.* This chapter presents one such method based on MUltiple SIgnal Classification technique (MUSIC) which derives phase steps from the *noise subspace* in the presence of noise. Once the phase steps are estimated pixelwise, the phase information can be derived as in chapter 2.

4.1 Introduction

MUSIC, a subspace based method [116, 117] has been successfully used to estimate the frequencies of sinusoids corrupted with white noise. Drawing upon the parallelism between the frequencies present in the spectrum and the phase shifts applied to the PZT, the MUSIC offers an innovative means of estimating the phase step at each pixel point. The method is based on the canonical decomposition of a positive definite Toeplitz matrix formed by an estimated autocorrelation sequence. The sequence corresponding to the phase shifted intensity images buried in white noise is acquired temporally. This decomposition yields a significant result as far as the estimation of frequency is concerned. Since the frequencies are estimated using the eigendecomposition of the autocorrelation matrix, the method is referred as *subspace method.* Although spectrum estimation can be handled efficiently by Fourier transform, resolution of closely spaced frequencies in the presence of noise is troublesome with limited number of data samples [109].The technique shows the effect of an increase in the number of data frames in retrieving the phase information in the presence of noise. However, selection of proper covariance length is paramount in obtaining accurate phase steps. In this context the technique also shows that design of sample covariance matrix using the *forward-backward* approach yields better result than the *forward*-approach.

4.2 Subspace-based Multiple Signal Classification Technique

In MUSIC, intially the phase step imparted to the PZT is retrieved followed by the estimation of phase. The fringe intensity recorded at a pixel (n', j') for n^{th} phase step in an optical configuration involving single PZT in the presence of Gaussian noise is given by Eq. (2.1). First step consists of forming the covariance or autocorrelation matrix from N recorded phase shifted sequences. The covariance of signal $I(n)$ in Eq. (2.1) is defined as [118]

$$r(p) = E[I(n)I^*(n-p)] = \sum_{k=0}^{2\kappa} A_k^2 exp(j\omega_k p) + \sigma^2 \delta_{p,0} \tag{4.1}$$

where, $E[\cdot]$ represents the expectation operator with averages over the ensemble of realizations; the terms A_0^2, A_1^2,....,$A_{2\kappa}^2$ are explained in Appendix A, σ^2 is the variance, and $\delta_{p,0}$ is the Kronecker delta ($\delta_{g,h} = 1$, if $g = h$; and $\delta_{g,h} = 0$ otherwise). The reader is referred to Appendix A for the derivation of Eq. (4.1). The covariance of function $I(n)$ is assumed to depend only on the lag between the two averaged samples. The covariance matrix can thus be written as [116–118]

$$\mathbf{R}_I = E[\mathbf{I}^c(n)\mathbf{I}(n)] = \begin{bmatrix} r(0) & r^*(1) & \cdot & \cdot & r^*(m-1) \\ r(1) & r(0) & \cdot & \cdot & \cdot \\ \cdot & \cdot & \cdot & \cdot & \cdot \\ \cdot & \cdot & \cdot & \cdot & r^*(1) \\ r(m-1) & \cdot & \cdot & \cdot & r(0) \end{bmatrix} \tag{4.2}$$

where, $\mathbf{I}(n) = [I(n-1) \ \cdots \ I(n-m)]$, m is the covariance length, and $(\cdot)^c$ is the conjugate transpose of a vector or a matrix. The covariance matrix $\mathbf{R}_I$ can be shown to have the form

$$\mathbf{R}_I = \underbrace{\mathbf{APA}^c}_{\mathbf{R}_s} + \underbrace{\sigma^2\mathbf{I}}_{\mathbf{R}_\varepsilon} \tag{4.3}$$

where, $\mathbf{R}_s$ and $\mathbf{R}_\varepsilon$ are the signal and noise contributions, $\mathbf{A}_{m\times 2\kappa+1} = [\mathbf{a}(\omega_0) \ \cdots \ \mathbf{a}(\omega_{2\kappa})]$, where for instance element $\mathbf{a}(\omega_0)$ consists of $m \times 1$ matrix with unity entries corresponding to I_{dc}; $\mathbf{a}(\omega_1) = [1 \ \exp(j\alpha) \ \cdots \ \exp(j\alpha_{(m-1)})]^T$, $\mathbf{I}$ is the $m \times m$ identity matrix; and $\mathbf{P}_{(2\kappa+1)\times(2\kappa+1)}$ matrix is

$$\mathbf{P} = \begin{bmatrix} A_0^2 & 0 & \cdot & \cdot & 0 \\ 0 & A_1^2 & \cdot & \cdot & \cdot \\ \cdot & \cdot & \cdot & \cdot & \cdot \\ 0 & \cdot & \cdot & \cdot & A_{2\kappa}^2 \end{bmatrix} \tag{4.4}$$

Since $\mathbf{R}_I$ is positive semidefinite, its eigen values are nonnegative. The eigenvalues of $\mathbf{R}_I$ can be ordered as $\lambda_1 \geq \lambda_2 \geq \cdots \geq \lambda_f \geq \cdots \geq \lambda_m$. Let $\mathbf{S}_{(m\times f)} = [\mathbf{s}_1 \ \mathbf{s}_2 \cdot\cdot \mathbf{s}_f]$ be the orthonormal eigenvectors associated with $\lambda_1 \geq \lambda_2 \geq \cdots \geq \lambda_f$. The space spanned by $\{\mathbf{s}_1, \mathbf{s}_2, ..., \mathbf{s}_f\}$ is known as *signal subspace*. The set of orthonormal eigenvectors $\mathbf{G}_{m\times(m-f)} = [\mathbf{g}_1 \ \mathbf{g}_2 \cdot\cdot \mathbf{g}_{m-f}]$ associated with eigenvalues $\lambda_{f+1} \geq \lambda_{f+2} \geq \cdots \geq \lambda_m$ spans a subspace known as *noise subspace*.

Since $\mathbf{APA}^c \in \mathbb{C}^{m \times m}$ ($\mathbb{C}$ represents complex matrix) has rank f ($f < m$), it has f eigenvalues and the remaining $m - f$ eigenvalues are zero. If we further suppose that (λ, r) is an eigenpair of $\mathbf{L} \in \mathbb{C}^{m \times m}$ and $\mathbf{W} = \mathbf{L} + \rho\mathbf{I}$ with $\rho \in \mathbb{C}$, then $(\lambda + \rho, r)$ is an eigenpair of $\mathbf{W}$, and in consequence we obtain $lambda = \tilde{\lambda_n} + \sigma^2$, where n spans from $1, 2, 3, \cdot\cdot, m$. We observe that $\lambda_1 \geq \lambda_2 \geq \cdots \geq \lambda_f \geq \sigma^2$ and $\lambda_{f+1} = \lambda_{f+2} = \cdots = \lambda_m = \sigma^2$. Following this corollary and from Eq. (4.3) we get

$$\mathbf{R}_I\mathbf{G} = \mathbf{G}\begin{bmatrix} \lambda_{f+1} & 0 & \cdot & \cdot & 0 \\ 0 & \lambda_{f+2} & \cdot & \cdot & \cdot \\ \cdot & \cdot & \cdot & \cdot & \cdot \\ 0 & \cdot & \cdot & \cdot & \lambda_m \end{bmatrix} = \sigma^2\mathbf{G} = \mathbf{APA}^c\mathbf{G} + \sigma^2\mathbf{G} \tag{4.5}$$

Last equality in Eq. (4.5) means that $\mathbf{APA}^c\mathbf{G} = 0$ and since $\mathbf{AP}$ has full column rank, we have $\mathbf{A}^c\mathbf{G} = 0$. This means that sinusoidals $\{\mathbf{a}(\omega_k)\}_{k=0}^{f}$ are orthogonal to *noise subspace.* This can be stated as $\sum_{k=m-f}^{m} \mathbf{a}^c(\omega)\mathbf{G}_k = 0$. Hence, true frequencies $\{\omega_k\}_{k=0}^{f}$ are the only solutions to the equation $\mathbf{a}^T(\omega)\mathbf{G}\mathbf{G}^c\mathbf{a}(\omega) = \parallel \mathbf{G}^c\mathbf{a}(\omega) \parallel^2 = 0$ for $m > f$. Here, $(\cdot)^T$ represents transpose of a matrix. Since, in practice, only the estimate $\hat{\mathbf{R}}_I$ of $\mathbf{R}_I$ is available, only the estimate $\hat{\mathbf{G}}$ of $\mathbf{G}$ can be determined. In the present study we employ *root* MUSIC [116, 117] which computes the frequencies as angular positions of f roots of the equation

$$\mathbf{a}^T(z^{-1})\hat{\mathbf{G}}\hat{\mathbf{G}}^c\mathbf{a}(z) = 0 \tag{4.6}$$

that are nearest and inside the unit circle. Here, $\mathbf{a}(z)$ is obtained from $\mathbf{a}(\omega)$, and by replacing $\exp(j\omega)$ by z we get $\mathbf{a}(z) = [1 \; z^{-1} \; \cdot \; \cdot z^{-(m-1)}]^T$. Since the minimum possible value of m is $f + 1$, from Eq. (4.6) it can be observed that we need data frames (N) that are at least twice the number of sinusoidal components in the signal. Hence, if $\kappa = 2$, which means $f = 5$, we need at 10 least data frames (the dc component is counted as dc frequency). Hence, the minimum number of data frames required while using MUSIC method for phase extraction is $4\kappa + 2$.

To apply MUSIC for estimating the phase steps α and β, one first needs to find out the number of harmonics present in the signal so that appropriate values of f is determined. The selection of m and N will be explained in next section. The method to determine f has been explained earlier in section 2.2.

4.3 Evaluation of the MUSIC Technique

The technique is tested by simulating the fringe pattern in Eq. (1.5) for the extraction of phase step α and subsequent phase φ [119]. During the simulation the phase step is chosen as $\alpha = \pi/4$. The analysis is performed for $\kappa = 2$. Since the number of frequencies in the signal, for $\kappa = 2$, we have $f = 5$, and thus the minimum number of data frames required is $N = 10$. However, the presence of noise necessitates acquiring more number of data frames to extract phase steps at lower SNRs. In practice, only the estimate of $\mathbf{R}_I$, represented as $\hat{\mathbf{R}}_I$, of a covariance matrix in Eq. (4.2) is known and the sample covariance matrix is designed using [120]

$$\hat{\mathbf{R}}_I = \frac{1}{N}\sum_{n=m}^{N}\begin{bmatrix} I^*(n-1) \\ I^*(n-2) \\ \cdot \\ \cdot \\ I^*(n-m) \end{bmatrix}\begin{bmatrix} I(n-1) & I(n-2) & \cdot & \cdot & I(n-m) \end{bmatrix} \tag{4.7}$$

which is as close as possible to $\mathbf{R}_I$ in Eq. (4.2) in least squares sense. The method which obtains the frequency estimates from $\hat{\mathbf{R}}_I$ given in Eq. (4.2) are called *forward approach.* We first discuss retrieving the phase step α in the presence of additive white Gaussian noise with SNR between 0 and 70 dB. Assuming that the number of frequencies $f = 5$ is known using the method suggested in section 2.2, hence, the number of data frames N for extracting the phase step values is 10. Subsequently, an appropriate value of m must be selected such that $N > m > f$. It is observed that $m > f$ increases the accuracy of frequency estimates. This is achieved at a higher computational cost and also m too close to N does not yield the covariance matrix $\hat{\mathbf{R}}_I$ similar to $\mathbf{R}_I$, which in turn results in spurious frequency estimates. Performing eigenvalue decomposition of $\hat{\mathbf{R}}_I$ gives estimates for eigenvectors $\mathbf{G}$ and $\mathbf{S}$, represented as $\hat{\mathbf{G}}$ and $\hat{\mathbf{S}}$, respectively. Finally using Eq. (4.6) the frequencies or the phase step values are estimated pixel-wise.

Figures (4.1a)-(4.1b) shows the plot for the case when data frame $N = 10$, and $m = 7$ and $m = 9$, respectively. As expected, the phase step α at any arbitrary pixel location on the data frame cannot be estimated correctly from the plots. Figure (4.1b) shows that value of m too close to N does not yield result. In the second case the number of data frame $N = 14$ is selected. Figure (4.1c)-(4.1e) show typical plot for phase step α with $m = 7, 9$ and 12, respectively. From Figs. (4.1c)-(4.1e), it can be observed that $m = 9$ yield better results as compared to those obtained with $m = 7$ or 12. In the third case $N = 18$ is selected, and plot for $m = 12$ is shown in Fig. (4.1f). From the plot it can be observed that phase step α can be more reliably estimated than that from Fig. (4.1d) at lower SNR's. From these three cases, it can be concluded that phase step α can be reliably estimated even at lower SNR's with increase in data frames N, and for m not too close to f and N (as a thumb rule, midway between f and N).

A better estimate for the values of frequencies can be observed if the sample covariance matrix is modified by using the following expression [120]

$$\hat{\mathbf{R}}_I = \frac{1}{2N}\sum_{n=m}^{N}\left\{\begin{bmatrix} I^*(n-1) \\ I^*(n-2) \\ \cdot \\ \cdot \\ I^*(n-m)\end{bmatrix}\begin{bmatrix} I(n-1) & I(n-2) & \cdot & \cdot & I(n-m)\end{bmatrix} + \begin{bmatrix} I^*(n-m) \\ \cdot \\ \cdot \\ I^*(n-2) \\ I^*(n-1)\end{bmatrix}\begin{bmatrix} I(n-m) & \cdot & \cdot & I(n-2) & I(n-1)\end{bmatrix}\right\} \tag{4.8}$$

The approach which obtains the frequency estimates from the formulation of covariance matrix given in Eq. (4.8) is called the *forward-backward approach.* Figures (4.2a)-(4.2b) shows the plot for the case when data frame $N = 10$, and $m = 7$ and $m = 9$, respectively. As expected, the phase step α at any arbitrary pixel location on the data frame cannot be estimated at lower SNRs (below 25 dB) from this plot. Figure (4.2b) shows that value of m too close to N does not yield result. In the second case the number of data frame $N = 14$ is selected. Figures (4.2c)-(4.2e) show typical plot for phase step α with $m = 7, 9$ and 12, respectively. From Figs. (4.2c)-(4.2e), it can be observed that $m = 9$ yield better results as compared to those obtained with $m = 7$ or 12. In the third case $N = 18$ is selected, and plot for $m = 12$ is shown in Fig. (4.2f). From

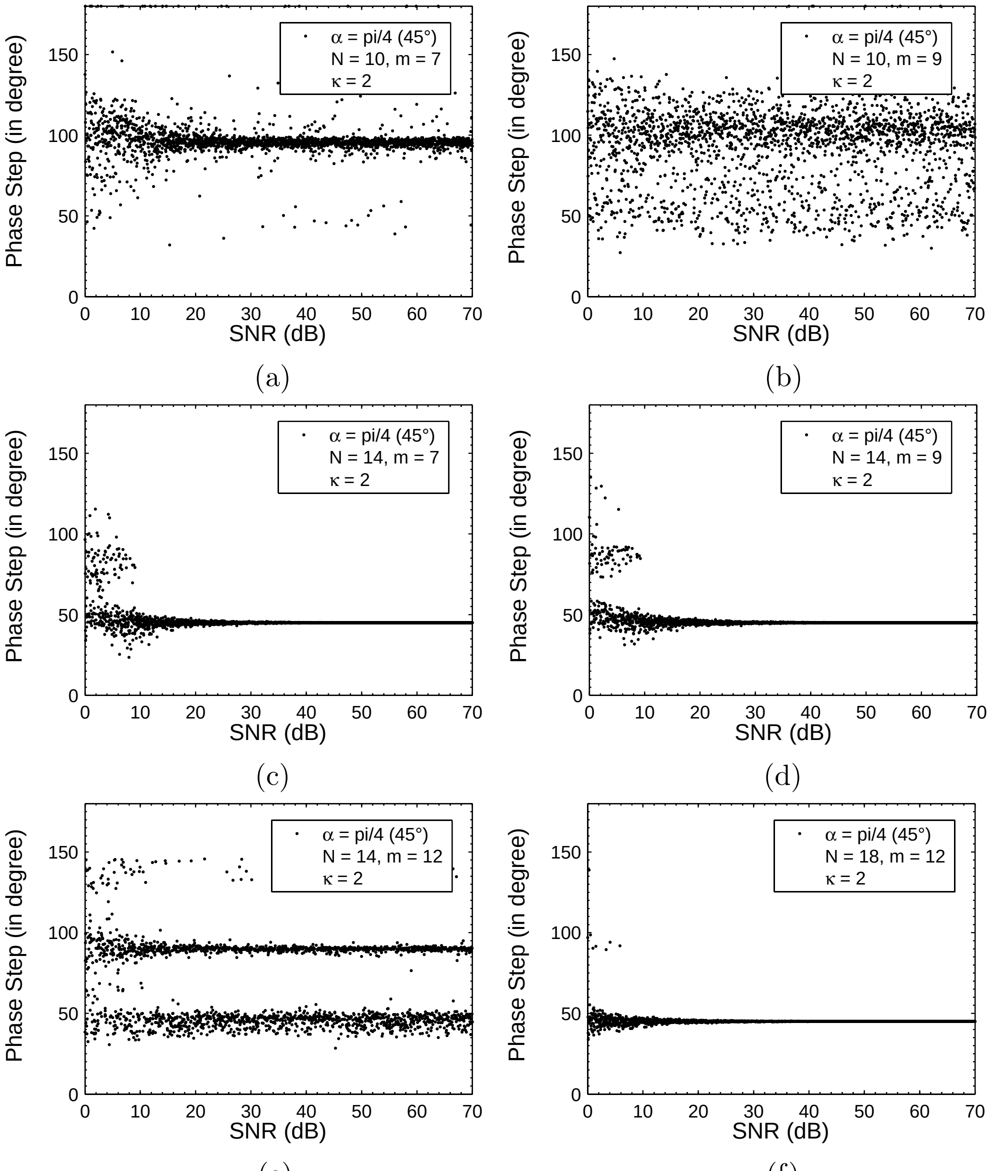

(a) (b) (c) (d) (e) (f)

Fig. 4.1: Plot of phase step α (in degree) versus SNR at an arbitrary pixel location on a data frame for $\kappa = 2$ and for different values of N and m in Eq. (4.7) using *forward approach.*

the plot it can be observed that phase step α can be more reliably estimated than that from Fig. (4.2d) at lower SNR's. From these three cases, it can be concluded that phase step α can be reliably estimated even at lower SNR's with increase in data frames N, and for m not too close to f and N (as a thumb rule, midway between f and N).

4.4 Evaluation of the MUSIC Technique for Holographic Moiré

The concept of MUltiple SIgnal Classification technique presented in section 4.2 is extended further to retrieve phases in the two arms of a holographic moiré [121]. First step consists of forming the covariance matrix from N recorded phase shifted sequences corresponding to

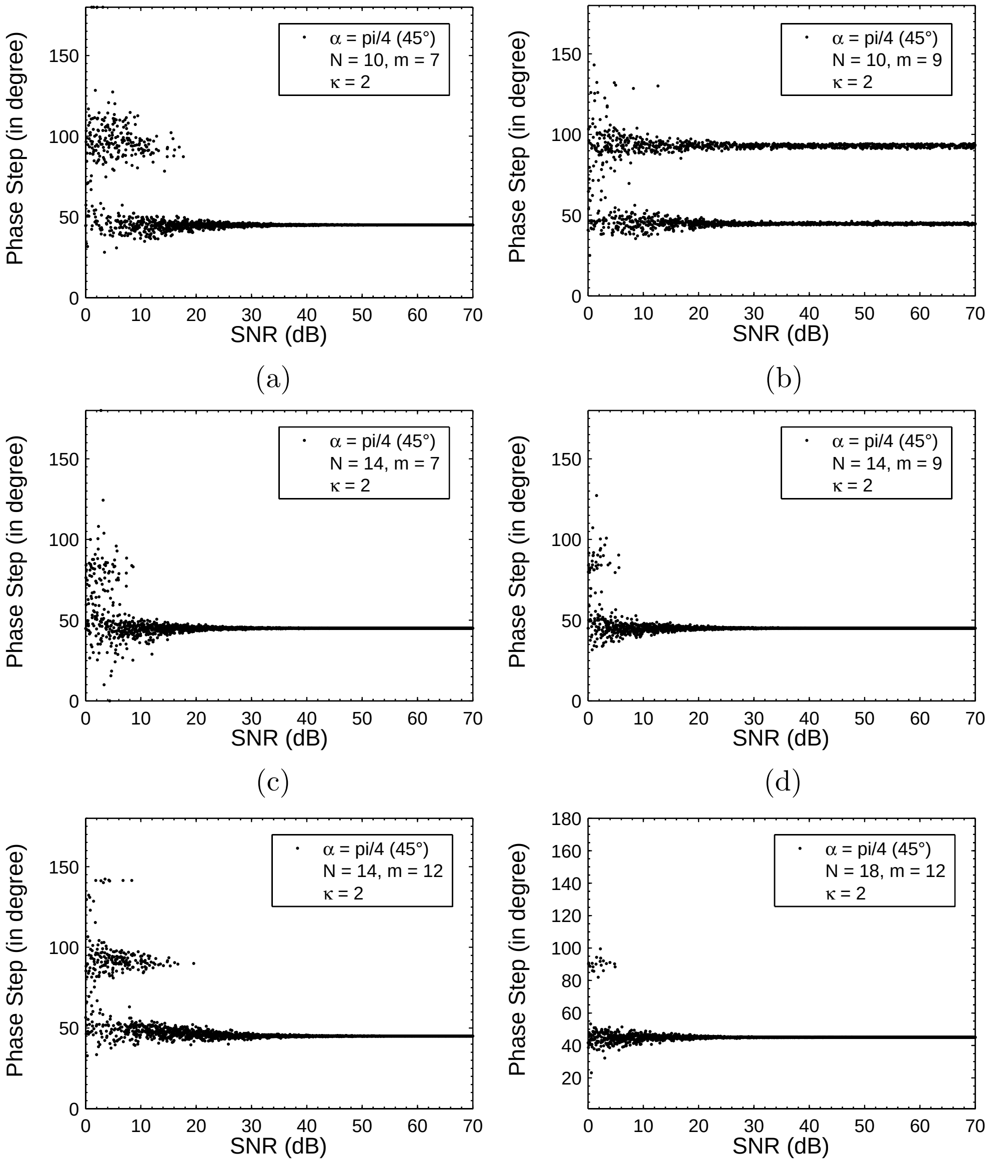

(a) (b) (c) (d) (e) (f)

Fig. 4.2: Plot of phase step α (in degree) versus SNR at an arbitrary pixel location on a data frame for $\kappa = 2$ and for different values of N and m in Eq. (4.8) using *forward-backward approach.*

holographic moiré . The covariance of signal $I(n)$ in Eq. (2.19) is defined as

$$r(p) = E[I(n)I^*(n-p)] = \sum_{k=0}^{4\kappa} A_k^2 exp(j\omega_k p) + \sigma^2 \delta_{p,0} \tag{4.9}$$

The terms A_0^2, A_1^2,....,$A_{4\kappa}^2$ can be derived in the similar way as explained in Appendix A. The Vandermonde matrix in Eq. (4.3) for holographic moiré is $\mathbf{A}_{m\times 4\kappa+1} = [\mathbf{a}(\omega_0) \ \cdots \ \mathbf{a}(\omega_{4\kappa})]$ and

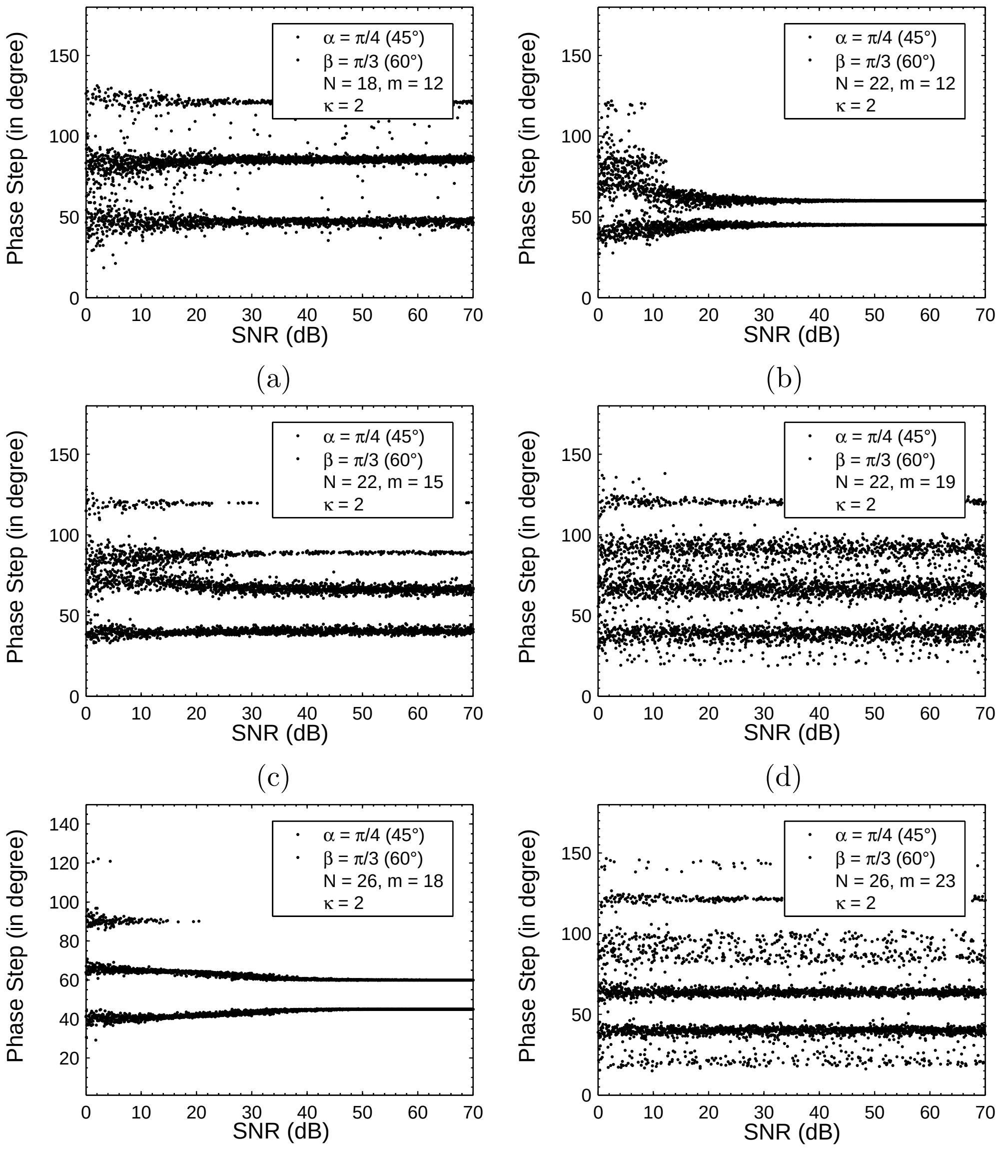

(a) (b) (c) (d) (e) (f)

Fig. 4.3: Plot of phase step α and β (in degree) versus SNR at an arbitrary pixel location on a data frame for $\kappa = 2$ and for different values of N and m in Eq. (4.7) using *forward approach.*

$\mathbf{P}_{(4\kappa+1)\times(4\kappa+1)}$ matrix is

$$\mathbf{P} = \begin{bmatrix} A_0^2 & 0 & \cdot & \cdot & 0 \\ 0 & A_1^2 & \cdot & \cdot & \cdot \\ \cdot & \cdot & \cdot & \cdot & \cdot \\ 0 & \cdot & \cdot & \cdot & A_{4\kappa}^2 \end{bmatrix} \tag{4.10}$$

The phase steps α and β can finally be estimated from Eq. (4.6). Once, the phase steps are estimated, linear Vandermonde system of equation in Eq. (2.31) is applied for the estimation of φ_1 and φ_2. During the simulation, in Eq. (2.19), the phase steps are selected as $\alpha = \pi/4$ and $\beta = \pi/3$, and harmonics $\kappa = 2$. The minimum number of data frames required for estimating

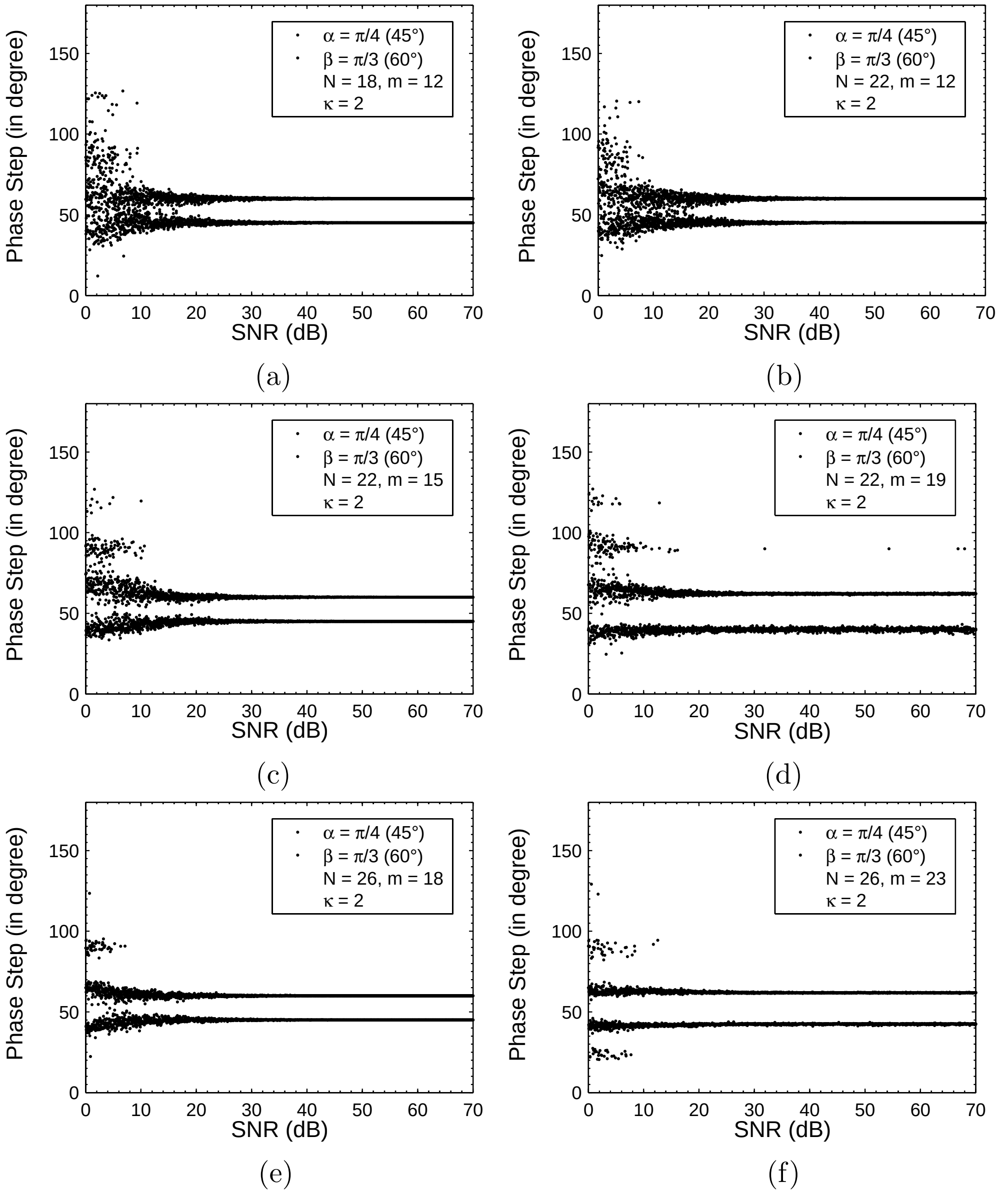

(a) (b)

(c) (d)

(e) (f)

Fig. 4.4: Plot of phase step α and β (in degree) versus SNR at an arbitrary pixel location on a data frame for $\kappa = 2$ and for different values of N and m in Eq. (4.8) using *forward-backward approach.*

the phase is $N = 18$, since $f = 9$, in the present example.

In the first case, let us evaluate the phase steps using the *forward approach* using Eq. (4.7). Figure (4.3a) shows the first case for the number of data frames $N = 18$ and value of $m = 12$. The phase steps α and β at any arbitrary pixel location on the data frame cannot be estimated from this plot. In the second case the number of data frames is chosen as $N = 22$. Figures (4.3b)-(4.3d) show typical plots for phase steps α and β with $m = 12$, 15, and 19 respectively. Figure (4.3b) shows that phase steps can be estimated for the values of SNR = 40 dB and above. However, no information regarding phase steps can be obtained from Figs. (4.3c)-(4.3d). In the third case, we choose $N = 26$, and plots for $m = 18$ and 23 are shown in Figs. (4.3e)-(4.3f), respectively.

From the plots it can be seen that phase steps can be estimated reliably for values of SNR = 40 dB and above in Fig. (4.3e). Figure (4.3f) shows that the value of m close to N does not yield reliable phase steps estimates.

In the second case, let us estimate the phase steps using the *forward-backward approach* given by Eq. (4.8). Figure (4.4a) shows the case for $N = 18$ and $m = 12$. The phase steps can be estimated in this case in contrary to the *forward* approach. In the second case the number of data frames is increased to $N = 22$. Figures (4.4b)-(4.4d) show typical plots for phase steps α and β for $m = 12$, 15, and 19 respectively. Figure (4.4c) yields better result at lower SNRs (25dB) as compared to that obtained in Figs. (4.4b) and (4.4d). From Fig. (4.4d), one can observe that value of m close to N does not yield reliable estimate. The phase steps can be more accurately measured for lower SNRs if the number of data frames are increased. For instance, in the third case we choose $N = 26$, and plots for $m = 18$ and 23 are shown in Figs. 4.4e) and (4.4f), respectively. From these plots we see that phase steps α and β can be better estimated from Fig. (4.4e) than that from Fig. (4.4f). We also observe that values of m too close to N do not reliably yield the phase step estimates. From the three cases discussed above we conclude that phase steps α and β can be reliably estimated at lower SNRs with an increase in the number of data frames N with m not too close to N. Finally, the Vandermonde system of equations in Eq. (2.31) is applied for the estimation of φ_1 and φ_2. The statistical study on the error in the estimation of phase values φ_1 and φ_2 will be presented in Chapter 9.

4.5 Discussion

To conclude, we have proposed a new approach for recovering phase distributions in the presence of higher order harmonics and multiple PZTs. The method offers the flexibility to select arbitrary phase steps and facilitates the use of spherical beams in optical interferometers. The proposed method allows for determining the phase steps of PZTs. Simulated results demonstrate the effectiveness of the proposed method for the case of holographic moiré . Further study should focus on determining the statistical accuracy of the method to resolve two closely spaced phase steps in the presence of white Gaussian noise.

Chapter 5

Minimum-Norm Algorithm for Phase Shifting Interferometry

The minimum-norm (min-norm) algorithm has been used extensively in the frequency estimation of sinusoids buried in white noise. Although, both the min-norm and the MUSIC derive the frequency estimates from the *noise subspace*, the former offers substantial computational advantage with almost the same statistical accuracy. This chapter thus presents a min-norm algorithm to estimate the phase steps from the *noise subspace.* Once the phases steps are estimated pixelwise, the phase information can be derived as in chapter 2.

5.1 Introduction of Min-norm algorithm

The min-norm algorithm has been used extensively in frequency estimation of sinusoidals buried in white noise. The algorithm functions by designing an autocovariance matrix given by Eq. (4.2). Usually, an autocovariance matrix is formulated from small overlapping fragments of the data sets using sliding window technique known as spatial smoothing presented in section 4.3. Subsequently, an autocovariance matrix is eigendecomposed to yield the *signal- and noise subspaces.* The derivation [116, 117] in this section also shows that the signal and noise spaces are orthogonal to each other. Therefore, the phase step values imparted to the PZT can be estimated pixel-wise from the *noise subspace.*

Let us recall Eq. (4.5) presented in the previous chapter

$$\mathbf{R}_I\mathbf{G} = \mathbf{G}\begin{bmatrix} \lambda_{f+1} & 0 & \cdot & \cdot & 0 \\ 0 & \lambda_{f+2} & \cdot & \cdot & \cdot \\ \cdot & \cdot & \cdot & \cdot & \cdot \\ 0 & \cdot & \cdot & \cdot & \lambda_m \end{bmatrix} = \sigma^2\mathbf{G} = \mathbf{APA}^c\mathbf{G} + \sigma^2\mathbf{G} \tag{5.1}$$

The equality in Eq. (5.1) means that $\mathbf{APA}^c\mathbf{G} = 0$ and since $\mathbf{AP}$ has full column rank we have

$$\mathbf{A}^c\mathbf{G} = 0 \tag{5.2}$$

This means that sinusoidals $\{\mathbf{a}(\omega_k)\}_{k=0}^{f}$ are orthogonal to *noise subspace.* This also indicates that $\{\mathbf{g}_k\}_{k=1}^{m-f}$ of $\mathbf{G}$ belong to the null space of $\mathbf{A}^c$ (can be written as $\mathbf{g}_k \in \mathbb{N}(\mathbf{A}^c)$). The dimension of $\mathbb{N}(\mathbf{A}^c)$ is equal to $m - f$ which is also the dimension of *range space* of $\mathbf{G}$, written as $\mathbb{R}(\mathbf{G})$. This fact combined to the observation that $\mathbf{A}^c\mathbf{G} = 0$ leads us to

$$\mathbb{R}(\mathbf{G}) = \mathbb{N}(\mathbf{A}^c) \tag{5.3}$$

Since, by definition

$$\mathbf{S}^c\mathbf{G} = 0 \tag{5.4}$$

and $\mathbb{R}(\mathbf{G}) = \mathbb{N}(\mathbf{S}^c)$; we have, $\mathbb{N}(\mathbf{S}^c) = \mathbb{N}(\mathbf{A}^c)$. We further deduce that since $\mathbb{R}\mathbf{S}$ and $\mathbb{R}\mathbf{A}$ are orthogonal complements to $\mathbb{N}(\mathbf{S}^c)$ and $\mathbb{N}(\mathbf{A}^c)$, respectively, it follows that

$$\mathbb{R}(\mathbf{S}) = \mathbb{R}(\mathbf{A}) \tag{5.5}$$

Observing Eqs. (5.4) and (5.5); the subspaces $\mathbb{R}(\mathbf{S})$ and $\mathbb{R}(\mathbf{G})$ are called *signal subspace* and *noise subspace*, respectively. In practice, since only the estimate $\hat{\mathbf{R}}_I$ of $\mathbf{R}_I$ is available, only the estimate $\hat{\mathbf{G}}$ of $\mathbf{G}$ can be determined. MUSIC uses $m - f$ linearly independent vectors in $\hat{\mathbf{G}}$ to obtain the frequency estimates. Using Eq. (5.2), in *root* MUSIC, the frequencies are estimated as angular positions of roots of equation

$$\mathbf{a}^T(z^{-1})\hat{\mathbf{G}}\hat{\mathbf{G}}^c\mathbf{a}(z) = 0 \tag{5.6}$$

In Eq. (5.6), $\mathbf{a}(z)$ is obtained from $\mathbf{a}(\omega)$, and by replacing $\exp(j\omega)$ by z we get $\mathbf{a}(z) = [1\ z^{-1} \cdot \cdot z^{-(m-1)}]^T$.

From Eq. (5.6), one can also see that since any vector in $\mathbb{R}(\hat{\mathbf{G}})$ is orthogonal to $\{\mathbf{a}(\omega_k)\}_{k=0}^{f}$, therefore, without sacrificing the accuracy too much, only one such vector can be used. This would result in substantial computational savings. The statistical accuracy of the min-norm algorithm is similar to that obtained using MUSIC. Hence, the performance of MUSIC algorithm is achieved at reduced computational cost [122, 123]. Min-norm algorithm computes the frequencies as the angular positions of the roots of the polynomial

$$\mathbf{a}^T(z^{-1})\begin{bmatrix} 1 \\ \hat{\mathbf{g}} \end{bmatrix} = 0 \tag{5.7}$$

where, $[1\,\hat{\mathbf{g}}]^T$ is the vector in $\mathbb{R}(\hat{\mathbf{G}})$ with first element equal to unity, that has minimum Euclidean norm. The following explains the rational behind this specific selection [122].

Let the Euclidean norm of a vector be denoted by $\|\cdot\|$. Since, in reality only the estimate $\hat{\mathbf{R}}_I$ of $\mathbf{R}_I$ is available, only the estimate $\hat{\mathbf{S}}$ of $\mathbf{S}$ can be determined. Let the matrix $\hat{\mathbf{S}}$ be partitioned as

$$\hat{\mathbf{S}} = \begin{bmatrix} \chi^c \\ \bar{\mathbf{S}} \end{bmatrix} \begin{matrix} \}1 \\ \}m-1 \end{matrix} \tag{5.8}$$

As, $[1\ \ \hat{\mathbf{g}}]^T \in \mathbb{R}(\hat{\mathbf{G}})$, Eq. (5.4) can be written as

$$\hat{\mathbf{S}}^c\begin{bmatrix} 1 \\ \hat{\mathbf{g}} \end{bmatrix} = 0 \tag{5.9}$$

Equation (5.9) can be rewritten using Eq. (5.8) as

$$\bar{\mathbf{S}}^c\hat{\mathbf{g}} = -\chi \tag{5.10}$$

The minimum-norm solution to Eq. (5.10) is given by

$$\hat{\mathbf{g}} = -\bar{\mathbf{S}}(\bar{\mathbf{S}}^c\bar{\mathbf{S}}^c)^{-1}\chi \tag{5.11}$$

under the assumption that the inverse exists. Given that the identity matrix $\mathbf{I}$ can be written as

$$\mathbf{I} = \hat{\mathbf{S}}^c\hat{\mathbf{S}} = \chi\chi^c + \bar{\mathbf{S}}^c\bar{\mathbf{S}} \tag{5.12}$$

and that one eigenvalue of $\mathbf{I} - \chi\chi^c$ is equal to $1- \parallel \chi \parallel^c$ and the remaining $f-1$ eigenvalues of $\mathbf{I} - \chi\chi^c$ are equal to unity, the inverse in Eq. (5.11) exists if and only if

$$\parallel \chi \parallel^c \neq 1 \tag{5.13}$$

If Eq. (5.13) is not satisfied, there will be no vector of the form of $[1 \quad \hat{\mathbf{g}}]^T$ in $\mathbb{R}(\hat{\mathbf{G}})$. Condition in Eq. (5.13) is equivalent to $\text{rank}(\bar{\mathbf{S}}^c\bar{\mathbf{S}}) = f$ which, in turn, holds if and only if

$$\text{rank}(\bar{\mathbf{S}}) = f \tag{5.14}$$

From Eq. (5.5) it can be observed that any block of matrix $\mathbf{S}$ made from more than f consecutive rows should have rank equal to f. Therefore, Eq. (5.14) is valid as long as N is sufficiently large. This completes the derivation of min-norm frequency estimator defined in Eq. (5.7). In addition, it has been shown that by using the min-norm vector $\mathbb{R}(\hat{\mathbf{G}})$ as defined in Eq. (5.7), the spurious frequency estimates can be reduced, a problem sometimes associated with the MUSIC method. Next sections discuss the evaluation of min-norm algorithm for the estimation of phase step.

5.2 Evaluation of the Minimum-Norm Algorithm

This section presents simulation results obtained using min-norm algorithm to extract the phase step values pixel-wise [124]. The phase φ for the interference fringes are simulated using the same equation as defined in Eq. (1.5a) for phase φ_1. In Eq. (2.1); we assume $\kappa = 2$, $\alpha = pi/4$, $a_{\pm1,\pm2} = 0.5$, and $I_{dc} = 1$. Additive white Gaussian noise with SNR between 0 and 70 dB is added to Eq. (2.1) and for each noise level phase step is computed at every pixel of the data frame. Let us first study the estimation of phase step using *forward approach.* Figures (5.1a)-(5.1d) show the case for $m = 6$, 7, 8, and 9, respectively in Eq. (4.2) when number of data frames $N = 10$ is used in computation of phase steps. The plot in Fig. (5.1a) shows that the phase step value can be reliably estimated from 70 dB onwards, while, the plot in Figs. (5.1b)-(5.1d) shows that the phase step values cannot be estimated at all since the value of m is too close to N. From Fig. (5.1b)-(5.1d) it can be inferred that estimation of phase step values at lower SNR's does not yield reliable results as the value of m approaches closer to N. Furthermore, plot in Fig. (5.1e) shows improved phase step estimation at lower SNR's with increased data frames ($N = 12$). Figure (5.1e) yields better phase step estimate as compared to that obtained from the plot in Fig. (5.1a). From this study it can again be concluded that phase step α can be reliably estimated at low SNR's with increase in number of data frames and for values of m not too close to f and N.

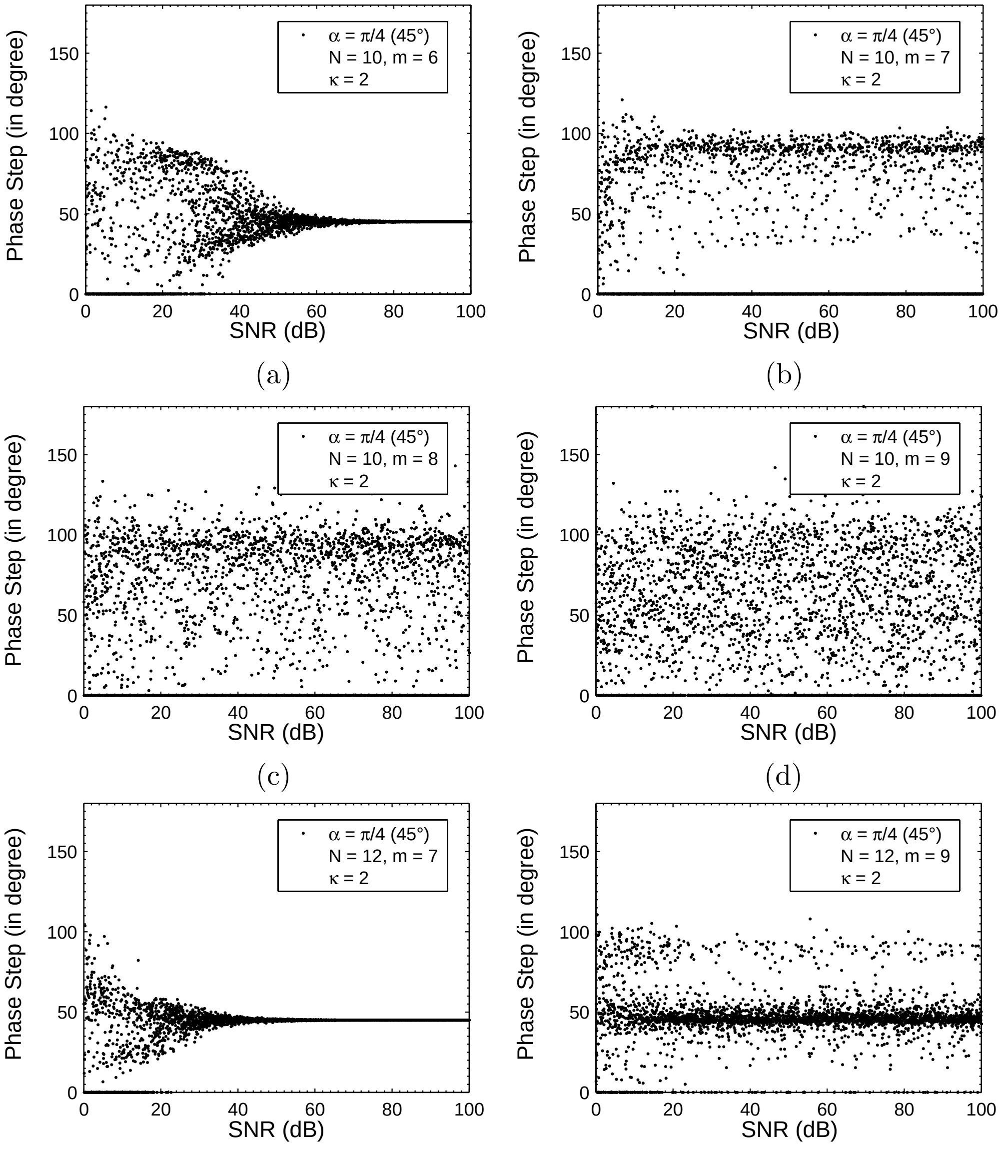

(a) (b)

(c) (d)

(e) (f)

Fig. 5.1: Plot of phase step α (in degree) versus SNR at an arbitrary pixel location on a data frame for $\kappa = 2$ and for different values of N and m in Eq. (4.7) using *forward approach.*

The phase step can be estimated reliably at low SNRs if the *forward-backward approach* is used. Figures (5.2a)-(5.2d) show the case for $m = 6$, 7, 8, and 9, respectively in Eq. (4.8) when number of data frames $N = 10$ is used in computation of phase steps. The plot in Fig. (5.2a) shows that the phase step value can be reliably estimated from 45 dB onwards, while, the plot in Fig. (5.2d) shows that the phase step values cannot be estimated at all since the value of m is too close to N. Figure (5.2b) shows that phase step values can be estimated at lower SNR's than that obtained from Fig. (5.2a), since the value of m is approximately midway between f and N. From Fig. (5.2c) it can be inferred that estimation of phase step values at lower SNR's does not yield reliable results as the value of m approaches closer to N. Furthermore, plot in Fig. (5.2e) shows improved phase step estimation at lower SNR's with increased data frames ($N = 12$). Figure (5.2f) yields better phase step estimate as compared to that obtained from the plot in

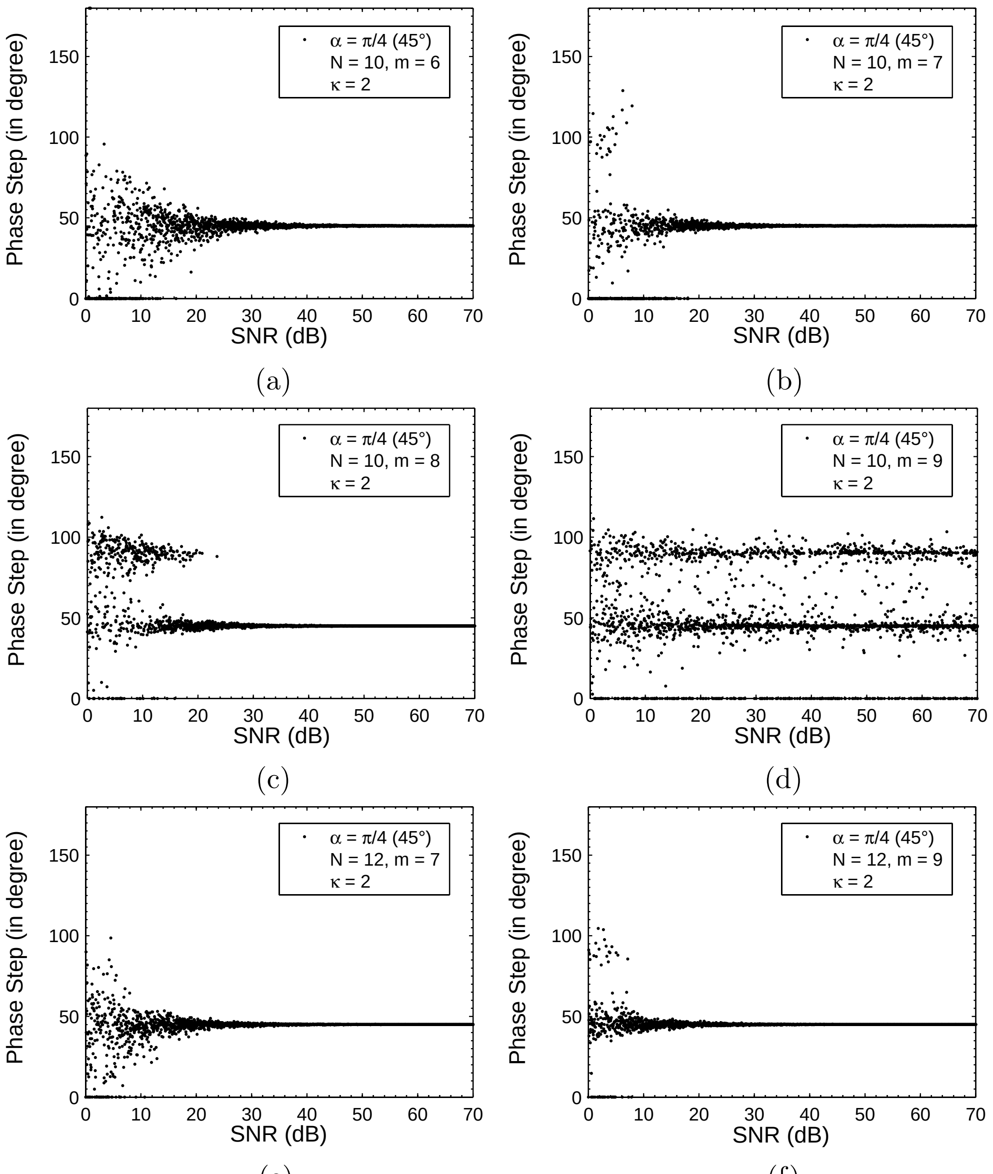

(a) (b) (c) (d) (e) (f)

Fig. 5.2: Plot of phase step α (in degree) versus SNR at an arbitrary pixel location on a data frame for $\kappa = 2$ and for different values of N and m in Eq. (4.8) using *forward-backward approach.*

Fig. (5.2e). From this study it can be concluded that phase step α can be reliably estimated at low SNR's with increase in number of data frames and for values of m not too close to f and N.

5.3 Evaluation of the Minimum-Norm Algorithm for Holographic Moiré

The concept of min-norm algorithm is extended further to retrieve phases in the two arms of a holographic moiré [125]. During the simulation, in Eq. (2.19), the phase steps are selected as $\alpha = \pi/4$ and $\beta = 7\pi/18$, and harmonics $\kappa = 2$. The minimum number of data frames required for estimating the phase is $N = 18$, since $f = 9$, in the present example. In the first case, let us

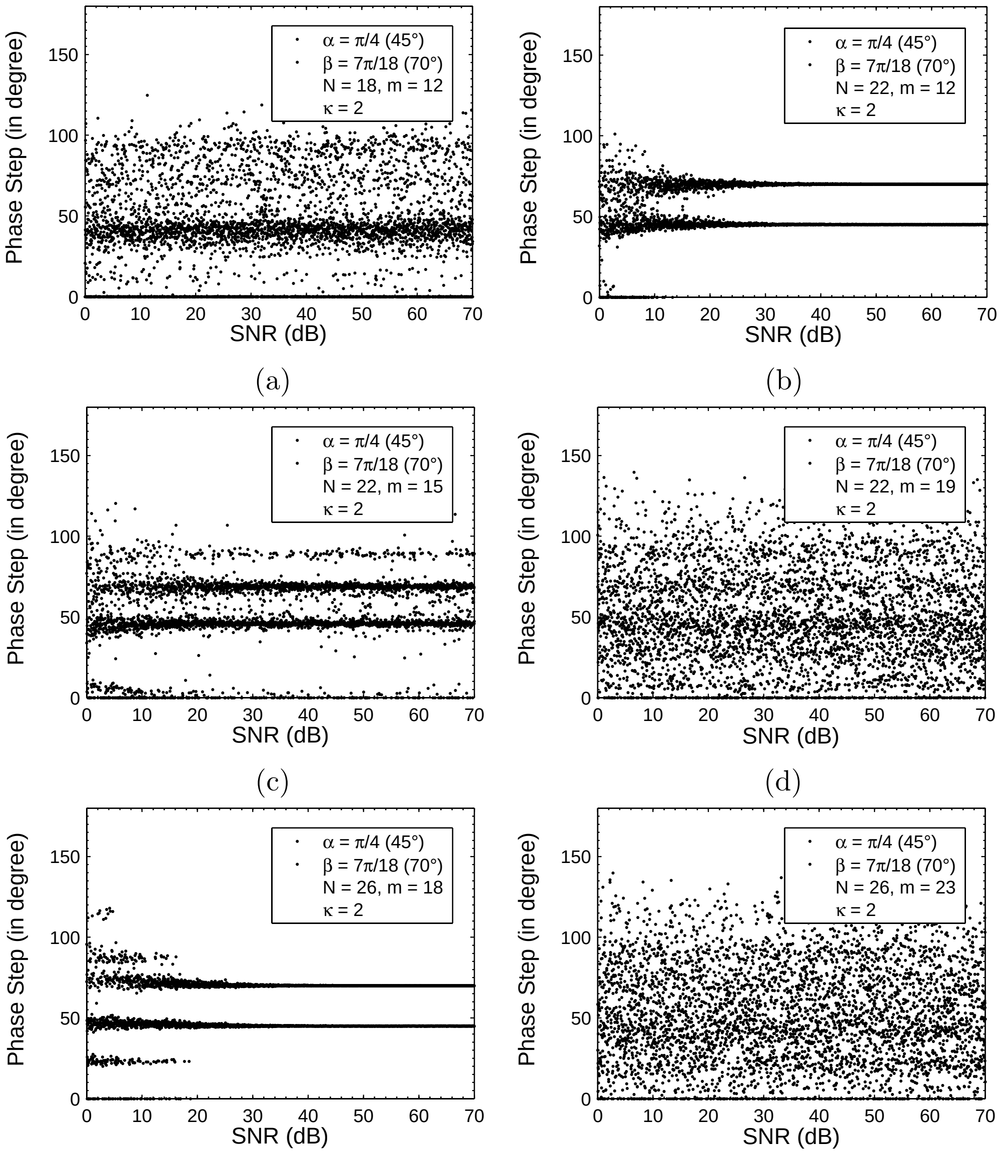

(a) (b)

(c) (d)

(e) (f)

Fig. 5.3: Plot of phase step α and β (in degree) versus SNR at an arbitrary pixel location on a data frame for $\kappa = 2$ and for different values of N and m in Eq. (4.7) using *forward approach.*

study the estimation of phase steps using the *forward approach.* Figure (5.3a) shows the plot for a case in which the number of data frames $N = 18$ and $m = 12$ is selected. The phase step values α and β at any arbitrary pixel location on the data frame cannot be estimated from this plot. In the second case, we choose the number of data frames to be $N = 22$. Figures (5.3a)-(5.3d) show typical plots for phase steps α and β for $m = 12$, 15, and 19, respectively. From these plots it can be observed that even if the number of frames is increased the phase steps can be estimated only when appropriate value for m is selected. Figure (5.3b) shows that phase steps α and β can be estimated reliably from 35 dB onwards. In the third case we choose $N = 26$, and plots for phase steps are shown in Figs. (5.3e) and (5.3f), respectively. Figure (5.3e) shows that phase steps can be estimated reliably for values of SNR 35 dB and above. This shows that

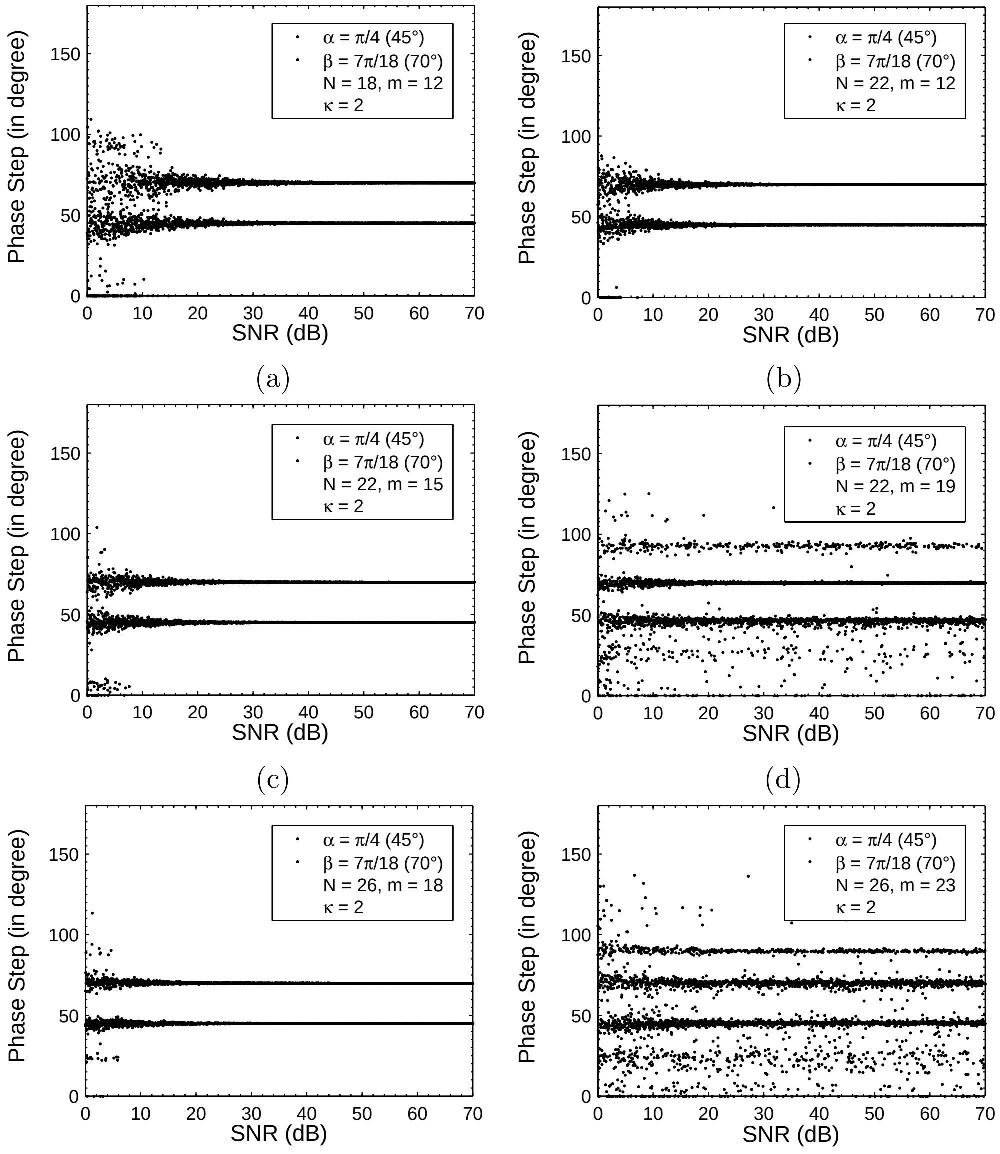

(a) (b)

(c) (d)

(e) (f)

Fig. 5.4: Plot of phase step α and β (in degree) versus SNR at an arbitrary pixel location on a data frame for $\kappa = 2$ and for different values of N and m in Eq. (4.8) using *forward-backward approach.*

with small increase in data frames, a substantial improvement in estimating the phase steps is not obtained.

In the second case, let us study the estimation of phase steps using the *forward-backward approach*. Figure (5.4a) shows the plot for data frames $N = 18$ and $m = 12$. Phase step values α and β can be estimated from this plot for values of SNR of 40dB and above. In the second case, we choose the number of data frames to be $N = 22$. Figures (5.4b)-(5.4d) show typical plots for phase steps α and β with $m = 12$, 15, and 19 respectively. Figures (5.4b)-(5.4c) shows that the values of α and β and can be estimated at much lower SNR (25 dB and above). Figure (5.4d) shows that value of m is critical and its value too close to N does not yield result.

In the third case, we choose $N = 26$; and corresponding plots for phase steps α and β are shown in Figs. (5.4e) and (5.4f), respectively. From these plots, we observe that phase steps α and β can be reliably estimated from Fig. (5.4e) as compared to Fig. (5.4f). We also observe from Fig. (5.4e) that phase steps can be estimated at much lower SNR (20dB and above) as compared to that obtained using other plots. The study shows that *forward-backward approach* yields better result than *forward approach.* Finally, the Vandermonde system of equations in Eq. (2.31) is applied for the estimation of φ_1 and φ_2. The statistical study on the error in the estimation of phase values φ_1 and φ_2 will be presented in Chapter 9.

5.4 Discussion

This chapter proposed a novel approach for recovering phase distribution in an optical setup. The successful extraction of dual phase distributions from a simulated holographic moiré pattern shows the feasibility of our proposed concept. A significant advantage of the proposed algorithm lies in its ability to measure phase steps in the presence of noise. The algorithm enables to choose arbitrarily phase shifts between 0 and π radian. The proposed technique works well with both the diverging and converging beams since it relies on retrieving the phase step values pixel-wise before applying them to the Vandermonde system of equation. The accuracy in the measurement of the phase steps in the presence of additive white Gaussian noise has been shown to increase with increasing number of data frames. The min-norm algorithm yields phase step estimates by using a single vector from the noise subspace as compared to the MUSIC method which uses the whole set of noise subspace for the phase step estimation. Hence, a reduced computational cost is achieved. However, it is interesting to study the estimation of phase steps from the *signal subspace* rather than the *noise subspace.*

Chapter 6

Rotational Invariance Approach in Phase Shifting Interferometry

In the previous two chapters, the phase step values are obtained from the *noise subspace*. With limited number of data frames being a prime requirement in phase shifting interferometry, the formation of true *noise subspace* is impossible. This chapter thus focuses on obtaining the phase step values from the *signal subspace*. For this, we exploit rotational invariance approach exhibited by the intensity data recorded at (n', j') pixel on the CCD. This approach is commonly known as Estimation of Signal Parameter via Rotational Invariance Technique (ESPRIT).

6.1 Introduction to ESPRIT

The technique functions by designing an autocovariance matrix given by Eq. (4.2). Usually, an autocovariance matrix is formulated from small overlapping fragments of the data sets using sliding window technique known as spatial smoothing presented in section 4.3. Subsequently, an autocovariance matrix is eigendecomposed to yield the *signal- and noise subspaces.* The phase step values are finally estimated pixel-wise from the *signal subspace.*

Let us recall Eq. (4.5) presented in Chapter 4 given by

$$\mathbf{R}_I\mathbf{G} = \mathbf{G}\begin{bmatrix} \lambda_{f+1} & 0 & \cdot & \cdot & 0 \\ 0 & \lambda_{f+2} & \cdot & \cdot & \cdot \\ \cdot & \cdot & \cdot & \cdot & \cdot \\ 0 & \cdot & \cdot & \cdot & \lambda_m \end{bmatrix} = \sigma^2\mathbf{G} = \mathbf{APA}^c\mathbf{G} + \sigma^2\mathbf{G} \tag{6.1}$$

The equality in Eq. (6.1) means that $\mathbf{APA}^c\mathbf{G} = 0$ and since $\mathbf{AP}$ has full column rank we have

$$\mathbf{A}^c\mathbf{G} = 0 \tag{6.2}$$

From Eq. (6.2) it can be seen that the sinusoidals $\{\mathbf{a}(\omega_k)\}_{k=0}^{f}$ are orthogonal to the *noise subspace* [123]. Let us set

$$\mathbf{\Lambda} = \begin{bmatrix} \lambda_1 - \sigma^2 & 0 & \cdot & \cdot & 0 \\ 0 & \lambda_2 - \sigma^2 & \cdot & \cdot & \cdot \\ \cdot & \cdot & \cdot & \cdot & \cdot \\ 0 & \cdot & \cdot & \cdot & \lambda_f - \sigma^2 \end{bmatrix} \tag{6.3}$$

Also observing that $\lambda_1 \geq \lambda_2 \geq \cdots \geq \lambda_f \geq \sigma^2$ and $\lambda_{f+1} = \lambda_{f+2} = \cdots = \lambda_m = \sigma^2$, and from Eq. (4.3) we get

$$\mathbf{R}_I\mathbf{S} = \mathbf{S}\begin{bmatrix} \lambda_1 & 0 & \cdot & \cdot & 0 \\ 0 & \lambda_2 & \cdot & \cdot & \cdot \\ \cdot & \cdot & \cdot & \cdot & \cdot \\ 0 & \cdot & \cdot & \cdot & \lambda_f \end{bmatrix} = \mathbf{A}\mathbf{P}\mathbf{A}^c\mathbf{S} + \sigma^2\mathbf{S}. \tag{6.4}$$

We thus obtain

$$\mathbf{S} = \mathbf{A}\underbrace{\left(\mathbf{P}\mathbf{A}^c\mathbf{S}\mathbf{\Lambda}^{-1}\right)}_{\mathbf{\Gamma}}. \tag{6.5}$$

The concept of rotational invariance [123, 126] is applied to Eq. (6.5). The basics of rotational invariance can be understood by the following illustrations.

Let us construct matrices $\mathbf{A}_{1_{(m-1)\times f}}$ and $\mathbf{A}_{2_{(m-1)\times f}}$ from $\mathbf{A}$ in Eq. (4.3) as

$$\begin{aligned} \mathbf{A}_{1_{(m-1)\times f}} &= \begin{bmatrix} \mathbf{I}_{(m-1)\times(m-1)} & \mathbf{0}_{(m-1)\times 1} \end{bmatrix}\mathbf{A}, \\ \mathbf{A}_{2_{(m-1)\times f}} &= \begin{bmatrix} \mathbf{0}_{(m-1)\times 1} & \mathbf{I}_{(m-1)\times(m-1)} \end{bmatrix}\mathbf{A}. \end{aligned} \tag{6.6}$$

where $\mathbf{I}_{(m-1)\times(m-1)}$ is an identity matrix. The matrices $\mathbf{A}_1$ and $\mathbf{A}_2$ in Eq. (6.6) are related by a unitary matrix $\mathbf{D}_{f\times f}$ in the following way:

$$\mathbf{A}_{2_{(m-1)\times f}} = \mathbf{A}_{1_{(m-1)\times f}}\underbrace{\begin{bmatrix} \exp(j\omega_1) & 0 & \cdot & \cdot & 0 \\ 0 & \exp(j\omega_2) & \cdot & \cdot & \cdot \\ \cdot & \cdot & \cdot & \cdot & \cdot \\ 0 & \cdot & \cdot & \cdot & \exp(j\omega_f) \end{bmatrix}}_{\mathbf{D}_{f\times f}}. \tag{6.7}$$

From Eq. (6.7) we observe that the transformation in Eq. (6.7) is rotation. This property plays a significant role in spectral estimation. Hence, using the same analogy as in Eq. (6.7), we can derive the matrices $\mathbf{S}_1$ and $\mathbf{S}_2$ from the $\mathbf{S}$ matrix as

$$\begin{aligned} \mathbf{S}_{1_{(m-1)\times f}} &= \begin{bmatrix} \mathbf{I}_{(m-1)\times(m-1)} & \mathbf{0}_{(m-1)\times 1} \end{bmatrix}\mathbf{S}, \\ \mathbf{S}_{2_{(m-1)\times f}} &= \begin{bmatrix} \mathbf{0}_{(m-1)\times 1} & \mathbf{I}_{(m-1)\times(m-1)} \end{bmatrix}\mathbf{S}. \end{aligned} \tag{6.8}$$

We can thus represent the matrix $\mathbf{S}_2$ using Eqs. (6.5) and (6.8) as

$$\mathbf{S}_2 = \mathbf{A}_2\mathbf{\Gamma} = \mathbf{A}_1\mathbf{D}\mathbf{\Gamma} = \mathbf{S}_1\mathbf{\Gamma}^{-1}\mathbf{D}\mathbf{\Gamma} = \mathbf{S}_1\mathbf{\Upsilon}. \tag{6.9}$$

where $\Upsilon = \Gamma^{-1}\mathbf{D}\mathbf{\Gamma}$. It is important to note that since both matrices $\mathbf{S}$ and $\mathbf{A}$ in Eq. (6.5) have full column rank, the matrix $\mathbf{\Gamma}$ is nonsingular. The matrices $\mathbf{A}_1$ and $\mathbf{A}_2$ in Eq. (6.7) have full column rank (equal to f) since the matrix $\mathbf{A}$ has Vandermonde structure. Hence, applying the similar analogy, we deduce from Eq. (6.5) that matrices $\mathbf{S}_1$ and $\mathbf{S}_2$ have full rank. Therefore, the matrix Υ is uniquely given by

$$\boldsymbol{\Upsilon} = (\mathbf{S}_1^c\mathbf{S}_1)^{-1}\mathbf{S}_1^c\mathbf{S}_2. \tag{6.10}$$

In Eq. (6.10), $\boldsymbol{\Upsilon}$ can be estimated from the available sample because $\boldsymbol{\Upsilon}$ and $\mathbf{D}$ have the same eigenvalues. Finally, ESPRIT enables us to estimate the frequencies $(\omega_k)_{k=0}^{f}$ as the argument of $\hat{\varpi}_k$, where $(\hat{\varpi}_k)_{k=0}^{f}$ are the eigenvalues of the following consistent estimate of the matrix $\boldsymbol{\Upsilon}$:

$$\hat{\boldsymbol{\Upsilon}} = (\hat{\mathbf{S}}_1^c\hat{\mathbf{S}}_1)^{-1}\hat{\mathbf{S}}_1^c\hat{\mathbf{S}}_2. \tag{6.11}$$

Since only the estimate of the covariance matrix in Eq. (4.3) can be obtained, Eq. (6.11) represents the estimated value of the matrix Υ based on the estimated values, $\hat{\mathbf{S}}_1$ and $\hat{\mathbf{S}}_2$ of $\mathbf{S}_1$ and $\mathbf{S}_2$, respectively. We infer from Eq. (6.11) that ESPRIT has no problem in separating signal roots from noise roots, a problem usually encountered in other spectral estimation techniques such as the Multiple Signal Classification (MUSIC) method [123]. The latter method has been used to estimate frequencies from the *noise subspace*, based on the precept that sinusoidals are orthogonal to *noise subspace.*

6.2 Evaluation of the ESPRIT for Phase Step Computation

This section presents simulation results obtained using ESPRIT to extract the phase step values pixel-wise [127]. The phase φ for the interference fringes are simulated using the same equation as defined in Eq. (1.5a) for phase φ_1. In Eq. (2.1); we assume $\kappa = 2$, $\alpha = pi/4$, $a_{\pm1,\pm2} = 0.5$, and $I_{dc} = 1$. Additive white Gaussian noise with SNR between 0 and 70 dB is added to Eq. (2.1) and for each noise level phase step is computed at every pixel of the data frame. We first look into the retrieval of phase step value by using the *forward approach.* Assuming that the number of frequencies are known (in the present case $f = 5$), an appropriate value of m must be selected such that $m > f$. First the matrix $\hat{\mathbf{R}}_I$ in Eq. (4.2) is eigendecomposed so as to obtain eigenvectors $\hat{\mathbf{S}}$, from which the matrices $\hat{\mathbf{S}}_1$ and $\hat{\mathbf{S}}_2$ are determined. Phase step is subsequently estimated from Eq. (6.11).

Figure (6.1a) shows the case for $m = 6$ when number of data frames is $N = 8$. The phase step α at any arbitrary pixel location on the data frame cannot be estimated from this plot for low SNR values. Figures (6.1b)-(6.1d) show typical plots for $m = 6$, 7, and 9 where we have increased the number of data frames to 10. Plots in Fig. (6.1b), show an increase in the performance in the determination of phase step. The plot in Figs. (6.1e)-(6.1f) shows the phase step for $m = 9$ and 11 for data frame $N = 14$. From the study of the above cases it can be concluded that phase step can be reliably estimated even at low SNR's with increase in number of data frames and for values of m not too close to N and f.

In the second case, the *forward-backward approach* is used for the estimation of phase step. Figure (6.2a) shows the case for $m = 6$ when number of data frames is $N = 8$. The phase step α at any arbitrary pixel location on the data frame cannot be estimated from this plot for low SNR values. Figures (6.1b)-(6.1d) show typical plots for $m = 6$, 7, and 9 where we have increased the number of data frames to 10. Plots in Figs. (6.1b)-(6.1c), show an increase in the performance in the determination of phase step at low SNR's. The plot in Fig. (6.1d) shows value of m too close to N yields spurious result. That the accuracy in the determination of phase step

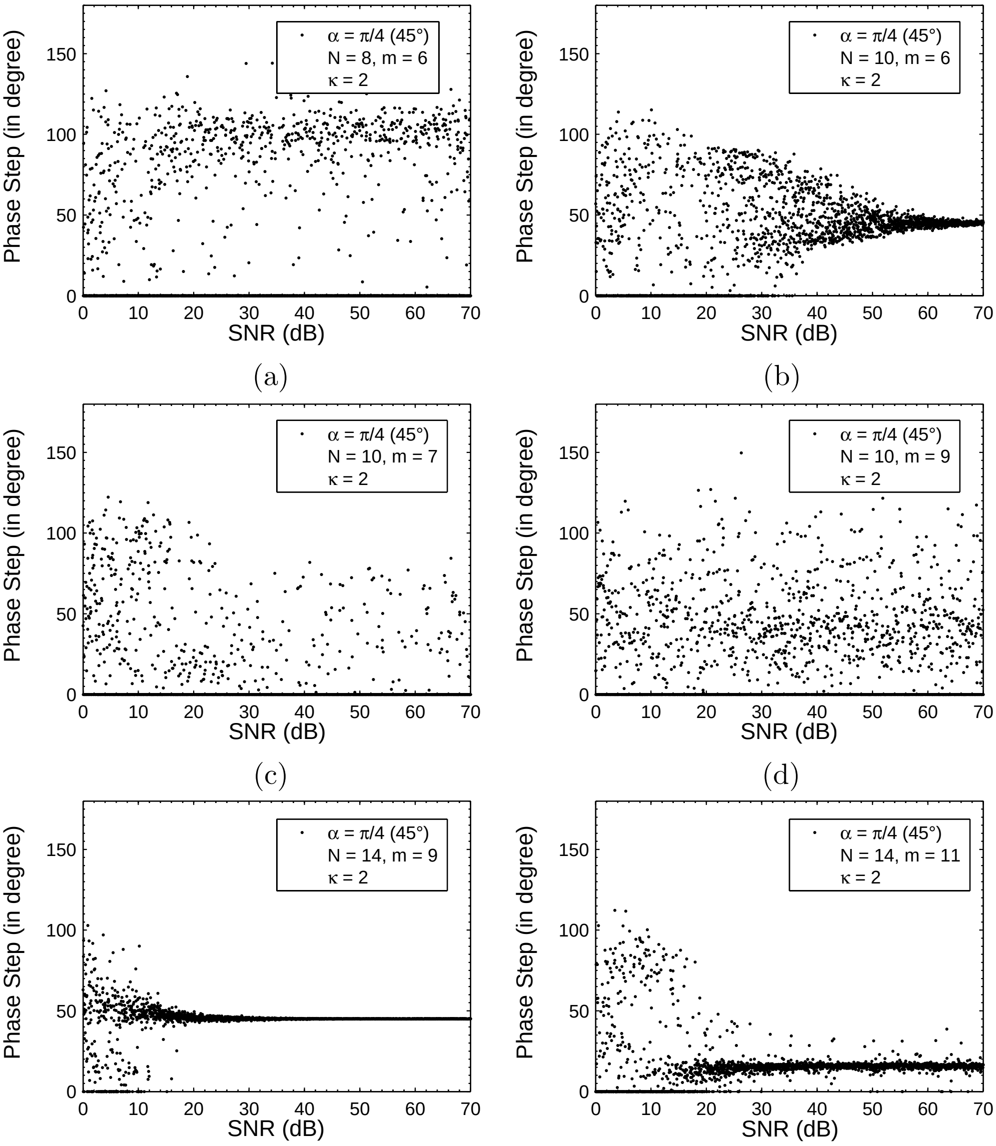

(a) (b)

(c) (d)

(e) (f)

Fig. 6.1: Plot of phase step α (in degree) versus SNR at an arbitrary pixel location on a data frame for $\kappa = 2$ and for different values of N and m in Eq. (4.7) using *forward approach*.

increases with large data frames is shown in Figs. (6.1e)-(6.1f), where $N = 14$. Figures (6.1e)-(6.1f) show typical plots for $m = 9$ and 11, respectively. From these figures, we observe that *forward-backward approach* yields better result as compared to the *forward approach*.

6.3 Evaluation of the ESPRIT for Holographic Moiré

The concept of ESPRIT is extended further to retrieve phases in the two arms of a holographic moiré [128]. During the simulation, in Eq. (2.19), the phase steps are selected as $\alpha = \pi/4$ and $\beta = \pi/3$, and harmonics $\kappa = 2$. The minimum number of data frames required for estimating the phase is $N = 18$, since $f = 9$, in the present example.

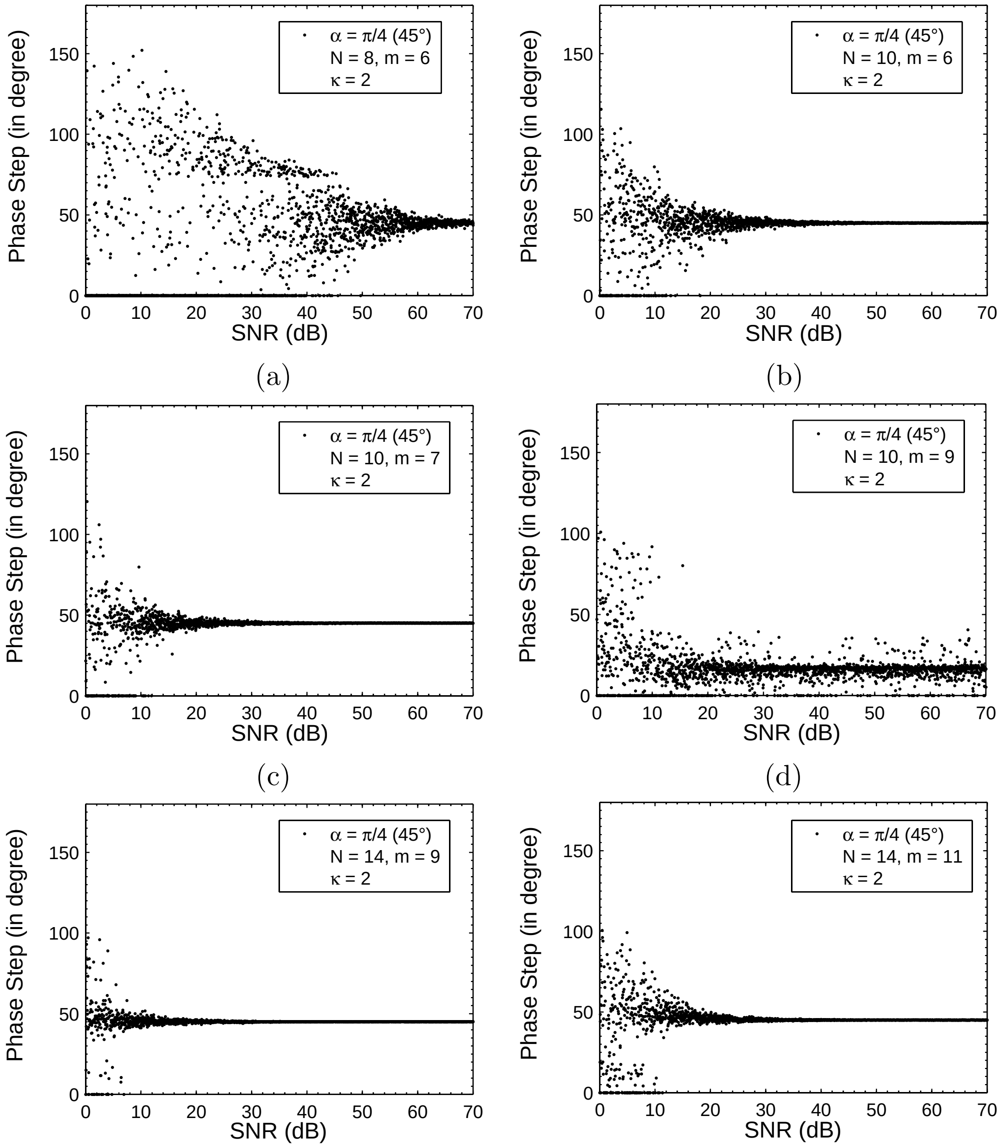

(a) (b) (c) (d) (e) (f)

Fig. 6.2: Plot of phase step α (in degree) versus SNR at an arbitrary pixel location on a data frame for $\kappa = 2$ and for different values of N and m in Eq. (4.8) using *forward-backward approach.*

Let us first study the estimation of phase steps using the *forward approach*. Figure (6.3a) shows the plot for a case in which the number of data frames $N = 10$ and $m = 10$ is selected. The phase step values α and β at any arbitrary pixel location on the data frame cannot be estimated from this plot. In the second case, we choose the number of data frames to be $N = 15$. Figures (6.3b), (6.3c), and (6.3d) show the typical plots for phase steps α and β for $m = 10$, 11, and 12 respectively. From these plots it can be observed that even if the number of frames is increased the phase steps cannot be estimated. In the third case we choose $N = 25$, and plots for are shown in Figs. (6.3e)-(6.3f), respectively. Figure (6.3e) shows that phase steps can be estimated reliably for values of SNR 25 dB and above. On the other hand, Fig. (6.3f) shows that value of m too close to N does not yield reliable phase step estimates.

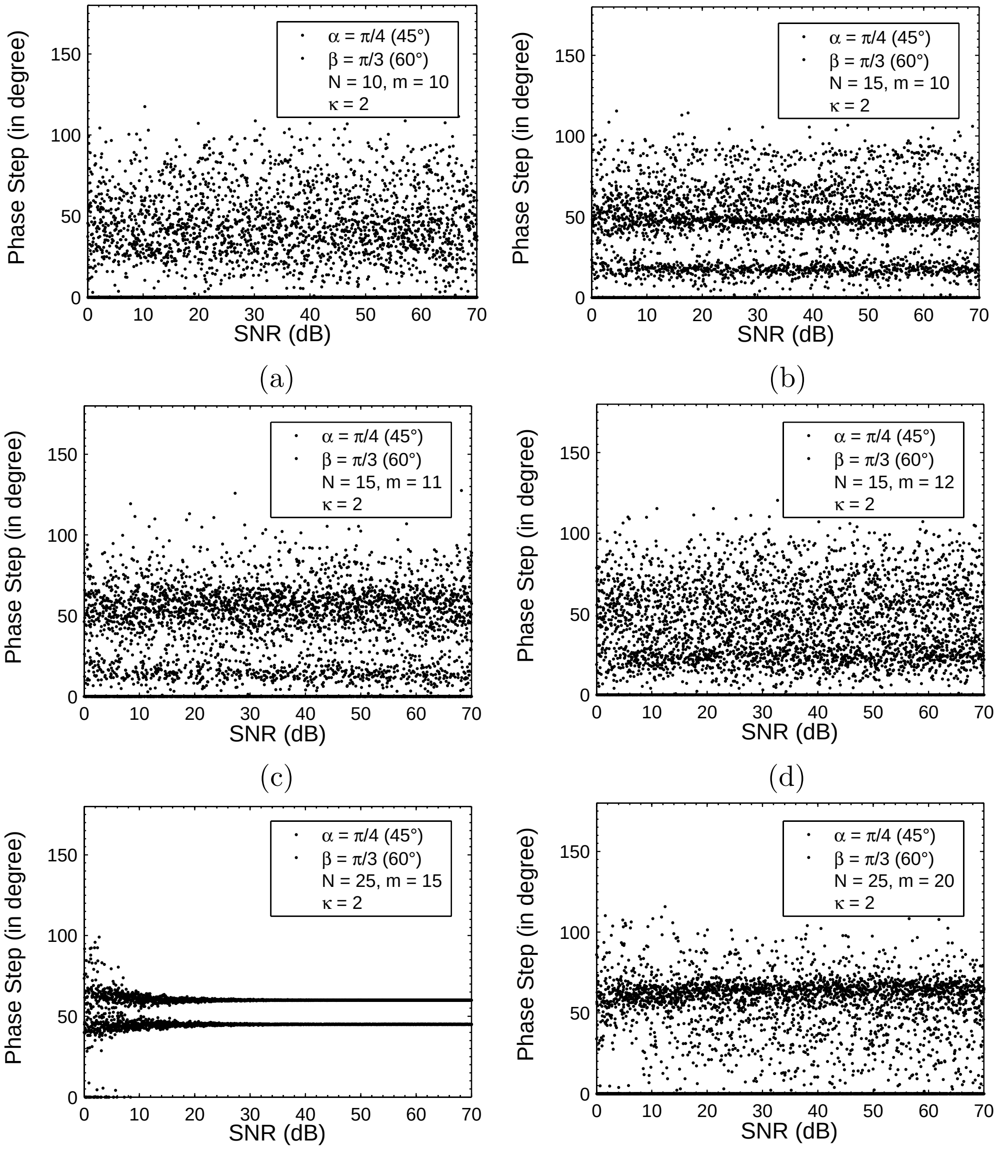

(a) (b)

(c) (d)

(e) (f)

Fig. 6.3: Plot of phase step α and β (in degree) versus SNR at an arbitrary pixel location on a data frame for $\kappa = 2$ and for different values of N and m in Eq. (4.7) using *forward approach.*

Let us now study the estimation of phase steps using the *forward-backward approach.* Figure (6.4a) shows the plot for a case in which the number of data frames $N = 10$ and $m = 10$ is selected. The phase step values α and β at any arbitrary pixel location on the data frame cannot be estimated from this plot. In the second case, we choose the number of data frames to be $N = 15$. Figures (6.4b), (6.4c), and (6.4d) show the typical plots for phase steps α and β for $m = 10$, 11, and 12 respectively. Figure (6.4c) shows that the values of α and β can be estimated at much lower SNR (35 dB and above) as compared to that obtained (SNR 60 and above) from Fig. (6.4b). Figure (6.4d) shows that value of m is critical for small number of data frames. In the third case, we choose $N = 25$; the corresponding plots for $m = 15$ and 20 are shown in Figs. (6.4e) and (6.4f), respectively. From these three cases we can conclude that phase steps values and can be reliably estimated at lower SNR's with increase in data frames. The

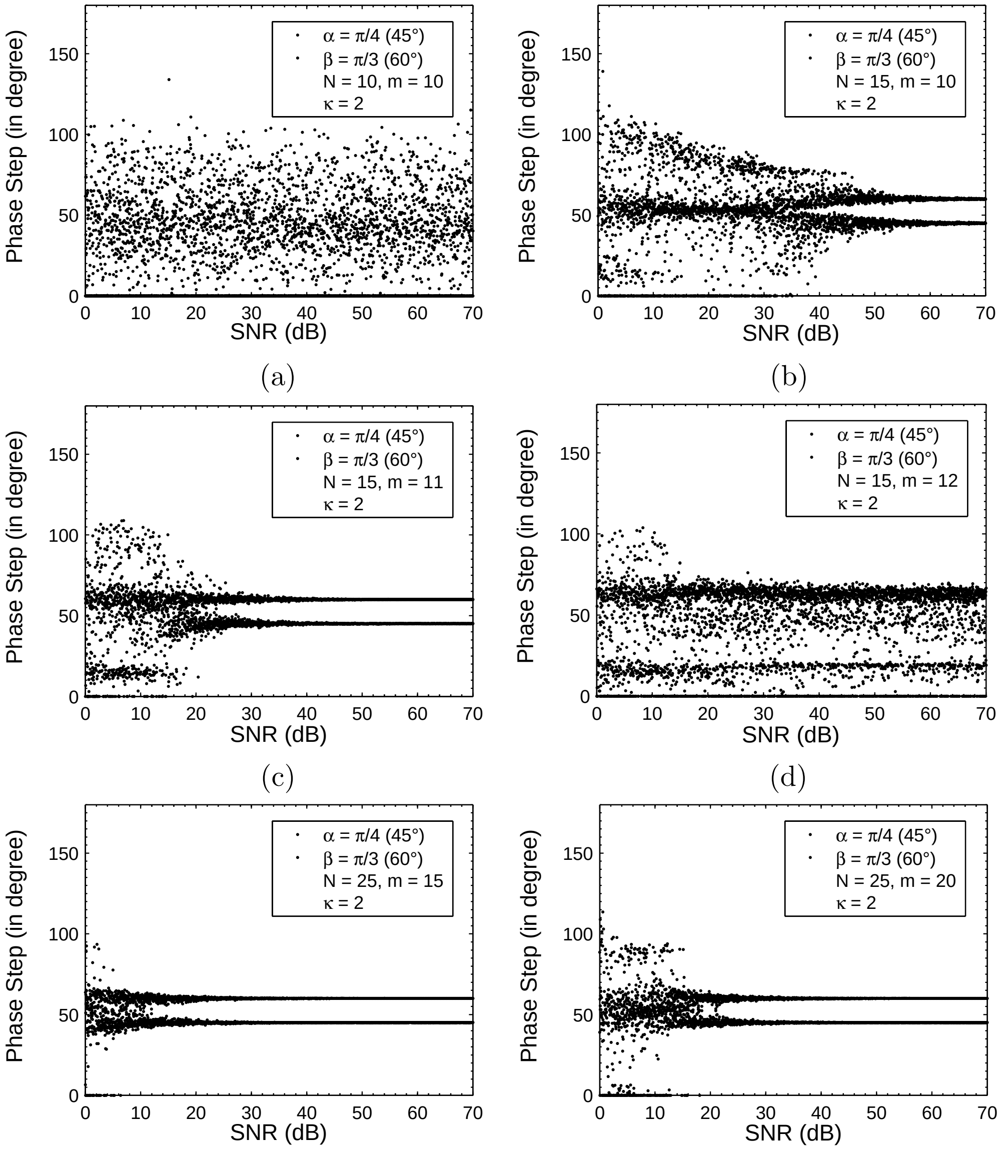

(a) (b) (c) (d) (e) (f)

Fig. 6.4: Plot of phase step α and β (in degree) versus SNR at an arbitrary pixel location on a data frame for $\kappa = 2$ and for different values of N and m in Eq. (4.8) using *forward-backward approach.*

forward-backward approach continues to exhibit better performance in the estimation of phase steps. Finally, the Vandermonde system of equations in Eq. (2.31) is applied for the estimation of φ_1 and φ_2. The statistical study on the error in the estimation of phase values φ_1 and φ_2 will be presented in Chapter 9.

6.4 Conclusion

To conclude, we have proposed a new approach for recovering phase distributions in presence of nonsinusoidal waveforms and in an interferometer containing multiple PZTs. The method enables to freely choose phase shifts between 0 and π. The forward-backward approach yields better phase step estimates as compared to the forward approach. The accuracy in the measurement of phase steps in the presence of additive white Gaussian noise has been shown to increase with large data frames. The proposed technique works well with both the diverging and converging beams since it first retrieves the dual phase step values pixel wise before applying them to the Vandermonde system of equation. The advantage of the proposed method also lies in its ability to measure the dual phase step values at each point after acquiring the data. Future research should focus on determining the smallest bounds for the phase steps that can be extracted.

Chapter 7

An Optimally Efficient Algorithm Based on Maximum-Likelihood Estimation

This chapter proposes a Maximum-Likelihood (ML) method based on spectral estimation theory for the estimation of phase distribution in interferometry in presence of nonsinusoidal waveforms, noise, and the miscalibration of the piezoelectric device. The proposed method also allows for the use of arbitrary phase steps. Maximum-Likelihood estimators are asymptotically efficient for sufficient data samples. The method is complemented well by the incorporation of a global search algorithm known as Probabilistic Global Search Lausanne (PGSL) for minimizing the ML function. The performance of the proposed method is studied in the presence of noise.

7.1 Introduction to Maximum-likelihood Estimator Algorithm

Maximum-Likelihood estimators (MLE) are optimally efficient with large data samples since they achieve the ultimate statistical performance inherent in Cramér-Rao bound (CRB) [129]. CRB gives lower bound on the attainable precision in estimation. The performance of any estimator cannot surpass the CRB.

Conceptually, first a ML function is designed for fringes recorded temporally at a pixel (n', j') on the CCD. The ML function is then minimized using a direct stochastic algorithm for global search known as probabilistic global search Lausanne [130]. Simulations on various benchmarking problems have shown that PGSL performs better than Genetic [131] and Simulated annealing algorithms [132]. In literature, ML functions are usually optimized using either of the two latter proposed algorithms or local search techniques. Genetic algorithm requires fine tuning of the parameters while Simulated annealing and the other local search techniques require initial guess which make them unattractive for implementation. Details on PGSL is a topic of next section.

The fringe intensity recorded at a pixel (n', j') for n^{th} phase step in an optical configuration involving single PZT in the presence of Gaussian noise is given by Eq. (2.1). Let us rewrite Eq. (2.1) in the following compact form

$$\mathbf{I}(n) = \mathbf{A}(\omega)\mathbf{\Psi}(n) + \mathbf{n}(n) \tag{7.1}$$

In Eq. (7.1), $\mathbf{I}(n) = [I(n-1)\ I(n-2)\ \cdot\ \cdot\ I(n-m)]$, $\mathbf{A}(\omega)$ has been described in Eq. (4.3), $\mathbf{\Psi}(n) = [\psi_0\ \psi_1\ \cdot\ \cdot\ \psi_(n)]^T$, and $\mathbf{n}(n) = [\eta(n-1)\ \eta(n-2)\ \cdot\ \cdot\ \eta(n-m)]^T$; where, for instance, $\psi_0 = I_{dc}$, $\psi_1 = a_{-1}\exp[-j(\varphi + \alpha n)]$. The point noteworthy is that the proposed representation in Eq. (7.1) can also be written for dual PZT, however, to keep our explanation simple, we study the case of only one PZT.

In Eq. (7.1), let $\digamma$ be a vector of unknown parameters that describes a collection of N data frames. The likelihood of $\digamma$, given the observations $\mathbf{I}(n)$, is $l(\mathbf{I},\digamma) \propto p(\mathbf{I},\digamma)$, where, l is the likelihood function and p is the conditional joint probability density function. Because $\mathbf{I}(n)$ are independent and identically distributed in presence of Gaussian noise,

$$l(\mathbf{I},\digamma) \propto p[I(0),\digamma][I(1),\digamma][I(2),\digamma]\cdots[I(N-1),\digamma] \tag{7.2}$$

Since in many applications, $p(\mathbf{I},\digamma)$ is exponential (e.g. Gaussian), it is easier to work with natural logarithm of $l(\mathbf{I},\digamma)$, written as $\mathtt{L}(\mathbf{I},\digamma) = \mathrm{ln}l(\mathbf{I},\digamma)$. The ML estimate is therefore $\hat{\digamma}$ that maximizes l or L for a particular set of measurements. Obtaining MLE involves specifying the likelihood function and finding those values of the parameters that give the function its minimum value. It is essential that if L is differentiable, its partial derivatives with respect to each of the unknown parameters in $\digamma$ are equal to zero.

The likelihood function for Eq. (7.1) is given by [129]

$$l = \frac{1}{(2\pi\sigma^2)^{N/2}} \exp\left\{-\frac{1}{2\sigma^2}\sum_{n=1}^{N}[\mathbf{I}(n) - \mathbf{A}(\omega)\mathbf{\Psi}(n)]^*[\mathbf{I}(n) - \mathbf{A}(\omega)\mathbf{\Psi}(n)]\right\} \tag{7.3}$$

Thus, the log-likelihood function is

$$ln(l) = \text{const} - \frac{N}{2}\mathrm{ln}\sigma^2 - \left\{\frac{1}{2\sigma^2}\sum_{n=1}^{N}[\mathbf{I}(n) - \mathbf{A}(\omega)\mathbf{\Psi}(n)]^*[\mathbf{I}(n) - \mathbf{A}(\omega)\mathbf{\Psi}(n)]\right\} \tag{7.4}$$

The likelihood in Eq. (7.4) can be evaluated with respect to σ^2 and $\{\psi_r\}_{r=0}^{n}$. Simple calculations show that ML estimators of these parameters are given by

$$\mathbf{\Psi}(n) = [\mathbf{A}^*\mathbf{A}]^{-1}[\mathbf{A}\mathbf{I}(n)] \quad n = 1, 2, ..., N \tag{7.5a}$$

$$\sigma^2 = \frac{1}{N}\sum_{n=1}^{N}[\mathbf{I}(n) - \mathbf{A}(\omega)\mathbf{\Psi}(n)]^*[\mathbf{I}(n) - \mathbf{A}(\omega)\mathbf{\Psi}(n)] \tag{7.5b}$$

After substituting Eq. (7.5a) into Eq. (7.5b), we obtain

$$\sigma^2 = \{\mathbf{I} - \mathbf{A}(\omega)[\mathbf{A}(\omega)^*\mathbf{A}(\omega)]^{-1}\mathbf{A}(\omega)^*\} \times \underbrace{\frac{1}{N}\sum_{n=1}^{N}\mathbf{I}^*(n)\mathbf{I}(n)}_{\mathbf{R}} \tag{7.6a}$$

$$= \text{trace}\{\mathbf{I} - \mathbf{A}(\omega)[\mathbf{A}(\omega)^*\mathbf{A}(\omega)]^{-1}\mathbf{A}(\omega)^*\} \times \mathbf{R} \tag{7.6b}$$

where, $\mathbf{I}$ is the identity matrix. Finally, substituting Eqs. (7.5a) and (7.5b) into Eq. (7.4), we obtain the following compact form for likelihood function

$$\text{constant} - N\ln \underbrace{\text{trace}\{\mathbf{I} - \mathbf{A}(\omega)[\mathbf{A}(\omega)^{*}\mathbf{A}(\omega)]^{-1}\mathbf{A}(\omega)^{*}\} \times \mathbf{R}}_{F(\digamma)} \tag{7.7}$$

Thus the ML estimate of $\digamma$ is given by the minimization of $F(\digamma)$. We thus minimize the function $F(\digamma)$ using PGSL. The following section explains in brief the PGSL.

7.2 Probabilistic Global Search Lausanne

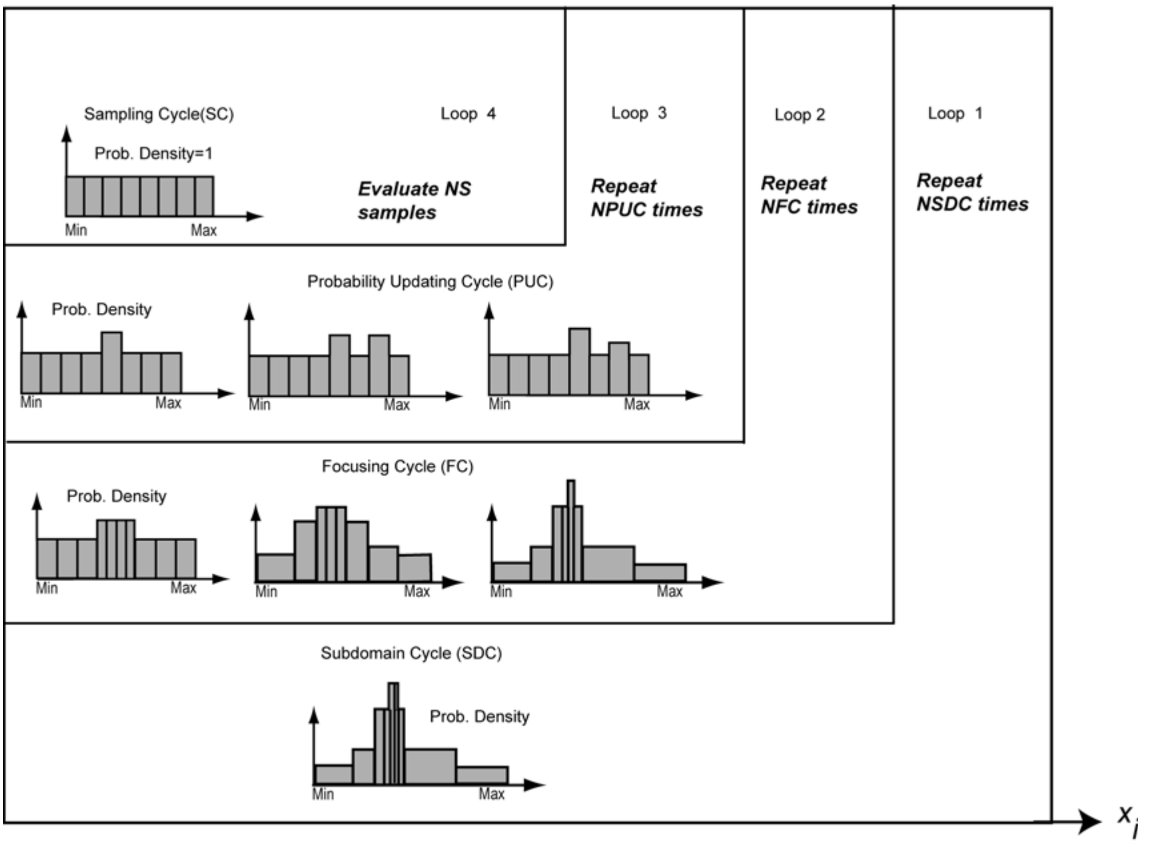

Fig. 7.1: The plot for various cycles in PGSL.

The PGSL algorithm operates by organizing an optimization search through four nested cycles, namely, Sampling, Probability updating, Focusing, and Subdomain cycle. Each cycle has a different role to perform while searching for the global, optimum, solution. The user first defines the bounds for each variable that is used with the objective function. The method then searches for the optimum value of the objective function defined in Eq. (7.7), which is performed by matching the measured with its predicted counterpart based on the estimated values of the variables (phase steps α and β, in the present case). The algorithm initially generates random values for each variable in the Sampling cycle. Assuming equal probability of finding good solution in the entire search space, the residual error is evaluated by substituting all generated solutions in Eq. (7.7). This allows for selecting all points where the residual error is minimum.

Probability updating and Focusing cycles subsequently refine search in the neighborhood of good solutions. Convergence to the optimum solution is achieved by means of Subdomain cycle. Following are the definitions of the terms used for describing the PGSL algorithm:

Solution point: A point consists of a set of values for each variable α and β.

Search space: The set of all potential solution points. It is an N-dimensional space with an axis corresponding to each variable. N denotes the total number of variables. The user defines the minimum and maximum values, commonly known as bounds of variables along each axis. A subset of the search space is called a subdomain.

Axis width: The difference between the minimum and the maximum along an axis of the search space or a subdomain.

Probability density function (PDF): The PDF of a variable is defined in the form of a histogram. The axis represented by the variable is discretised into a fixed number of intervals. In our case, the interval is chosen as 20. Uniform probability distribution is assumed within each interval.

The function of each cycle is described below:

Sampling cycle: The NS (number of samples) points are generated randomly by selecting a value for each variable according to its PDF. This sampling technique resembles the Monte Carlo technique. Each point is evaluated and the point having the minimum cost, BS (Best Sample), is selected.

Probability updating cycle: The sampling cycle is repeated NPUC (number of iterations in the probability updating cycles) times and after each iteration, the PDF of each variable is modified using the probability-updating algorithm. This ensures that the sampling frequencies in regions containing good points are increased. In the probability-updating algorithm the interval containing the value of the variable in BS is located. The probability of this interval is multiplied by a factor greater than 1. The PDF is subsequently normalized. The evolution of the PDF for a variable after several sampling cycles is illustrated in Fig. (7.1).

Focusing cycle: The probability updating cycle is repeated NFC (number of focusing cycles) times and after each iteration, the current best point, CBEST is selected. The PDF is updated by first locating the interval containing the value of each variable in CBEST. This interval is divided into four uniform subintervals. 50% probability is assigned to this interval so that about half the points will be generated within it. This probability is uniformly divided to its subintervals. The region outside this interval is subdivided into 16 subintervals. The widths of these subintervals are calculated such that the PDF decays exponentially away from it. After subdivisions, intervals no longer have the same width and probabilities are heavily concentrated near the current best. The evolution of PDF after several probability updating cycles is illustrated in Fig. (7.1).

Subdomain cycle: In the subdomain cycle, the focusing cycle is repeated NSDC (number of subdomain cycles) times and at the end of each iteration, the current space search is modified. In the beginning, the entire space is searched, but in subsequent iterations a subdomain of a smaller width is selected for search. The size of the subdomain decreases gradually and the solution converges to a point. For more details on PGSL, the reader is referred to Reference [130].

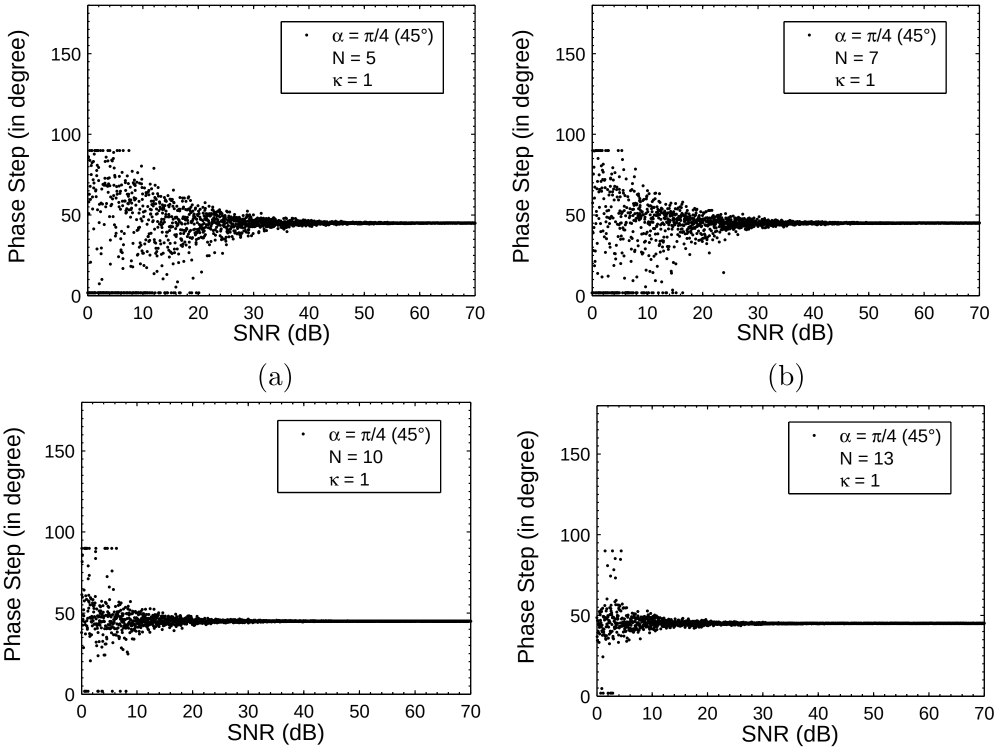

(a) (b)

(c) (d)

Fig. 7.2: Plot of phase step α (in degree) versus SNR at an arbitrary pixel location on a data frame for $\kappa = 1$ and for different values of N.

7.3 Maximum-likelihood Estimator for Phase Step Computation

The proposed algorithm is tested by applying it to computer generated fringes [133]. The phase step employed to the PZT is set as $\alpha = \pi/4$, while the phase φ is chosen as linear straight line fringe. We study the proposed concept for $\kappa = 1$ and $\kappa = 2$. The objective now, is to minimize the function in Eq. (7.7) using PGSL. In Eq. (7.7), only the bound for α needs to be set and we select the bound as $0 < \alpha < \pi$. The performance of the proposed concept is studied by generating additive white Gaussian noise having SNR from 0 to 70 dB and for data frames $N = 5, 7, 10,$ and 13 for $\kappa = 1$ and $N = 7, 10, 13,$ and 15 for $\kappa = 2$. It is observed that for smooth objective functions, the number of samples NS=2, are sufficient. The number of iterations to determine the global minima in other cycles are, probability updating cycle PUC=1, Focusing cycles Fc=40, and Subdomain cycle SDC=100.

The simulation results obtained from the proposed concept is shown in Fig. (7.2) for various data frames. Figures (7.2b)-(7.2d) show the influence of an increase in data frames on retrieving the phase steps. As the number of data frames increases, the phase steps can be reliably estimated at lower SNR's. For instance, Fig. (7.2b) shows that phase steps can be estimated from 45dB onwards as compared to 35dB onwards in Fig. (7.2c) for $\kappa = 1$. Similarly, Fig. (7.3d) show that phase steps can be estimated from 20dB onwards as compared to 40dB onwards in Fig. (7.3a) for $\kappa = 2$.

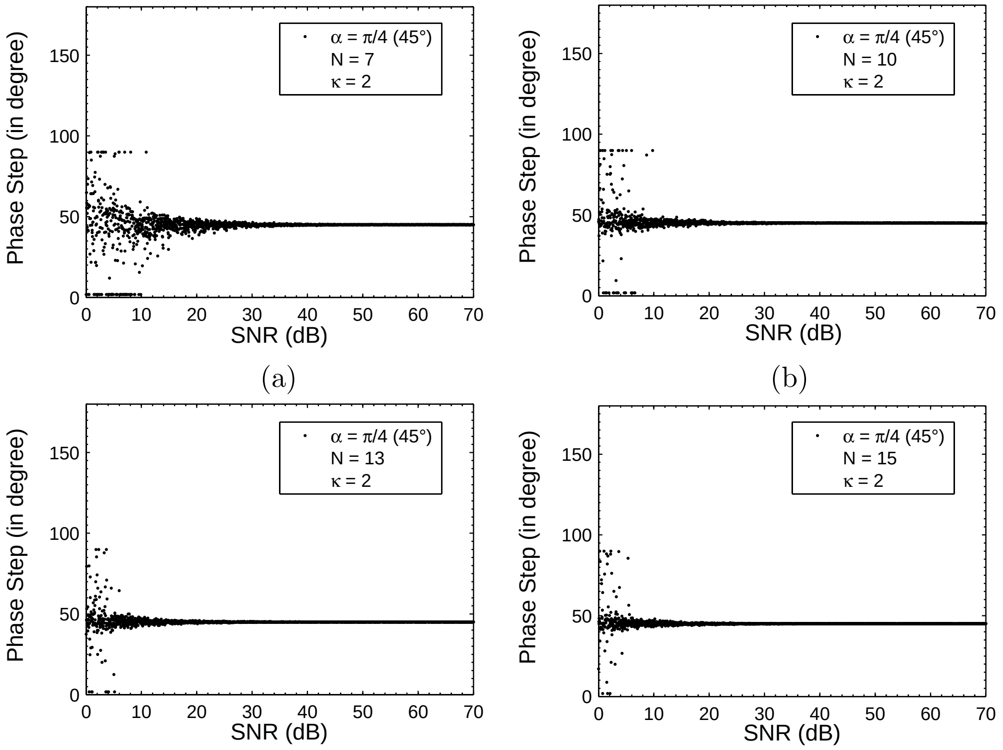

(a) (b)

(c) (d)

Fig. 7.3: Plot of phase step α (in degree) versus SNR at an arbitrary pixel location on a data frame for $\kappa = 2$ and for different values of N.

7.4 Maximum-likelihood Estimator for Holographic Moiré

The proposed algorithm is further tested by applying it to computer generated moiré fringes [134]. The phase steps employed to the two PZT's are set as $\alpha = \pi/4$ and $\beta = \pi/3$, $\kappa = 2$, and phases φ_1 and φ_2 in Eq. (2.1) are chosen as linear straight line fringes with different pitches. Since the number of harmonics can be easily determined using well known signal processing principles, we assume that the number of harmonics κ and hence the number of frequencies f is known. A closer look at Eq. (7.7) suggests that only the bounds for α and β need to be set. Therefore, let us select the bound as $0 < \alpha, \beta < \pi$. We study the performance of the proposed concept by generating additive white Gaussian noise that has signal-to-noise ration (SNR) from 0 to 70 dB and for data frames N = 10, 13, 15, 20. The same values for various cycles in the PGSL algorithm is chosen for the present study.

The simulation results obtained from the proposed concept is shown in Fig. (7.4) for various data frames. As expected, the phase steps cannot be estimated by use of $N = 10$ data frames when $f = 9$. Figures (7.4b)-(7.4d) show the influence of an increase in data frames on retrieving the phase steps. As the number of data frames increases the phase steps can be reliably estimated at lower SNR's. For instance, Fig. (7.4c) shows that phase steps can be estimated from 27dB onwards as compared to 45dB onwards in Fig. (7.4b). Similarly, Fig. (7.4) show that phase steps can be estimated from 18dB onwards.

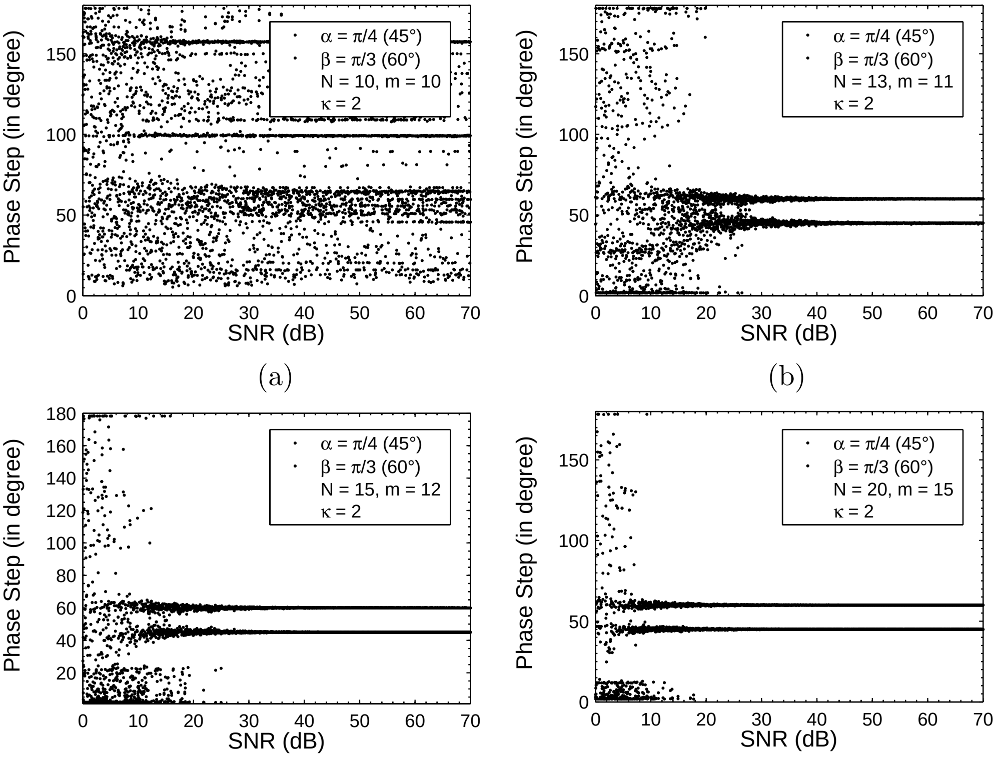

(a) (b)

(c) (d)

Fig. 7.4: Plot of phase step α and β(in degree) versus SNR at an arbitrary pixel location on a data frame for $\kappa = 2$ and for different values of N.

7.5 Discussion on ML method

This Chapter discussed a novel approach to estimate phase distribution in an interferogram in the presence of noise. For this purpose, a ML method was chosen as this method is known to be optimally efficient for very large data samples. However, such a case is not realistic in applications involving PZT and hence tradeoff is sought between the accuracy and the number of data frames. The proposed method handles nonsinusoidal waveforms and also allows the use of arbitrary phase steps. The statistical accuracy of the proposed method will be presented in Chapter 9.

Chapter 8

Constraints in Dual Phase Shifting Interferometry

The concept of dual phase shifting interferometry in holographic moiré is not straightforward and certain guidelines need to be considered for its successful implementation. There are basically three approaches of realizing dual phase shifting in holographic moiré for retrieving multiple phases, namely, traditional phase shifting, flexible least-squares, and signal processing methods. The study reveals that these methods cannot be applied straightforward to retrieve phase information and discusses the constraints associated with these methods. Since the signal processing method is the most efficient among these approaches, the chapter discusses significant issues involved in the successful implementation of the concept. In this approach the knowledge of the pair of phase steps is of paramount interest. Thus the choice of the pair of phase steps that can be applied to the phase shifting devices in the presence of noise is discussed. In this context, we present a theoretical study using Cramér-Rao bound with respect to the selection of the pair of phase step values in the presence of noise.

8.1 Introduction

Holographic moiré is an efficient technique for the nondestructive evaluation of rough objects. The method functions by integrating two holographic interferometers within one system. The result is produced in the form of a moiré. However, the complex nature of the interferometer and the beat inherent in the process precludes the use of standard phase shifting procedures to holographic moiré [100, 101].

Information carried by the carrier and moiré can be decoded by either the traditional phase shifting approach or by least-squares fit techniques or, by the introduction of signal processing concepts in phase shifting interferometry. In the traditional approach, we refer to three-frame, five-frame, and seven-frame algorithms [100, 101] which allow for accommodating dual PZTs. By least-squares fit technique, we extend the least squares fit data reduction method proposed by Morgan [78] and Grievenkamp [79] to accommodate dual phase shifting devices PZTs. On the other hand, the signal processing approach allows for applying high resolution frequency estimation techniques such as polynomial rooting (annihilation method) [1, 108], state-space approach [115, 135] MUltiple-SIgnal Classification (MUSIC) [119, 121], Minimum-Norm (min-norm) [124, 125, 125], Estimation of Signal Parameters via Rotational Invariance Technique (ESPRIT) [127, 128], and the Maximum-Likelihood Estimation (MLE) [133, 134] to optical configurations including two PZTs.

However, these approaches have inherent limitations and cannot be applied straightforward to configurations such as holographic moiré for the simultaneous extraction of two orthogonal displacement components. For instance, in the traditional approach, the retrieval of information is not straightforward and the phase map corresponding to the carrier yields a phase pattern corrupted by moiré and vice-versa. Hence, additional step needs to be associated to the measurement to yield uncorrupted phase maps. On the other hand, in both the least squares fit technique and the signal processing approach, though the phase steps imparted by the PZTs can be arbitrary, the selection of phase steps in the presence of noise is crucial to the successful implementation of the concept.

In this context, the objective of this chapter is to discuss in detail the constraints encountered while following these approaches. We believe that understanding the conditions that are necessary to employing these algorithms is of paramount importance for the successful implementation of the proposed concept. Since, the signal processing approach is the most efficient among these approaches, we present a statistical analysis using Cramér-Rao lower bound [136] for the selection of the optimal pair of phase steps in the presence of noise. Once the phase steps have been estimated within an allowable accuracy, the Vandermonde system of equations [114] can be designed for the determination of phases.

As a case study, we will consider the five-frame algorithm (traditional approach) [101] and the annihilation method (spectral estimation approach) [108]. The performance of other estimators such as MUSIC, min-norm and ESPRIT can also be studied in a similar way. The present study is expected to provide the guidelines for applying dual phase shifting procedures to holographic moiré.

8.2 Dual phase shifting interferometry: methods and their limitations

8.2.1 Traditional approach: a five-frame algorithm

Figure (1.1) shows the configuration for the holographic moiré setup. Recall that the intensity equation for moiré is given by Eq. (1.1). The sum and difference of phases can be obtained by applying dual phase steps in the two arms of holographic moiré . Thus, in order to recover the sum of phase term $\Phi_+ = \varphi_1(P) + \varphi_2(P)$, we apply pairs of phase steps $(-2\alpha, -2\beta)$, $(-\alpha, -\beta)$, $(0, 0)$, (α, β), and $(2\alpha, 2\beta)$ to the PZTs. Frames I_1, I_2, I_3, I_4, and I_5 corresponding to these phase steps are recorded in the computer [100, 101]. Assuming, $\alpha = \beta = \pi/2$, the term corresponding to the sum of phases is given by

$$\Phi_+ = 2\tan^{-1}\left[\frac{2(I_2 - I_4)}{2I_3 - I_1 - I_5}\right], \text{ for } \varphi_1(P) - \varphi_2(P) \neq (2\chi + 1)\pi \tag{8.1}$$

where, χ is some integer constant. Similarly, in order to recover the difference of phase term, $\Phi_- = \varphi_1(P) - \varphi_2(P)$, we apply pairs of phase steps $(-2\alpha, 2\beta)$, $(-\alpha, \beta)$, $(0, 0)$, $(\alpha, -\beta)$, and $(2\alpha, -2\beta)$ to the PZTs. Frames I_1, I_2, I_3, I_4, and I_5 corresponding to these phase steps are recorded in the computer. Assuming, $\alpha = \beta = \pi/2$, the term corresponding to the difference of phases is given by

$$\Phi_- = 2\tan^{-1}\left[\frac{2(I_2 - I_4)}{2I_3 - I_1 - I_5}\right], \text{ for } \varphi_1(P) + \varphi_2(P) \neq (2\chi + 1)\pi \tag{8.2}$$

Constraints in traditional approach

Although $\alpha = \beta = \pi/2$ in Eqs. (8.1) and (8.2) minimizes the first order calibration errors in PZTs, the conditions in Eqs. (8.1) and (8.2) are the main constraints when it comes to extracting the wrapped phases. For instance, in Eq. (8.1) whenever, $\varphi_1(P) - \varphi_2(P) = (2\chi + 1)\pi$, the equation becomes indeterminate. Because of the arctangent operator this indeterminacy manifests itself as a discontinuity and Φ_+ jumps by either $+2\pi$ or -2π depending upon the sign. Hence, while extracting the wrapped sum of phases, the fringes corresponding to moiré are also seen to modulate the wrapped phase pattern, Φ_+.

The above mentioned phenomenon is better understood by observing the simulated moiré fringes in Figs. (1.2a) and (1.2b). Figure (1.2a) and (1.2b) show the fringe pattern (512 × 512 pixels) corresponding to Eq. (1.2), under the assumption $\Phi_{ran1} = \Phi_{ran2} = 0$ and $\Phi_{ran1} = \Phi_{ran2} \neq 0$, respectively. The wrapped phase maps corresponding to Φ_+ using Eq. (1.3) for Figs. (1.2a) and (1.2b) are shown in Figs. (1.3a) and (1.3b), respectively. The figures show that the information carried by the sum of phases is corrupted by the moiré fringes. The figures are plotted without taking into consideration the constraints in Eq. (1.3). Figure (8.1) shows a typical plot along a row in Fig. (1.3a). From the plot it can be observed that whenever, $\varphi_1(P) - \varphi_2(P) = (2\chi + 1)\pi$, the discontinuity (shown by R1) is $\pm 2\pi$ in Φ_+. However, this discontinuity can be removed by processing the wrapped phase term Φ_+ using a computer. An efficient way to perform this task is to resample the wrapped phase using the cosine operator. Since, at $\varphi_1(P) - \varphi_2(P) = (2\chi + 1)\pi$, there is a jump of $\pm 2\pi$, from basic trigonometry we get $\cos[\varphi_1(P) - \varphi_2(P) \pm (2\chi + 1)\pi] = \cos[\varphi_1(P) - \varphi_2(P)]$. Hence, the discontinuity is removed. In Fig. (8.1) $f(x)$ represents the continuous function obtained from $f(x) = \cos(\Phi_+)$. However, to make the procedure compatible with most of the commercially available unwrapping softwares, the computer generated phase steps can be imparted to $f(x)$. For instance, phase shifts of 0, $\pi/2$, π, and $3\pi/2$ can be applied to extract the wrapped phase. Figures (8.2a)-(8.2b) shows that the discontinuities due to constraints in Eq. (1.3) are removed. Similarly, when it comes to extracting the information carried by moiré using Eq. (8.2), we observe that the phase map is corrupted by carrier fringes. The phase maps corresponding to Φ_- in Figs. (1.2a)-(1.2b) are shown in Figs. (1.4a)-(1.4b), respectively. The plot in Fig. (8.3) drawn across a central row shows that whenever $\varphi_1(P) + \varphi_2(P) = (2\chi + 1)\pi$, the discontinuity (shown by R2) is $\pm 2\pi$ in Φ_-. This discontinuity is removed in a similar way as explained in the previous paragraph.

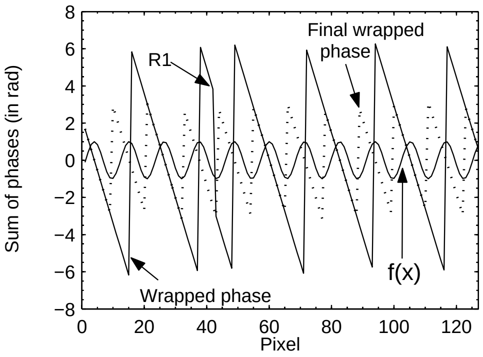

Fig. 8.1: Typical plot for wrapped sum of phases $\varphi_1 + \varphi_2$ (in radians) shown in Fig. (1.3a). In plot the pixels in the central row from pixel (256,0) till pixel (256, 127) is shown. In the plot, R1 shows the discontinuity in phase since $\varphi_1 - \varphi_2 = \pm 2\pi$.

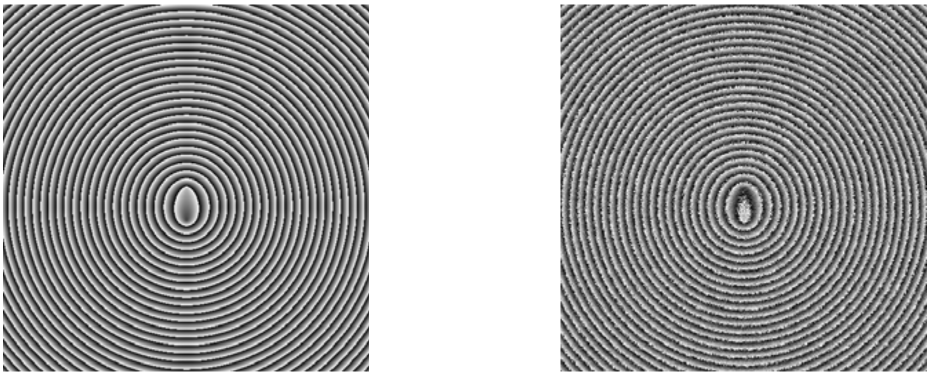

(a) (b)

Fig. 8.2: The map corresponding to the wrapped sum of phases $\varphi_1 + \varphi_2$ obtained using Eq. (1.3) for the fringe map in (a) Fig. (1.2a) and (b) Fig. (1.2b).

Figure (8.3) shows the continuous function $g(x)$ obtained from $g(x) = \cos(\Phi_-)$. Applying phase shifts of 0, $\pi/2$, π, and $3\pi/2$ to $g(x)$ and solving the four phase shifted images results in the estimation of wrapped difference of phases. Figures (8.4a)-(8.4b) show the wrapped difference of phases obtained for fringes in Figs. (1.2a)-(1.2b), respectively.

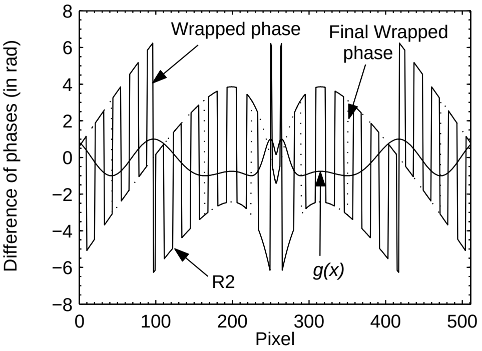

Fig. 8.3: Typical plot for wrapped difference of phases $\varphi_1 - \varphi_2$ (in radians) shown in Fig. (1.4a). In plot the pixels in the central row from pixel (256, 0) till pixel (256, 511) is shown. In the plot, R2 shows the discontinuity in phase since $\varphi_1 + \varphi_2 = \pm 2\pi$.

The same phenomenon is also observed for the three-frame [100] and seven-frame [101] algorithms. The point which needs to be emphasized here is that the straightforward adaptation of these algorithms to dual phase stepping is not possible. Moreover, these algorithms are sensitive to nonsinusoidal wavefronts (a consequence of detector nonlinearity or multiple reflections inside the laser cavity, or the phase shifter itself). These algorithms also do not offer any flexibility either in the selection of phase step values α and β or in the use of non-collimated wavefronts for phase shifting.

8.2.2 Flexible least-squares method

The use of least squares fitting techniques has assumed greater significance in simple phase shifting interferometry [78, 79] because of its ability to allow arbitrary phase steps. The concept

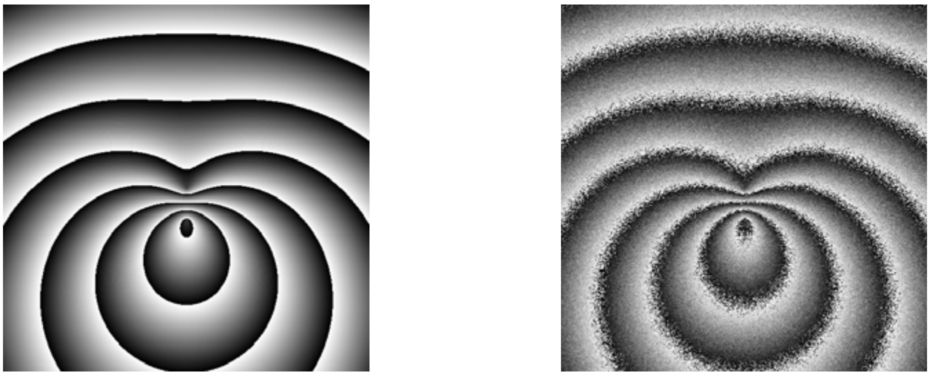
(a) (b)

Fig. 8.4: The figure shows the final wrapped difference of phases obtained after removing the $\varphi_1 + \varphi_2 = \pm 2\pi$ discontinuity. Figure (a) shows the wrapped difference of phases for the fringe map in (a) Fig. (1.2a) while (b) shows the wrapped phase for fringe in Fig. (1.2b).

of least-squares fit has primarily been shown to be effective in configurations involving a single PZT. It can, however, be extended to holographic moiré shown in Fig. (1.1), albeit, with some constraints. The equation for holographic moiré defined by Eq. (1.2) can be written as

$$I_n = I_{dc} + \gamma \cos\alpha_n + \delta \sin\alpha_n + \mu \cos\beta_n + \nu \sin\beta_n \quad \text{for } n = \ 0, 1, 2, ..., N-1 \tag{8.3}$$

where, $\gamma = I_{dc} V \cos\varphi_1(P)$, $\delta = -I_{dc} V \sin\varphi_1(P)$, $\mu = I_{dc} V \cos\varphi_2(P)$, and $\nu = -I_{dc} V \sin\varphi_2(P)$. Here, N is the number of data frames. Since Eq. (8.3) is linear with respect to unknown coefficients I_{dc}, γ, δ, μ, and ν, we can use least-squares technique to minimize $E(P)$, defined as

$$E(P) = \sum_{n=0}^{N-1} \left[I_{dc} + \gamma \cos\alpha_n + \delta \sin\alpha_n + \mu \cos\beta_n + \nu \sin\beta_n - I_n \right]^2 \tag{8.4}$$

For the best fit, the error function in Eq. (8.4) should be minimized (min$E(P)$). This is done by setting the first derivative of $E(P)$ with respect to the unknown coefficients I_{dc}, γ, δ, μ, and ν, written as $\partial E/\partial I_{dc}$, $\partial E/\partial \gamma$, $\partial E/\partial \delta$, $\partial E/\partial \mu$, and $\partial E/\partial \nu$, respectively, equal to zero. The resulting equations can be written in the matrix form as $\mathbf{B} = \mathbf{A}^{-1}\mathbf{X}$, where,

$$\mathbf{A} = \begin{bmatrix} N & \sum\cos\alpha_n & \sum\sin\alpha_n & \sum\cos\beta_n & \sum\sin\beta_n \\ \sum\cos\alpha_n & \sum\cos^2\alpha_n & \sum\cos\alpha_n\sin\alpha_n & \sum\cos\alpha_n\cos\beta_n & \sum\cos\alpha_n\sin\beta_n \\ \sum\sin\alpha_n & \sum\cos\alpha_n\sin\alpha_n & \sum\sin^2\alpha_n & \sum\sin\alpha_n\cos\beta_n & \sum\sin\alpha_n\sin\beta_n \\ \sum\cos\beta_n & \sum\cos\alpha_n\cos\beta_n & \sum\sin\alpha_n\cos\beta_n & \sum\cos^2\beta_n & \sum\sin\beta_n\cos\beta_n \\ \sum\sin\beta_n & \sum\cos\alpha_n\sin\beta_n & \sum\sin\alpha_n\sin\beta_n & \sum\sin\beta_n\cos\beta_n & \sum\sin^2\beta_n \end{bmatrix} \tag{8.5}$$

$\mathbf{B} = [I_{dc}\ \gamma\ \delta\ \mu\ \nu]^T$, and $\mathbf{X} = [\sum I_n\ \sum I_n\cos\alpha_n\ \sum I_n\sin\alpha_n\ \sum I_n\cos\beta_n\ \sum I_n\sin\beta_n]^T$. Here the simulation is carried out from $n = 0$ to $n = N-1$. The solution to the above matrix equation results in the determination of the unknown coefficients I_{dc}, γ, δ, μ, and ν, and subsequently, in the determination of φ_1 and φ_2. The sum and difference of phases can then be obtained using

$$\Phi_+ = \tan^{-1} \frac{\delta\mu + \nu\gamma}{\delta\nu - \mu\gamma} \tag{8.6a}$$

$$\Phi_- = \tan^{-1} \frac{\gamma\nu - \mu\delta}{\gamma\mu + \nu\delta} \tag{8.6b}$$

Constraints in flexible least-squares method

The main constraint in flexible least-squares method is that the phase steps should be carefully selected such that matrix **A** is non-singular. It has also been observed that the use of sequential phase steps such as $n\alpha$ and $n\beta$ in matrix **A** results in the determinant to be zero. In practical situations although the successive phase steps cannot be exact multiples of $n\alpha$ and $n\beta$, the resulting matrix in this case will be nearly singular or poorly conditioned. Therefore, if the least squares technique is applied, then only few arbitrary phase steps should be selected such that the matrix **A** is non-singular. For instance, if thirteen data frames are acquired and, $\alpha = 40°$ and $\beta = 20°$, then five data frames corresponding to frames $n = 0, 2, 5, 8$ and 10 can be selected in a non-regular order. This would result in matrix **A** to be non-singular. It is also observed that even if the matrix **A** is not well conditioned, mathematical tools such as MATLAB [137] may still compute the inverse of the matrix **A**. Therefore, it is always advisable to check whether the matrix is well conditioned or not.

Hence, the well know generalized data reduction technique proposed by Morgan [78] and Grievenkamp [79] cannot be extended straightforward to holographic moiré, since utmost care is required in the selection of the pair of phase steps. The other method by which the generalized holographic moiré can be realized is by designing the Vandermonde system of equations. A Vandermonde matrix usually arises in the polynomial least squares fitting, Lagrange interpolating polynomials, or in the statistical distribution of the distribution moments [59,114]. The solution of $N \times N$ Vandermonde matrix requires N^2 operations. The advantage of Vandermonde matrix is that its determinant is always nonzero (hence invertible) for different values of $n\alpha$ and $n\beta$. Hence, the matrix for determining phases φ_1 and φ_2 can be written in the form

$$\begin{bmatrix} \exp(j\alpha_0) & \exp(-j\alpha_0) & \exp(j\beta_0) & \exp(-j\beta_0) & 1 \\ \exp(j\alpha_1) & \exp(-j\alpha_1) & \exp(j\beta_1) & \exp(-j\beta_1) & 1 \\ \vdots & \vdots & \vdots & \vdots & \vdots \\ \exp(j\kappa\alpha_N) & \exp(-j\kappa\alpha_N) & \exp(j\beta_N) & \exp(-j\beta_N) & 1 \end{bmatrix} \begin{bmatrix} \ell \\ \ell^* \\ \wp \\ \wp^* \\ I_{dc} \end{bmatrix} = \begin{bmatrix} I_0 \\ I_1 \\ \vdots \\ I_{N-1} \end{bmatrix} \tag{8.7}$$

where, (α_0, β_0), (α_1, β_1),..,and $(\alpha_{N-1}, \beta_{N-1})$ are phase steps for frames I_0, I_1, I_2,...,and I_{N-1}, respectively. The phase distribution φ_1 and φ_2 are subsequently computed from the argument of ℓ and $\wp$, where $\ell = 0.5 I_{dc} V \exp(j\varphi_1)$ and $\wp = 0.5 I_{dc} V \exp(j\varphi_2)$. Here, $*$ denotes the complex conjugate.

A point to note is that in phase shifting interferometry using the least-squares fit method, the first step involves the exact determination of the phase steps while the second step involves the determination of the phase distribution. The method proposed by Lai and Yatagai [90] for the estimation of phase steps in real time cannot be applied in a straight-forward manner here as the procedure is applicable to a single PZT based configuration only. In such a case the algorithm suggested by Patil *et al.* [138] using stochastic approach seems to be the most appropriate. The algorithm however is sensitive to noise and can only work well if the data is assumed to have a high signal to noise ratio (SNR). To overcome this problem, high resolution techniques have been proposed. Limitations associated with the use of high-resolution techniques is the topic of the next subsection.

8.2.3 Signal processing approach

In the signal processing approach, a parallelism is drawn between the frequencies that are present in the spectrum and the phase steps imparted to the PZTs. The problem therefore reduces to estimating the frequencies or in other words the phase steps. Once the phase steps have been estimated, the Vandermonde system of equation shown in Eq. (2.31) can be applied for the extraction of phase distributions. Patil *et al.* [6-10] have introduced signal processing algorithms to configurations involving single and multiple PZTs. The advantage of these approaches lies in their ability to compensate for the errors arising due to non-sinusoidal wavefronts and PZT miscalibrations. These algorithms also allow the use of spherical wavefronts and arbitrary phase steps between 0 and π radians. The number of data frames that these methods require is equal to at least twice the number of frequencies that are present in the spectrum. Hence, for dual PZTs and for harmonic $\kappa = 1$, we need at least $N = 10$ data frames. Since, discussion of each signal processing algorithms is beyond the scope, let us consider as a case study, the case of one such algorithm based on the design of an annihilation filter.

Annihilation filter method

In the annihilation filter method, we transform the discrete time domain signal I_n in Eq. (1.2) into a complex frequency domain by taking its Z-transform. Let the Z-transform of I_n be denoted by $\mathbf{I}(z)$. The objective is to design another polynomial $\mathbf{P}(z)$ termed as annihilation filter which has zeros at frequencies associated with $\mathbf{I}(z)$. This in turn would result in $\mathbf{I}(z)\mathbf{P}(z) = 0$. The phase steps α and β are estimated by extracting the roots of the polynomial $\mathbf{P}(z)$. The details on the design of annihilation filter is explained in Chapter 2.

Constraints in signal processing approach

Of the three approaches, the signal processing approach seems to be the most promising as it is effective in minimizing some of the commonly occurring systematic and random errors during the measurement. However, the constraint in the signal processing approach is the selection of the pair of phase steps that are applied to dual PZT's. In the presence of low signal-to-noise ratio (SNR), a careful selection of the pair of phase steps with limited number of data frames is necessary. Since, noise plays an important role in the successful implementation of the concept, a sound knowledge of the allowable phase steps is of prime importance. Hence, there is a need to study the statistical characteristics of phase shifted holographic moiré (which is independent of the estimator itself) using Cramér-Rao bound. In the next section we present the CRB for holographic moiré in the context of the selection of the phase steps. Once the CRB is obtained the study will focus on the performance evaluation of the annihilation filter method.

8.3 Optimizing phase shifts by signal processing approach

This section provides useful guidelines to optimizing the selection of phase step values obtained by signal processing approach. This study can be performed by deriving the CRB for holographic moiré. The CRB provides valuable information on the potential performance of the estimators.

The CRBs are independent of the estimation procedure and the precision of the estimators cannot surpass the CRBs. In this context, we will first derive the CRB for the phase steps α and β as a function of SNR and N. Although the phase steps α and β can be arbitrary for pure intensity signal, the central question is: what is the smallest difference between the phase steps α and β that can be retrieved reliably by any estimator as a function of SNR and N? Hence, we need to determine all the allowable values of phase steps α and β at a particular SNR and N. The reason why we are interested in computing the smallest phase step difference is to provide an experimentalist with a fair idea of phase steps which must be selected at a particular SNR and N, so that the phases φ_1 and φ_2 can be estimated reliably. Suppose that inadvertently, the two phase steps are chosen very close to one another and the measurements are performed at a low value of SNR. In such as case, the phases φ_1 and φ_2 cannot be estimated reliably. However, for the same value of SNR, if the two phase steps α and β are far apart, the phase values φ_1 and φ_2 can be reasonably estimated. Hence, there is a need to set up guidelines for the selection of the phase steps.

In order to respond to this query, we will derive the mean square error (MSE) for difference in phase steps $\alpha - \beta$ as a function of SNR which will indicate the theoretical Cramér-Rao lower bounds to the MSE. The Cramér-Rao bound can then be compared with the MSE obtained by any estimator (in the present case we will study the annihilation filter method). For this, we perform 500 Monte-Carlo simulations at each SNR and the separation between the phase steps α and β is varied from 0 to 100%.

Two scenarios are possible. First, the MSE obtained from the estimator is below the CRB. We attribute this observation to the non-reliability in the estimated phase steps and discard those values of separation between α and β in which the MSE is below the CRB. Second, the MSE of the estimator is above the CRB. In such a case, we infer that closer the MSE of the estimator is to the CRB, the more efficient is the estimator. Of course, for an unbiased estimator, the MSE obtained by the estimator can never reach the theoretical CRB for limited number of sample points. In the present study, we derive the CRB for the phase steps and compare the performance of the annihilation filter method with the CRB.

8.3.1 Cramér-Rao bound for holographic moiré

Let $\mathbf{I}' = \mathbf{I} + \eta$ denote the vector consisting of measured intensities in the presence of noise η, where $\mathbf{I} = [I_0\ I_1\ I_2\ \cdot\ I_{N-1}]^T$. The vector $\mathbf{I}'$ is characterized by the probability density function $p(\mathbf{I}'; \Psi) = p(\mathbf{I}')$, where Ψ is the set of unknown parameters in the moiré fringes. In the present case, $\Psi = (I_{dc1}, I_{dc2}, V_1, V_2, \varphi_1, \varphi_2, \alpha, \beta)^T$, where subscripts 1 and 2 refer individually to the two arms of the interferometer. Note that in Eq. (1.2), it was assumed that $I_{dc1} = I_{dc2} = I_{dc}$ and $V_1 = V_2 = V$. Therefore, I_{dc1} and I_{dc2} are the average intensities while V_1 and V_2 are the fringe visibilities in the two arms. Now, if $\hat{\Psi}$ is an unbiased estimator of the deterministic Ψ, then the covariance matrix of the unbiased estimator, $E\{\hat{\Psi}\hat{\Psi}^T\}$, where E is an expectation operator, is bounded by its lower value given by [136]

$$E\{\hat{\Psi}\hat{\Psi}^T\} \geq \mathbf{J}^{-1} \tag{8.8}$$

where, $\mathbf{J}$ is the Fisher Information matrix. This matrix is defined as [136]

$$\mathbf{J} = E\left\{\left[\frac{\partial}{\partial \Psi}\log p(\mathbf{I}')\right]\left[\frac{\partial}{\partial \Psi}\log p(\mathbf{I}')\right]^T\right\} \tag{8.9}$$

In other words, if $\hat{\psi}_r$ (any r^{th} element of Ψ) is an unbiased estimator of deterministic ψ_r, based on $\mathbf{I}'$, whose CRB is given by

$$E\{\hat{\Psi}_r^2\} \geq \mathbf{J}_{r,r}^{-1}, \text{ for } r = 1, 2, 3, ..., 8 \tag{8.10}$$

where, $\mathbf{J}_{r,r}^{-1}$ is the (r,r) element in matrix $\mathbf{J}^{-1}$. Assuming η is the additive white Gaussian noise with zero mean and variance σ^2, the probability density function $p(\mathbf{I}';\Psi)$ is defined by the mean and variance of the noise. Thus, the joint probability of the vector $\mathbf{I}'$ is given by

$$p(\mathbf{I}';\Psi) = \left(\frac{1}{\sqrt{2\pi}\sigma}\right)^N \exp\left[-\frac{1}{2\sigma^2}\sum_{n=0}^{N-1}(I'_n - I_n)^2\right] \tag{8.11}$$

It is well understood that the CRB for each unknown parameter can be determined by observing the diagonal elements of the inverse of the Fisher Information matrix, $\mathbf{J}^{-1}$. Simplifying Eq. (8.11) by taking the logarithmic function (note that $\log p$ is asymptotic to $p(\mathbf{I}';\Psi)$), we obtain

$$\log p = \text{constant } - \frac{1}{2\sigma^2}\sum_{n=0}^{N-1}(I'_n - I_n)^2 \tag{8.12}$$

Differentiating Eq. (8.12) with the r^{th} element in Ψ, say ψ_r, we obtain,

$$\frac{\partial \log p}{\partial \psi_r} = \frac{1}{\sigma^2}\sum_{n=0}^{N-1}\frac{\partial I_n}{\partial \psi_r}(I'_n - I_n) \tag{8.13}$$

Similarly, Eq. (8.13) can be differentiated with respect to ψ_s. Therefore Eq. (8.8) for the r^{th} and s^{th} element in Ψ can be written as

$$J_{r,s} = E\left\{\frac{1}{\sigma^4}\sum_{n=0}^{N-1}\frac{\partial I_n}{\partial \psi_r}(I'_n - I_n)\sum_{l=0}^{N-1}\frac{\partial I_l}{\partial \psi_s}(I'_l - I_l)\right\} \tag{8.14}$$

Equation (8.14) can be simplified into the following compact form

$$J_{r,s} = \frac{1}{\sigma^2}\sum_{n=0}^{N-1}\frac{\partial I_n}{\partial \psi_r}\frac{\partial I_n}{\partial \psi_s} \tag{8.15}$$

Finally, the lower bounds are given by variance, $\text{var}(\hat{\psi}_r) \geq \mathbf{J}_{r,r}^{-1}$. In the present example the typical Fisher Information matrix will be

$$\mathbf{J} = \begin{bmatrix} J_{I_{dc1},I_{dc1}} & J_{I_{dc1},I_{dc2}} & J_{I_{dc1},V_1} & J_{I_{dc1},V_2} & J_{I_{dc1},\varphi_1} & J_{I_{dc1},\varphi_2} & J_{I_{dc1},\alpha} & J_{I_{dc1},\beta} \\ J_{I_{dc2},I_{dc1}} & J_{I_{dc2},I_{dc2}} & J_{I_{dc2},V_1} & J_{I_{dc2},V_2} & J_{I_{dc2},\varphi_1} & J_{I_{dc2},\varphi_2} & J_{I_{dc2},\alpha} & J_{I_{dc2},\beta} \\ J_{V_1,I_{dc1}} & J_{V_1,I_{dc2}} & J_{V_1,V_1} & J_{V_1,V_2} & J_{V_1,\varphi_1} & J_{V_1,\varphi_2} & J_{V_1,\alpha} & J_{V_1,\beta} \\ J_{V_2,I_{dc1}} & J_{V_2,I_{dc2}} & J_{V_2,V_1} & J_{V_2,V_2} & J_{V_2,\varphi_1} & J_{V_2,\varphi_2} & J_{V_2,\alpha} & J_{V_2,\beta} \\ J_{\varphi_1,I_{dc1}} & J_{\varphi_1,I_{dc2}} & J_{\varphi_1,V_1} & J_{\varphi_1,V_2} & J_{\varphi_1,\varphi_1} & J_{\varphi_1,\varphi_2} & J_{\varphi_1,\alpha} & J_{\varphi_1,\beta} \\ J_{\varphi_2,I_{dc1}} & J_{\varphi_2,I_{dc2}} & J_{\varphi_2,V_1} & J_{\varphi_2,V_2} & J_{\varphi_2,\varphi_1} & J_{\varphi_2,\varphi_2} & J_{\varphi_2,\alpha} & J_{\varphi_2,\beta} \\ J_{\alpha,I_{dc1}} & J_{\alpha,I_{dc2}} & J_{\alpha,V_1} & J_{\alpha,V_2} & J_{\alpha,\varphi_1} & J_{\alpha,\varphi_2} & J_{\alpha,\alpha} & J_{\alpha,\beta} \\ J_{\beta,I_{dc1}} & J_{\beta,I_{dc2}} & J_{\beta,V_1} & J_{\beta,V_2} & J_{\beta,\varphi_1} & J_{\beta,\varphi_2} & J_{\beta,\alpha} & J_{\beta,\beta} \end{bmatrix} \tag{8.16}$$

where, the subscripts in Eq. (8.16) represent derivatives with respect to the unknown parameters. Hence, to determine the allowable values of phase steps α and β as function of SNR and N, let us first look at the following simple calculation. Suppose that, we have a variable $q = \Psi^T \mathbf{U}$, which represents the difference between the phase steps α and β, then the variance of q is given by

$$\begin{aligned} E[|q-\hat{q}|^2] =& E[(q-\hat{q})(q-\hat{q})^T] \\ =& E[\mathbf{U}^T(\Psi-\hat{\Psi})(\Psi-\hat{\Psi})^T\mathbf{U}] \\ =& \mathbf{U}^T E[(\Psi-\hat{\Psi})(\Psi-\hat{\Psi})^T]\mathbf{U} \\ \geq& \mathbf{U}^T\mathbf{J}^{-1}\mathbf{U} \end{aligned} \tag{8.17}$$

The problem, therefore, narrows down to selecting a matrix $\mathbf{U}$ such that the minimum difference between α and β is computed. Since all the parameters are unknown, the matrix $\mathbf{U}$ is given by $\mathbf{U} = [0\ 0\ 0\ 0\ 0\ 0\ 1\ \ -1]^T$.

8.3.2 Results of CRB analysis

We now perform 500 Monte-Carlo simulations at each SNR and study the performance of the annihilation filter method in retrieving the difference of the phase steps at a pixel point. During the analysis the phases φ_1 and φ_2 are kept the same as described earlier in Eqs. (1.5a) and (1.5b), respectively. Additive white Gaussian noise having SNR between 0 and 70 dB is considered during the simulations. Our analysis consists of two parts.

During the first part, we determine the MSE of $\alpha-\beta$ as a function of the SNR and the difference between the phase steps α and β as percentage of α. During the analysis we choose $\alpha = \pi/6$ and vary the difference of α and β between 0 to 100% of α. Given the fixed value of α, this analysis indicates the reliable values of β which can be selected for a particular SNR and N. It is important to note that the value of α can be selected anywhere between 0 and π radians. However, to keep the analysis simple we have selected just one value of α in the present study. The allowable values of β can be determined by comparing the plot of MSE of $\alpha-\beta$, obtained using the annihilation filter method for 500 iterations at each SNR, with respect to the mean square error obtained from the CRB given by Eq. (8.17). The values in the plot where the MSE of $\alpha-\beta$, obtained from the annihilation filter method, goes below the MSE obtained using the CRB, are considered as prohibited for the selection of separation between the phase step values α and β. The test is carried out for data frames $N = 11$, 15, and 20. The study shows that separation between the phase steps can be reduced as the number of data frames increases. Moreover, the incorporation of denoising procedure substantially improves the allowable lower range of phase step separation. For instance, Fig. (8.5f) shows that for the separation between α and β as 70% of α, and for SNR 30 dB, the MSE is 0.01 rad^2 using the annihilation method.

In the second analysis, we perform 1000 simulations at a pixel to compare the bounds in the retrieval of phase steps α and β obtained using the annihilation filter method, with theoretical bounds obtained by the CRB for various phase step values in the presence of noise. Since the previous analysis showed that the denoising procedure is effective, the present study is performed with the incorporation of a denoising step and for $N = 20$. Figure (8.6) shows that as the separation between the phase steps α and β increases, their values can be reliably estimated at lower SNRs. Figures (8.6e)-(8.6f) show that as the separation between the phase steps increases the bounds obtained by annihilation filter method reaches the theoretical bounds given by the

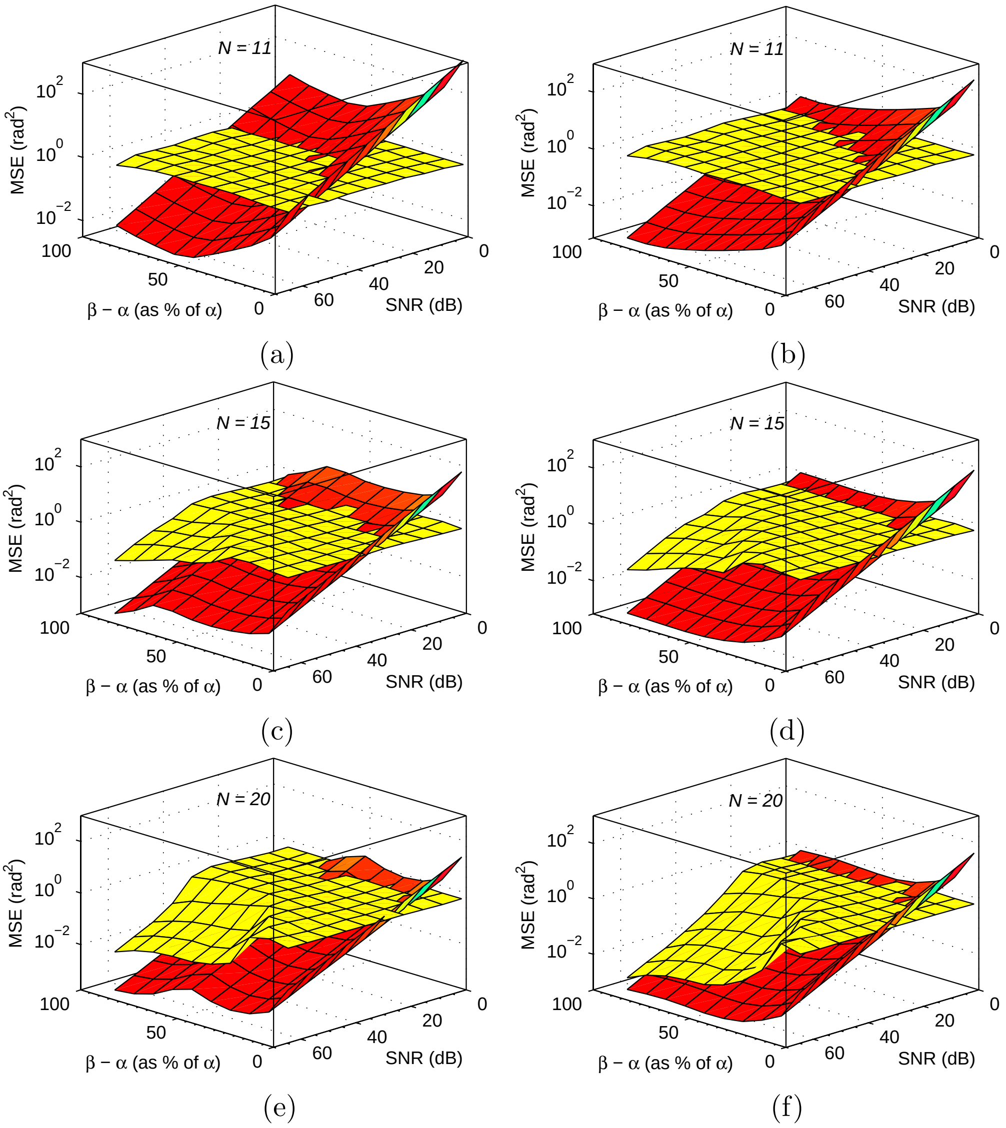

(a) (b) (c) (d) (e) (f)

Fig. 8.5: The plots show the MSE for $\alpha - \beta$ with respect to $\alpha - \beta$ as percentage of α, and SNR. The plots are shown for data frames $N = 11$, 15, and 20. The plots a, c, and e, are without the denoising procedure, while plots in b, d, and f are with the denoising step. In the plot the grey shade represents the Cramér-Rao lower bound while the white shade represents the MSE obtained using the annihilation filter method. MSE is represented in log scale.

CRB at much lower SNR as compared to that obtained in Figs. (8.6a)-(8.6d). This analysis once again reemphasizes the fact that larger the separation between the phase steps, more reliably is the phase obtained at lower SNRs. Similar analysis can also be performed for other algorithms.

8.4 Conclusion

To conclude, this chapter discussed three approaches namely, the traditional approach, the least-squares method, and the signal processing (annihilation filter method) approach in dual phase shifting interferometry. The traditional approach suggests that an additional processing

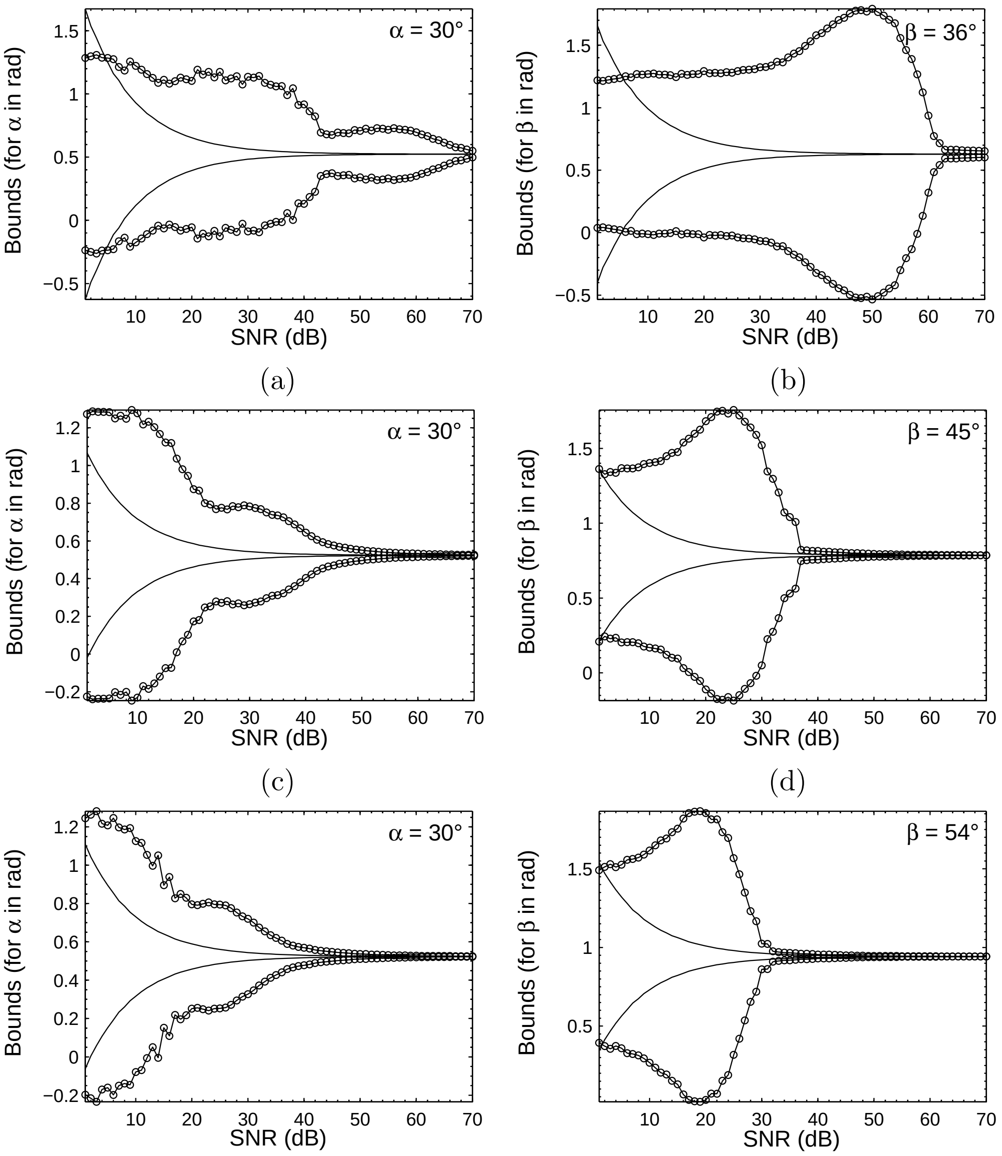

(a) (b)

(c) (d)

(e) (f)

Fig. 8.6: The plots show the bounds for retrieving the phase steps α and β for 0 to 70 dB SNR. The values of β in (b), (d), and (e) are selected as 1.2, 1.5, and 1.8 times of $\alpha = \pi/6$, respectively. The line with circle dots shows the error bounds obtained using the annihilation method while the simple line represents the bounds given by the CRB.

step needs to be incorporated to extract the wrapped phases. The study of the least squares fit and the signal processing approaches reveal that a proper choice of the pair of phase steps is of paramount importance. The analysis using Cramér-Rao bound can act as a guideline to select the optimal pair of phase steps in the presence of noise. We believe that a thorough understanding of the issues associated with each of these approaches will pave the way for automated simultaneous measurement of two components of displacement in holographic moiré.

Chapter 9

Statistical Study and Experimental Verification of High Resolution Methods in Phase Shifting Interferometry

Introduction of high resolution methods such as annihilation filter, state-space, Multiple Signal Classification (MUSIC), Minimum-Norm (min-norm), Estimation of Signal Parameter via Rotational Invariance (ESPRIT), and Maximum-Likelihood Estimator (MLE), have enabled the estimation of distribution of multiple phases in an interferogram by incorporating multiple piezoelectric transducers (PZT's), especially in holographic moiré. Typically, while using these methods, the first step involves estimating the phase steps pixel-wise, followed by computing the interference phase distribution by designing a Vandermonde system of equations. In this context, the present chapter presents a statistical study of these methods for the case of single and dual PZT's. The performance of these methods is also compared with other conventional bench-marking algorithms involving single PZT's. The chapter also discusses a significant issue of allowable pair of phase steps in the presence of noise using a robust statistical tool such as Cramér-Rao bound. Furthermore, experimental validations of these high resolution methods is presented for the estimation of single phase in holographic interferometry and for the estimation of multiple phases in holographic moiré.

9.1 Introduction

In phase shifting interferometry, the potential bottlenecks in obtaining accurate phase results of the order of $1/100^{\text{th}}$ of the wavelength are the various systematic and random errors influencing the measurement. Various attempts have been made to overcome these sources of errors through design of algorithms. [49, 139] Some of these conventional algorithms are well suited to minimize systematic errors such as those due to nonsinusoidal waveforms and PZT miscalibration. [61, 68] Nonsinusoidal waveform is a consequence of multiple reflections inside the laser cavity, detector nonlinearity, or the phase shifter itself. These algorithms however, advocate selection of certain fixed phase steps in order to minimize these sources of errors. Generalized phase shifting algorithms on the other hand offer the flexibility of using phase steps which could be chosen arbitrarily. [78, 79] These algorithms are however sensitive to nonsinusoidal waveforms.

Phase shifting algorithms based on high-resolution methods such as annihilation filter [1], state-space [115], Multiple Signal Classification (MUSIC) [121], Minimum-Norm (min-norm) [125], Estimation of Signal Parameter via Rotational Invariance (ESPRIT) [128], and maximum-likelihood estimator [134] have been proposed for the determination of phase **distributions**. These algorithms draw upon the complementary strengths of the conventional and generalized phase shifting algorithms. Moreover, the algorithms developed prior to the advent of phase shifting algorithms based on high-resolution methods tended to be also restricted as far as accommodating multiple PZT's in an optical setup was concerned.

These high-resolution methods are well known for estimating the frequencies present in the spectrum embedded in noise. These methods assume the noise to have normal distribution with zero mean and variance σ^2 in accordance to the central limit theorem. [74] Given the successful adaptation of these methods for estimating phase distribution in an interferogram, this chapter addresses an important aspect of studying the statistical behavior of these methods. The performance of these methods is analyzed by studying the mean-squared-error (MSE) in the estimation of phase step in the presence of noise, and the most robust of these methods is identified. Once the most robust method is identified, comparison is performed between the best high resolution method and the other bench marking algorithms for various levels of signal-to-noise ratio (SNR). Further study will focus on identifying the best phase steps while using this method in the presence of noise. The chapter further discusses the performance of high resolution methods in the estimation of multiple phases. In the case of the estimation of dual phases, a proper choice of the estimation method and the pair of phase steps is of utmost importance. We thus perform a similar study as carried out in the case of a single PZT by identifying the best method from the MSE plot for various magnitudes of noise and percentage separation between the phase steps α and β. Once the best method for dual PZT is identified, we discuss the important issue of selecting an allowable pair of phase steps in the presence of noise using the Cramér-Rao bound. Cramér-Rao bound gives an insight into the potential performance of the estimator. [136] Experimental results are shown to provide an insight on the feasibility of these methods for the estimation of single phase in holographic interferometry and multiple phases in holographic moiré. [100, 101]

9.2 Classification of Phase Shifting Algorithms

Conventional single PZT algorithms and our high-resolution methods can be broadly classified into three Groups, namely A (effective in minimizing the linear calibration error in PZT), B (effective in handling the harmonics), and C (effective in accommodating multiple PZT's) as shown in Table 1. A detailed comparison of the algorithms and methods in each Group for various cases will be presented in this chapter. The numbers in the parenthesis in Table 1. represent the references in which these algorithms appeared.

The first step involves comparing the Group C methods to identify the most efficient method of estimating the phase. Although Maximum-likelihood is an optimally efficient method in the presence of large number of data samples, this method will not be considered during the comparison because of its temporally inefficiency. Once the best method is identified, we compare the algorithms from Group A and B with this best identified method for various sources of errors. We further present the statistical study of the best identified method in Group C and also provide experimental validations supporting the study.

Tab. 9.1: Categorization of the conventional bench-marking phase shifting algorithms and high-resolution methods according to their characteristics.

	Calibration error (ε_1)	Harmonics (κ)	Multiple PZT's ($\mathbf{H}$)
	Group A	Group B	Group C
Carré [49]	✓	×	×
Hariharan [64]	✓	×	×
Schmit [140]	✓	✓	×
Larkin [68]	✓	✓	×
Surrel [60]	✓	✓	×
de Groot [141]	✓	✓	×
Annihilation filter [1]	✓	✓	✓
State-space [115]	✓	✓	✓
MUSIC [121]	✓	✓	✓
Min-norm [125]	✓	✓	✓
ESPRIT [128]	✓	✓	✓
Maximum-likelihood [134]	✓	✓	✓

9.3 Single PZT

9.3.1 Identification of an Efficient Method in Group C

One of the elegant approaches for identifying an efficient method is to compute the mean squared error (MSE) obtained during the estimation of phase step at a pixel in the presence of noise. For this, we consider additive white Gaussian noise between 0 and 70 dB. We assume $\kappa = 1$ and $\varphi = \pi/3$. The phase steps α are selected as $\pi/6$, $\pi/4$, $\pi/3$, and $\pi/2$. The data frames are selected as $N = 10$. We now perform 1000 Monte-Carlo simulations at each SNR and plot the MSE obtained during the estimation of the phase step α. The plots in Figs. (9.1a)- (9.1d) show the MSE versus SNR plot for different values of phase steps.

From the plots in Fig. (9.1), two significant observations can be made; first, among all the high-resolution methods ESPRIT performs better than the others, and second, as the phase step increases all the methods tend to have a similar performance. For instance, in Fig. (9.1d) we observe that for $\alpha = \pi/2$, all the methods exhibit the same MSE. This fact can also be verified experimentally in a holography interferometry setup. For smaller values of phase steps, the signal behaves as a correlated source and separating the phase steps is a difficult task with limited number of data frames. The method based on annihilation filter yields the phase steps directly from the signal data. For this method to work efficiently, the noise should be Gaussian. The other methods perform better than annihilation filter because based on the formulation of a covariance matrix they yield phase step from a more robust tool such as eigenvalue decomposition. At larger values of phase steps such as $\alpha = \pi/2$, the signal behaves as uncorrelated sources and separation of frequencies is a lot easier. In fact MUSIC is more accurate than ESPRIT if large number of data frames are present. But such a case is unrealistic in the case of phase shifting interferometry, where we are constrained to work with a limited number of data frames in order to minimize the influence of noise and errors originating from the PZT itself. Moreover, the fact which also needs to be taken into account is that in the case of a model mismatch ESPRIT performs better than MUSIC [142]. In several communication applications such as radar and sonar [123], the basic assumption is that the phase φ and the amplitudes a_k's and b_k's are random. This in turn gives rise to a covariance matrix which being identical in the least squares sense provides a more

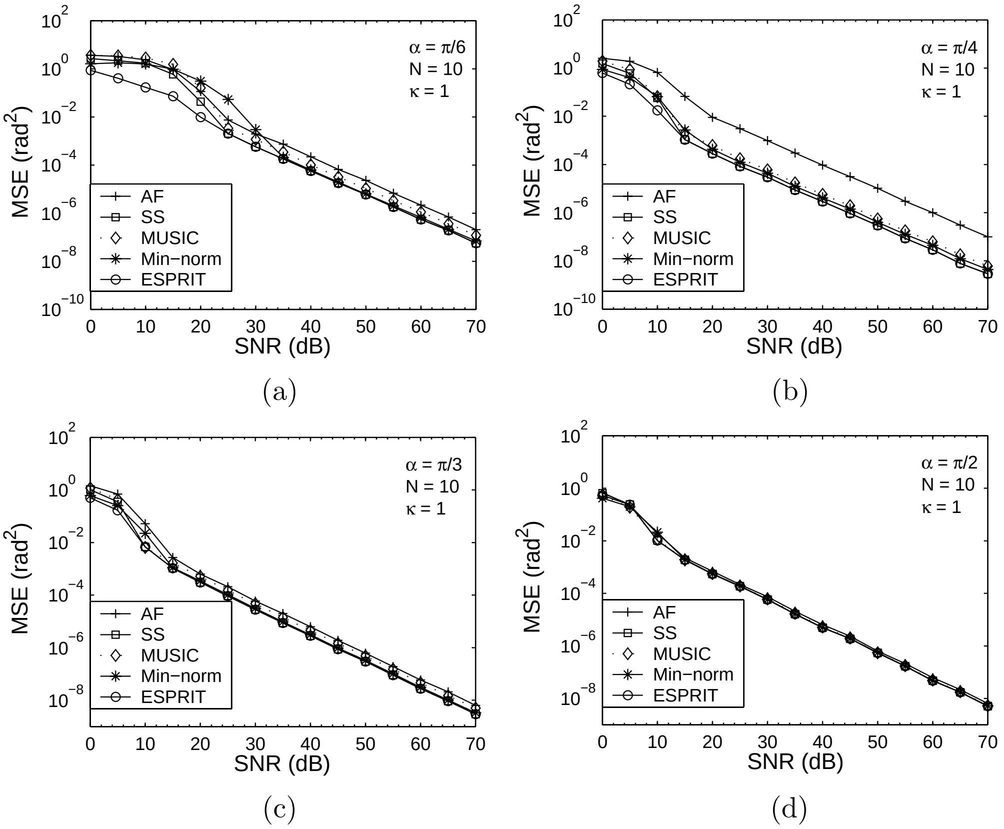

(a) (b)

(c) (d)

Fig. 9.1: The plots show the MSE for α with respect to SNR. In the legend ‘AF’ and ‘SS’ refer to annihilation filter and state-space method, respectively. MSE is represented in the log scale.

accurate estimation of phase steps. However, in the present application φ, a_k’s, and b_k’s are deterministic and hence a true covariance matrix cannot be achieved.

9.3.2 Experimental Verification of an Efficient Method in Group C

In the first case, the holographic fringes are captured on a 576 × 768 pixel CCD camera. About ten data frames are captured with phase steps of $\alpha = \pi/4$ between each data frame. Although the PZT has a nonlinear response to the applied voltage, a region corresponding to the linear response is selected. It is a well known fact [139] that the retrieved phase steps at each pixel are not constant because of noise and other errors, and hence studying the distribution of the retrieved phase steps can be one way to compute the value of the phase step. We thus plot a histogram to study the distribution of phase steps retrieved using our methods. Figures (9.2a) (9.2e) show the histograms for the phase steps obtained for $N = 10$ data frames. The histograms are drawn by dividing the phase steps between 0 and 180° into 1800 equal intervals or bins. The number of occurrence/frequency of each phase step is put in the corresponding bin. It can be observed clearly that with the exception of annihilation-filter method, all the other methods yield similar results. One of the elegant methods for identifying the phase steps and the nonlinear response of the PZT is proposed by Gutmann and Weber [139]. In this five-frame method, the frequency of occurrence of each combination of numerator, $M = I_5 - I_1$, and denominator $Z = 2(I_4 - I_2)$ in the phase step estimation is plotted by representing them by a gray level in a two dimensional diagram with M as the ordinate and Z as the abscissa. This way they form a Lattice-site rep-

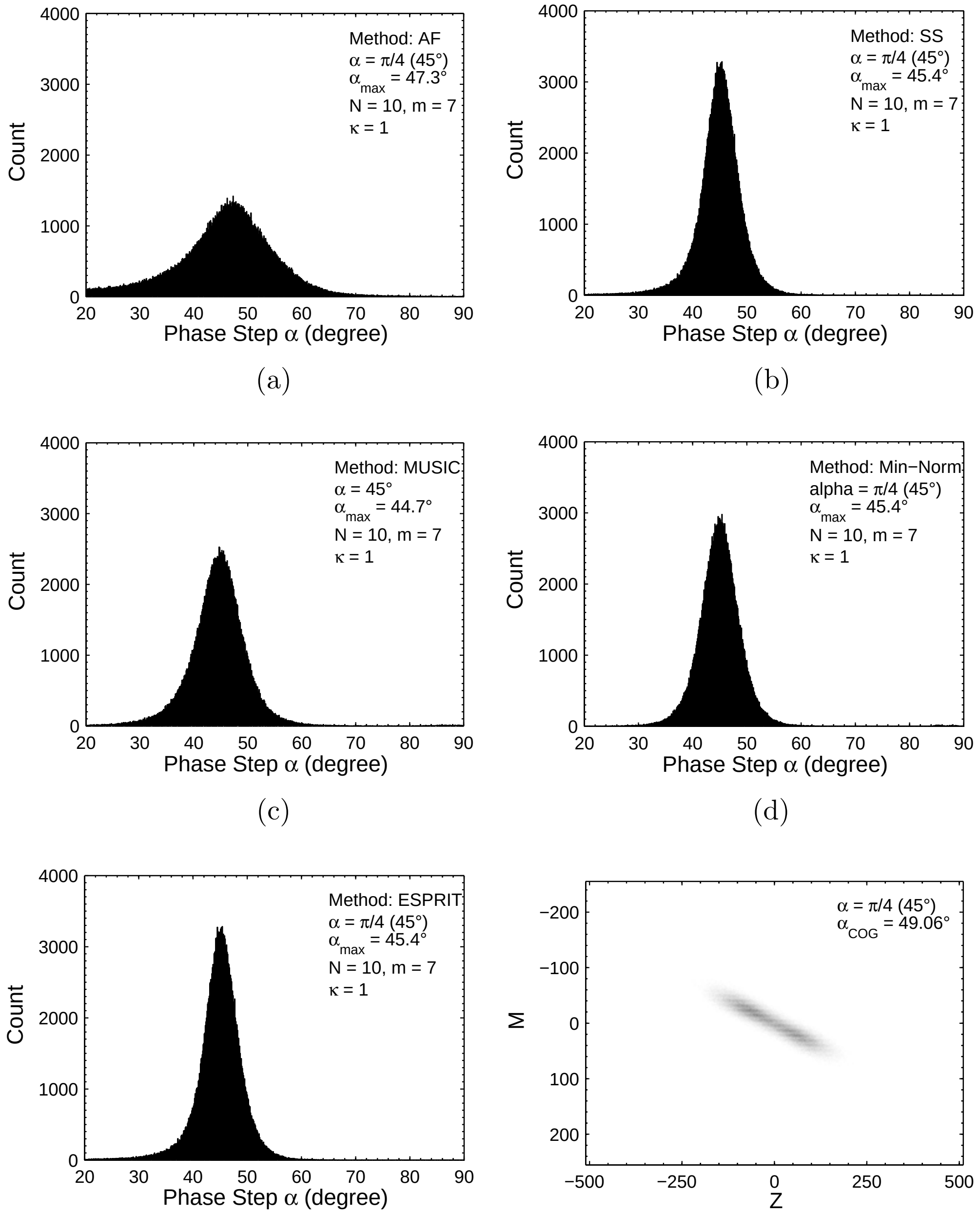

(a) (b) (c) (d) (e) (f)

Fig. 9.2: The histogram plot for phase step α for different methods. In the legend 'AF' and 'SS' refers to annihilation filter and state-space method, respectively.

resentation of the phase steps computed at each pixel on the data frame. If the phase steps are not equal then the lattice site curve will tend to form an ellipse or circle, which is a qualitative test for nonlinearity in the PZT response. In the presence of noise, the broadening of the lattice site can be observed. The phase step obtained using Gutmann and Weber method is shown in Fig. (9.2f). With only five data frames used by this method, large errors in the computation of phase step can be observed for a highly noisy data.

In the second case, the experiment is performed with phase steps of $\alpha = \pi/2$ between each data

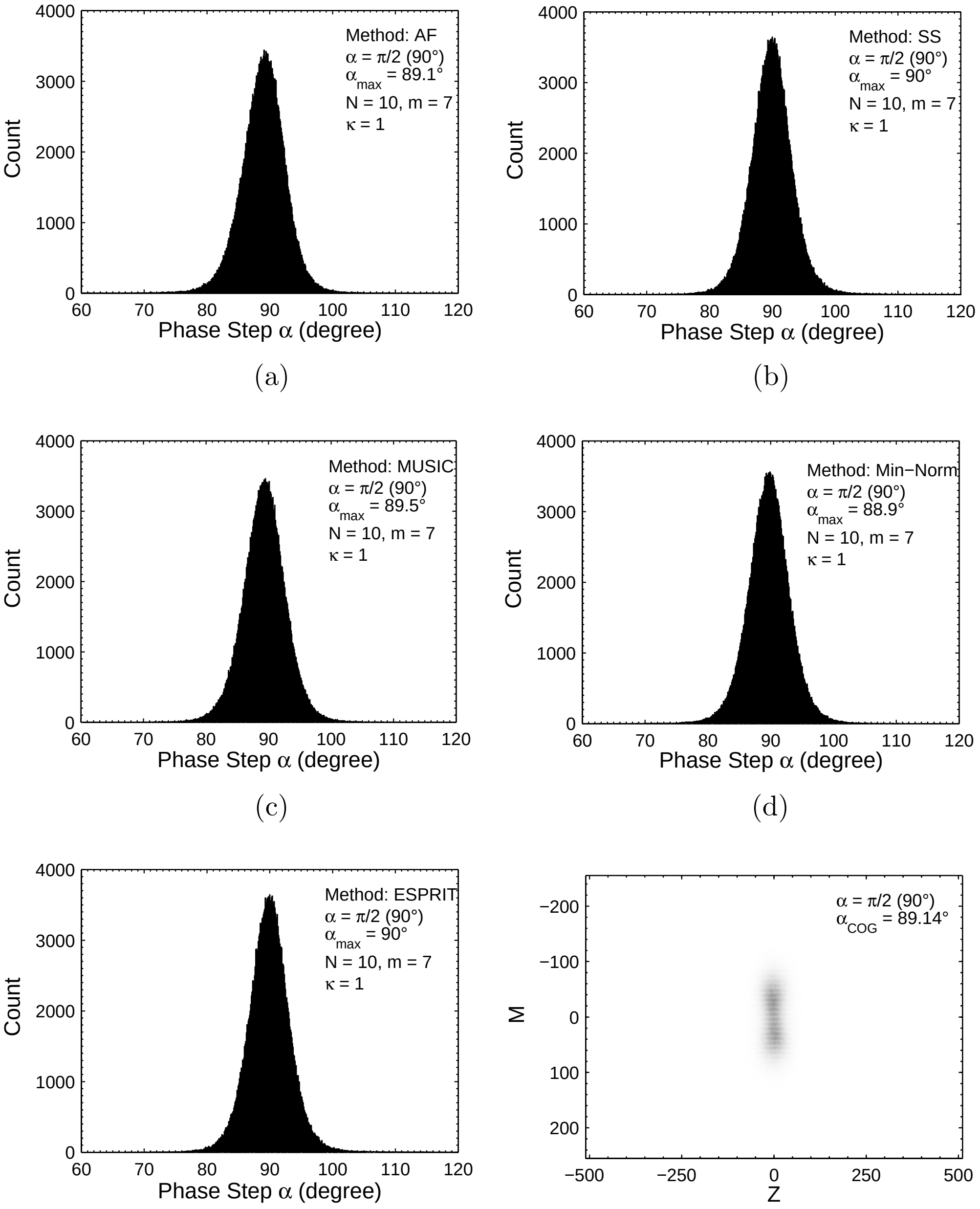

(a) (b)

(c) (d)

(e) (f)

Fig. 9.3: The histogram plot for phase step α with different methods. In the legend 'AF' and 'SS' refers to annihilation filter and state-space method, respectively.

frame. We again plot a histogram to study the distribution of phase steps retrieved using our methods in References [1, 119, 124, 127, 135]. Figures (9.3a)-(9.3e) shows the histogram for the phase steps obtained for $N = 10$ data frames. In this case, all the methods yield similar results. The results obtained using our methods are comparable to the one obtained using Gutmann and Weber [139] method. This is shown in Fig. (9.3f).

From these simulations and experimental verification, it is evident that the ESPRIT and the state-space approach almost perform similarly and are highly efficient. For further investigations, we will now concentrate on the ESPRIT.

9.4 Selection of Best Phase Step in ESPRIT

In the previous section we have identified ESPRIT to be the best performing method and hence, this section provides guideline for using this method in the presence of anticipated noise, data frames, and phase steps. The plots in Fig. (9.4) is obtained by computing the MSE in the estimation of phase step α for various values of phase steps and data frames at a particular SNR. For this, we perform 1000 Monte-Carlo simulations for each value of phase step and data frame. The plot clearly shows that as the SNR increases a broader range of phase step values can be used for the same data frame. For instance, the plot in Fig. (9.4f) shows that the allowable range of phase steps for $N = 8$ data frames and SNR=35 dB are from 10° to 170°, as compared to the allowable range of 40° and 120° for SNR=10dB as shown in Fig. (9.4a). The plot also reveals reduction in the MSE as the SNR increases. Thus for best results, we recommend a selection of phase steps between 30° and 160°, and the number of data frames between 8 to 10, since the SNR can be reasonably anticipated between 15 to 30dB in practical situations.

9.5 Comparison of Group B Algorithms and ESPRIT

This section presents a comparison of ESPRIT with other well known algorithms from Group B in Table 1. The algorithms proposed by Carré [49] and Hariharan [64] are not considered here as these algorithms are sensitive to higher order harmonics and, in addition, do not compensate for detector non-linearity. According to the central limit theorem, the noise occurring during phase measurement can be assumed to be Gaussian [74]. Hence, we perform 1000 Monte-Carlo simulations at each SNR, for values of SNR from 10 to 80 dB; and compute the MSE in the estimation of phase at an arbitrary pixel point. Usually, the phase step applied to the PZT can be considered as $\alpha^{'} = \alpha(1 + \varepsilon)$, where ε is the linear miscalibration error. Plots in Fig. (9.5a) show that for a zero calibration error in the phase step the ESPRIT, Surrel, Larkin, Schmit, and de Groot algorithms perform similarly. However, our method requires additional number of data frames to achieve the same performance as these algorithms. Unfortunately, there is always some magnitude of linear miscalibration error associated with the use of a PZT. Hence, we test the robustness of these algorithms and our method in the presence of linear miscalibration errors. Figures (9.5b)-(9.5d), show the plots for $\varepsilon = 1.0\%$, $\varepsilon = 3.0\%$, and $\varepsilon = 5.0\%$, respectively. The figures show that as the miscalibration error increases, there is a certain bias in the estimation of the MSE even with an increase in the SNR. However, ESPRIT shows a continuous decrease in the MSE with an increase in the SNR. An important point to note here is that with our method, the MSE can still be reduced further if additional number of data frames is used in the computation of phase. Moreover, these algorithms have been designed for particular phase step values and even a slight deviation from these values has been seen to result in a considerable error in phase computation.

9.5.1 Phase Extraction using ESPRIT

We present an example in this section in which the phase step is selected as $\alpha = \pi/3$ between the successive data frames in a holographic interferometry setup. Ten data frames are acquired with this selected phase step. Figure (9.6a) shows a typical fringe map obtained after deforming the object. The phase step obtained using ESPRIT is shown in Fig. (9.6b). The phase step is

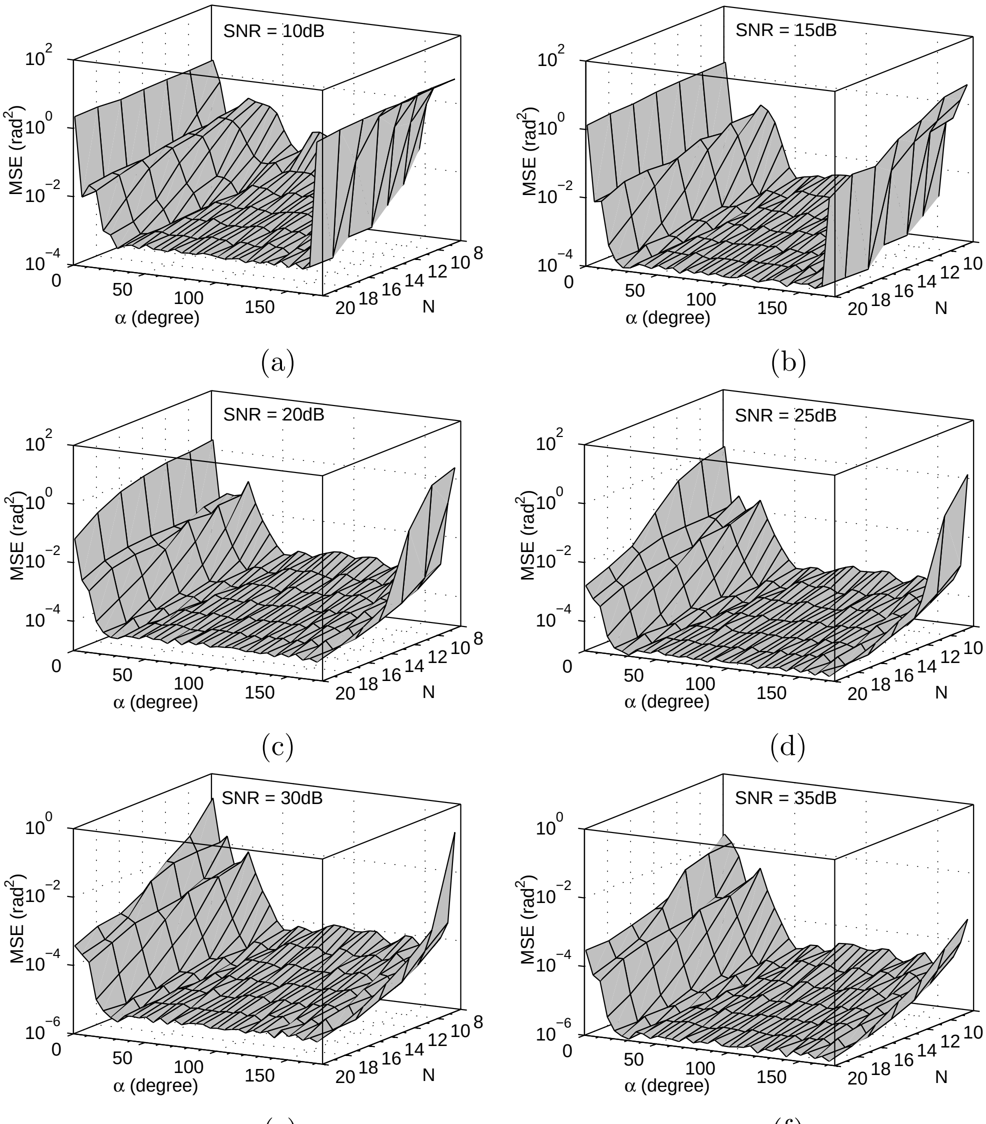

(a) (b)

(c) (d)

(e) (f)

Fig. 9.4: The plots show the MSE for α with respect to α and N for various SNR using ESPRIT.

reasonable estimated with 1.16% error. The phase step of 59.3° is considered while computing the phase distribution. Figures (9.6c) and (9.6d) show the wrapped and unwrapped phase maps. Note that median phase filtering has been applied to the wrapped phase map. The wrapped phase is obtained by designing a Vandermonde system of equations. [114, 137] The computational time for the estimation of wrapped phase is about 3 minutes on a desktop PC with a Pentium IV 3GHz processor and a 2 GB RAM.

9.6 Dual PZTs in Holographic Moiré

To the best of the author's knowledge none of the fixed phase steps algorithms in Table 1 have the ability to accommodate dual PZTs. On the other hand, high resolution methods seem to be well suited for applications including dual PZT's in an optical configuration. The high resolution based methods are also effective in minimizing the commonly occurring systematic

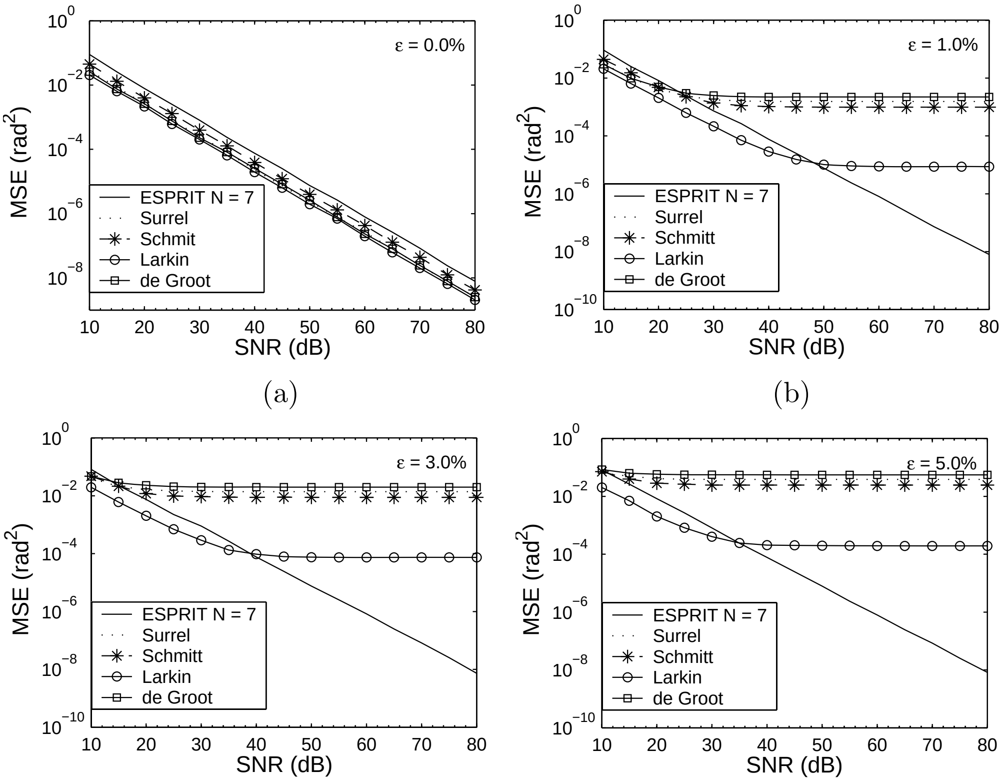

(a) (b)

(c) (d)

Fig. 9.5: Comparison of ESPRIT with respect to the algorithms developed by Surrel, Schmit, Larkin, and de Groot for the computation of phase for different values of linear miscalibration errors a) $\varepsilon = 0.0\%$, b) $\varepsilon = 1.0\%$, c) $\varepsilon = 1.0\%$, and d) $\varepsilon = 5.0\%$

and random errors during the measurement. We first proceed by identifying the best possible method among the five high resolution methods that we have proposed. Once the best method has been identified we will study the conditions on the selection of the pair of phase steps that can be applied to dual PZT's. In the presence of a low signal-to-noise ratio (SNR), a careful selection of the pair of phase steps with limited number of data frames is necessary. Since, noise plays an important role in the successful implementation of the concept, a sound knowledge of the allowable phase steps is of prime importance. Hence, there is a need to study the statistical characteristics of phase shifted holographic moiré (which is independent of the estimator itself) using Cramér-Rao bound. We further present an experimental investigation on retrieving the pair of phase steps for various percentages of separation between them in holographic moiré. Finally, we present the wrapped and unwrapped phase maps corresponding to phase distributions φ_1 and φ_2.

9.6.1 Selection of the Best Method for Dual PZTs

We perform a similar analysis as presented for single PZT for identifying an efficient method. However, note that unlike the previous case, we now have to consider the performance of each method for different values of phase steps α and β in Eq. 2.19. We thus compute the MSE in the estimation of individual phase steps at a pixel (n', j') in the presence of noise for different percentage of separation between the phase steps α and β. For this, we consider additive white

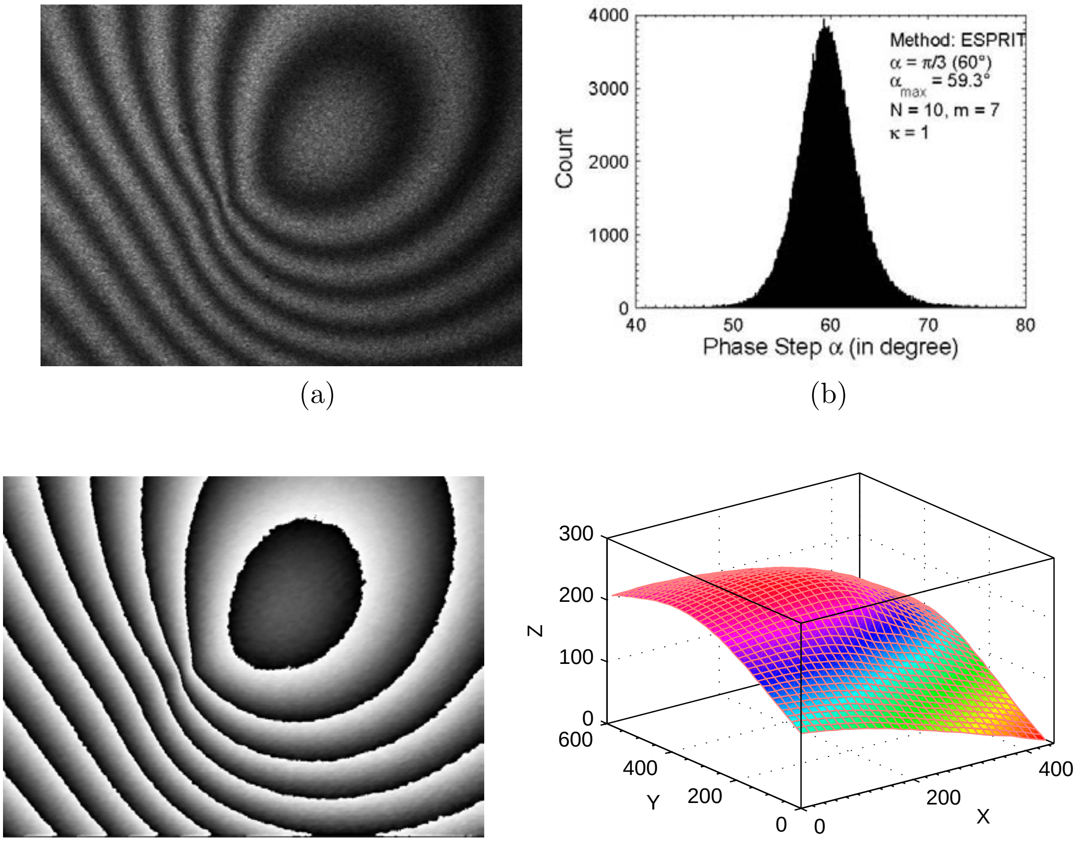

(a) (b)

(c) (d)

Fig. 9.6: a) Typical fringe map obtained in holographic interferometry; b) the histogram plot for phase step α; c) wrapped phase obtained using ESPRIT; and d) unwrapped phase map using Goldstein [3] algorithm.

Gaussian noise between 10 and 55 dB and perform 1000 Monte-Carlo simulations at each SNR. We assume $\kappa = 1$ and $\varphi = \pi/3$. The phase step α is selected as $5\pi/36(25^\circ)$. The values of $\beta - \alpha$ is selected as 10%(27.5°), 50%(37.5°), and 200%(75°) of α. We perform two different analysis for identifying the best method as regard to the lower MSE with data frames $N = 15$ and 35.

The plot in Figs. (9.7a)- (9.7b), Figs. (9.7e)- (9.7f), Figs. (9.7i)- (9.7j), Figs. (9.7m)- (9.7n), Figs. (9.7q)- (9.7r), and Figs. (9.7u)- (9.7v), show the MSE versus SNR plot for the percentage separation between α and β as 10%, 30%, 50%, 100%, 200%, and 300% corresponding to the values of $\alpha = 25^\circ$ and $\beta = 27.5^\circ, 32.5^\circ, 37.5^\circ, 50^\circ, 75^\circ$, and 100°, respectively for $N = 15$ data frames. While, the plots in Figs. (9.7c)-(9.7d), Figs. (9.7g)-(9.7h), Figs. (9.7k)-(9.7l) Figs. (9.7o)-(9.7p) Figs. (9.7s)-(9.7t) and Figs. (9.7w)-(9.7x) show the MSE versus SNR plot for the percentage separation between α and β as 10%, 30%, 50%, 100%, 200%, and 300% corresponding to the values of $\alpha = 25^\circ$ and $\beta = 27.5^\circ$, 32.5°, 37.5°, 50°, 75°, and 100°, respectively for $N = 35$ data frames. From the plots in Fig. (9.7), two significant observations can be made; first, among all the high-resolution methods ESPRIT still performs better than the others, and second, as the percentage separation between α and β increases all the methods start performing the same. From the plot it can also be observed that with the increase in the number of data frames, slightly lower separation between the phase step values is also possible. For instance, if we study the plots in Figs. (9.7e)-(9.7f) and Figs. (9.7g)-(9.7h), a remarkable improvement in the estimation of phase steps can be seen. Of all the methods, annihilation filter seems to be the most sensitive to the percentage of separation between the phase steps. The point which again needs to be emphasized here is that acquiring $N = 35$ data frames is not an attractive solution as with an increase in the acquisition time, the measurement process becomes more susceptible to error sources. Moreover, acquiring large number of data frames also adds to the computational cost. Hence, we suggest acquiring atleast $N = 18$ data frames and setting the value of $\beta - \alpha$ atleast 100% of α. In the following Section, we will we will corroborate this conclusion with robust statistical tools such as Cramér-Rao bound.

9.7 Cramér-Rao Bound Analysis for Holographic Moiré

From the analysis in the previous section, we can conclude that ESPRIT is the best method among al these high resolution methods given that the percentage separation between the phase steps is not high. This section provides further guidelines to optimizing the selection of pair of phase step values. We will first derive the CRB for holographic moiré. The CRB provides valuable information on the potential performance of the estimators. The CRBs are independent of the estimation procedure and the precision of the estimators cannot surpass the CRBs. In this context, we will first derive the CRB for the phase steps α and β as a function of SNR and N. Although the phase steps α and β can take arbitrary values for pure intensity signal, the central question is: what is the smallest difference between the phase steps α and β that can be retrieved reliably by an estimator as a function of SNR and N? Hence, we need to determine all the allowable values of phase steps α and β at a particular SNR and N.

The reason why we are interested in computing the smallest phase step difference is to provide an experimentalist with a guideline for the phase steps which he must select at a particular SNR and N, in order for him to estimate the phases φ_1 and φ_2 reliably. Suppose that the two phase steps are chosen inadvertently very close to one another and the measurements are performed at a low value of SNR. In such a case, the phases φ_1 and φ_2 cannot be estimated reliably. However, for the same value of the SNR, if the two phase steps α and β are far apart, the phase values φ_1 and φ_2 can be estimated reasonably accurately.

We thus derive the MSE for difference in phase steps $\alpha - \beta$ as a function of SNR and a percentage separation between the phase steps α and β, which will indicate the theoretical Cramér-Rao lower bound to the MSE. The Cramér-Rao bound can then be compared with the MSE obtained by any estimator (in the present case we will study the ESPRIT method). For this, we perform 1000 Monte-Carlo simulations at each SNR and the separation between the phase steps α and β is varied from 1% to 250% of α.

Two scenarios are possible. First, the MSE obtained from the estimator is below the CRB. We attribute this observation to the non-reliability in the estimated phase steps and discard those values of separation between α and β in which the MSE is below the CRB. Second, the MSE of the estimator is above the CRB. In such a case, we infer that closer the MSE of the estimator is to the CRB, the more efficient is the estimator. The following section describes in brief the derivation for CRB.

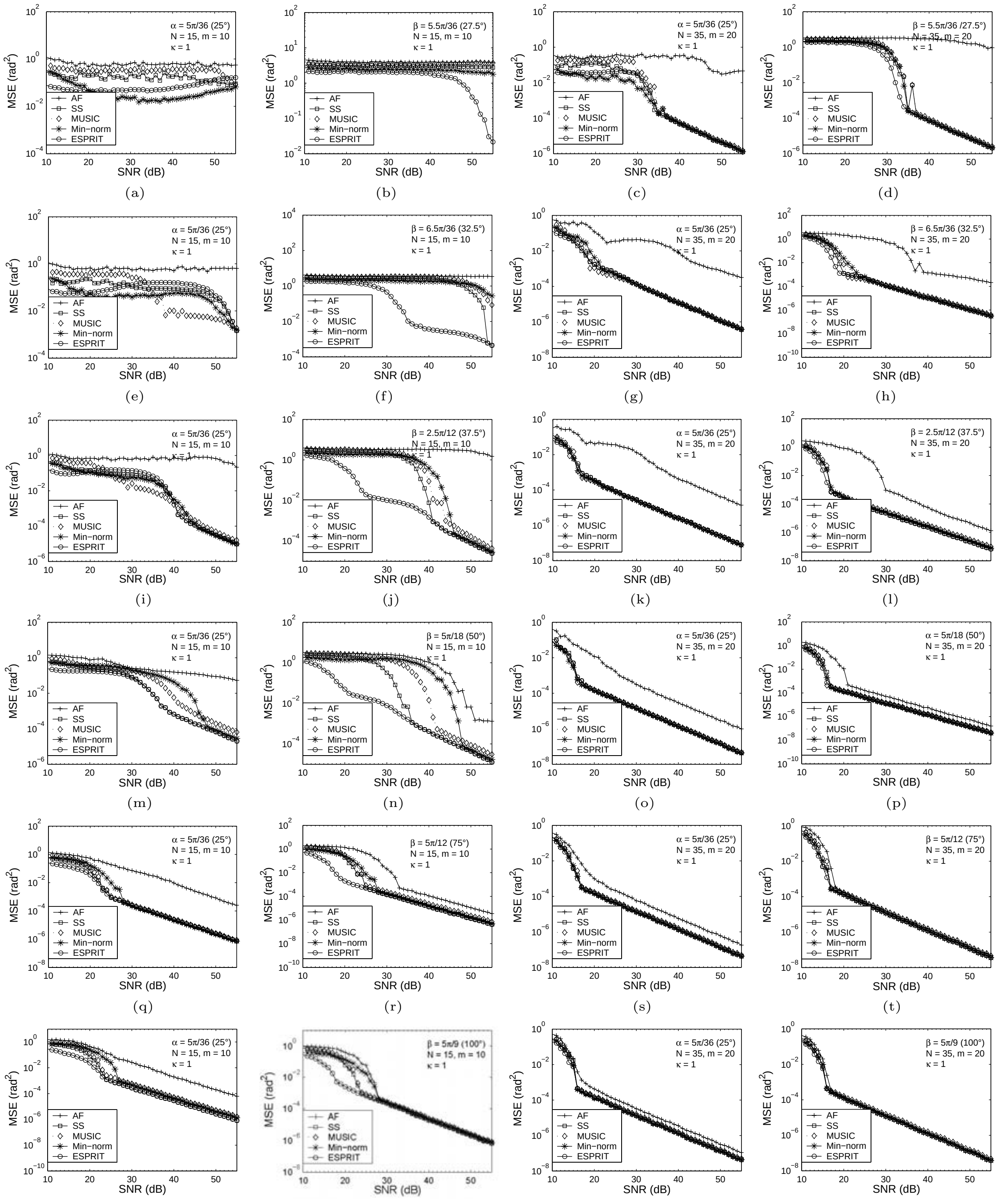

(a) (b) (c) (d)

(e) (f) (g) (h)

(i) (j) (k) (l)

(m) (n) (o) (p)

(q) (r) (s) (t)

(u) (v) (w) (x)

Fig. 9.7: The plots show the MSE in the estimation of phase steps α and β for various percentage of separation and data frames. In the figure, plots (a), (b), (e), (f), (i), (j), (m), (n), (q), (r), (u), and (v) correspond to $N = 15$, while plots (c), (d), (g), (h), (k), (l), (o), (p), (s), (t), (w), and (x) correspond to $N = 35$

9.7.1 Results of the CRB Analysis

MSE Estimation for the Best Dual Phase Step

We now perform 1000 Monte-Carlo simulations at each SNR and study the performance of the ESPRIT in retrieving the difference of the phase steps at a pixel point. During the analysis the phases φ_1 and φ_2 are selected as $\pi/4$ and $\pi/3.5$, respectively. Additive white Gaussian noise having SNR between 0 and 45 dB is considered during the simulations. We perform two different **analyses** as follows.

During the first part, we determine the MSE of $\alpha - \beta$ as a function of the SNR and the difference between the phase steps α and β as percentage of α. During the analysis we choose $\alpha = 5\pi/36$ and vary the difference of α and β between 0 to 250% of α. Given the fixed value of α, this analysis indicates the reliable values of β which can be selected for a particular SNR and N. It is important to note that the value of α can be selected anywhere between 0 and π radians. However, to keep the analysis simple we have selected just one value of α in the present study. The allowable values of β can be determined by comparing the plot of MSE of $\alpha - \beta$, obtained using ESPRIT for 1000 iterations at each SNR, with respect to the mean square error obtained from the CRB given by Eq. (8.17). The values in the plot for which the MSE of $\alpha - \beta$, obtained from the ESPRIT goes below the MSE obtained using the CRB, are considered as prohibited for the selection of separation between the phase step values α and β. The test is carried out for data frames $N = 10$, 15, 20, and 25. The study shows that the separation between the phase steps can be reduced with the increase in the number of data frames. The analysis also shows that for $N = 15$ onwards and for large percentage separation between the phase steps (150% in Fig. (9.8b)), ESPRIT seems to be optimally efficient as it attains a theoretical CRB for SNR greater than 30dB. As the number of data frames increase, for instance $N = 20$ (Fig. (9.8c)) and $N = 25$ (Fig. (9.8d)), ESPRIT is optimally efficient for 125% (SNR$\geq$25dB) and 75% (SNR$\geq$20dB) separation of α, respectively.

Estimation of the Theoretical Bounds for the Best Dual Phase Step

In the second analysis, we perform 1000 simulations at a pixel to compare the bounds in the retrieval of phase steps α and β obtained using ESPRIT, with the theoretical bounds obtained by the CRB for various phase step values in the presence of noise. The objective here is to show the importance of percentage separation between the phase steps and the influence of the number of data frames in attaining the theoretical CRB. Figures (9.9b) and (9.9d) show that as the separation between the phase steps α and β increases, their values can be reliably estimated at lower SNRs. What is more interesting to note here is that as the number of data frames increases, for the same percentage separation between the phase steps, the theoretical CRB can be attained at much lower SNRs. For instance, in Fig. (9.9d) the CRB is achieved at SNR=20dB while in Fig. (9.9f) the CRB is attained at SNR=15dB. In the plots in Fig. (9.9), the dotted lines show the upper and lower bounds in the estimation of phase steps using ESPRIT, while simple lines show the upper and lower bounds on the CRB. The point which needs to be emphasized is that when the estimated bounds for phase step values are within the CRB bounds, then the phase steps obtained cannot be relied upon at a particular SNR using the proposed estimator. This analysis reemphasizes the fact that larger is the separation between the phase steps and more are the number of data frames acquired, the more reliably would the phase be obtained at lower SNRs.

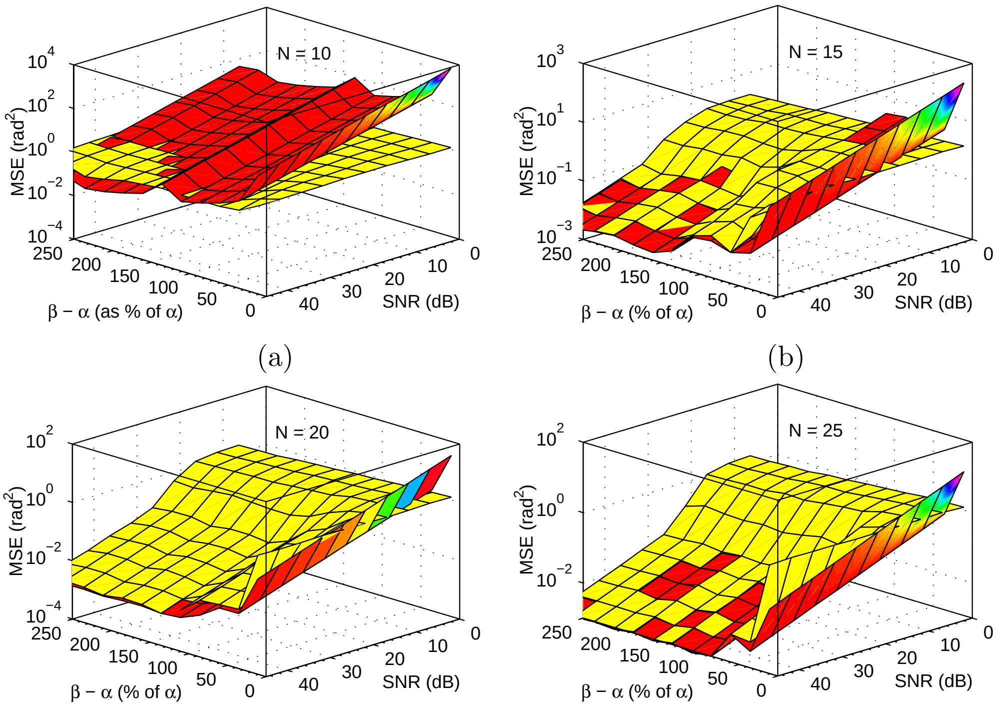

(a) (b)

(c) (d)

Fig. 9.8: The plots show the MSE for $\beta - \alpha$, with respect to $\beta - \alpha$ as a percentage of α, and with respect to the SNR. The plots are shown for data frames $N = 10$, 15, 20, and 25. In the plot the grey shade represents the Cramér-Rao lower bound while the white shade represents the MSE obtained using ESPRIT. MSE is represented in the log scale.

Experimental Verification of the Statistical Study

In this section, we study experimentally the influence of the phase step separation and of the number of data frames on retrieving the phase steps values. For this, we implement a holographic moiré set up as explained in Reference 24. The light from the laser source (He-Ne operating at 532nm wavelength) is split into two beams, namely the object beam OB, and the reference beam, RB. The reference beam falls directly on the holographic plate. The object beam, is split into two beams namely OB1 and OB2. The piezoelectric devices are placed in the path of the object beams. The OB1 and RB thus form one holographic interferometry system while OB2 and RB form the other interferometry system. Holographic moiré is an incoherent superposition of two holographic interferometry systems. The intensities of the object beams OB1 and OB2 are adjusted in such a way that equal scattered intensities from the object falls on the holographic plate. In the present experiment the object beam intensities falling on the holographic plates are 1.4 μw (OB1=OB2=0.7μw). The reference beam intensity is 9 μw. The exposure time for the holographic plate is selected as 3.5 seconds. The holographic plate after exposing for 3.5 seconds is developed using wet chemical process and placed accurately in its original position.

We now impart two displacements, i.e. out-of-plane and in-plane displacements to the object under study. A series of moiré fringe pattern is acquired while the phase steps are applied simultaneously to the two PZTs placed in the two arms of the optical system. The question central to applying the phase steps concerns the choice of the phase step values that should be applied in order to obtain reliable results. The analysis in the previous section showed that

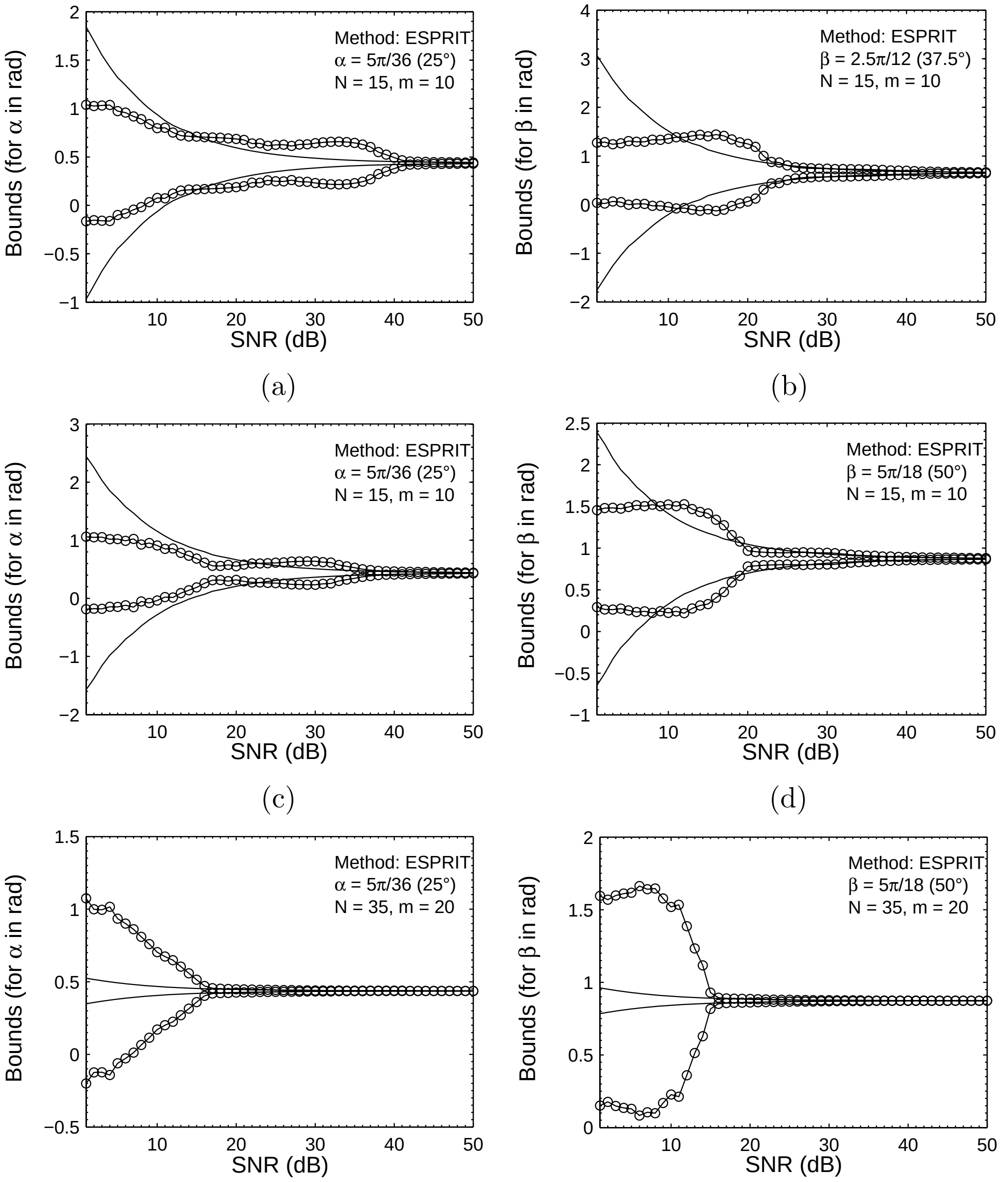

(a) (b)

(c) (d)

(e) (f)

Fig. 9.9: The plots show the bounds for retrieving the phase steps α and β for SNR= 0 to 50 dB. The values of β in (b), (d), and (f) are selected as 1.5, 2 , and 2 ($N = 35$ in this case) times of $\alpha = 5\pi/36$, respectively. The line with circle dots shows the error bounds obtained using ESPRIT while the simple line represents the bounds given by the CRB.

larger is the separation between the phase steps, the better is the reliability in the estimation of the phase steps. Once these phase steps have been estimated, we apply the Vandermonde system of equations for obtaining the phase information.

We thus select nine different pairs of phase steps $(\alpha, \beta) = [(45°, 60°), (30°, 45°), (25°, 45°), (30°, 60°), (45°, 90°), (25°, 60°), (30°, 90°), (25°, 90°), (20°, 90°)]$, corresponding to the percentage separation between α and β as 33%, 50%, 80%, 100%, 100% (note the selection of different pair of phase steps for the same percentage separation), 140%, 200%, 260%, and 350%, respectively. We

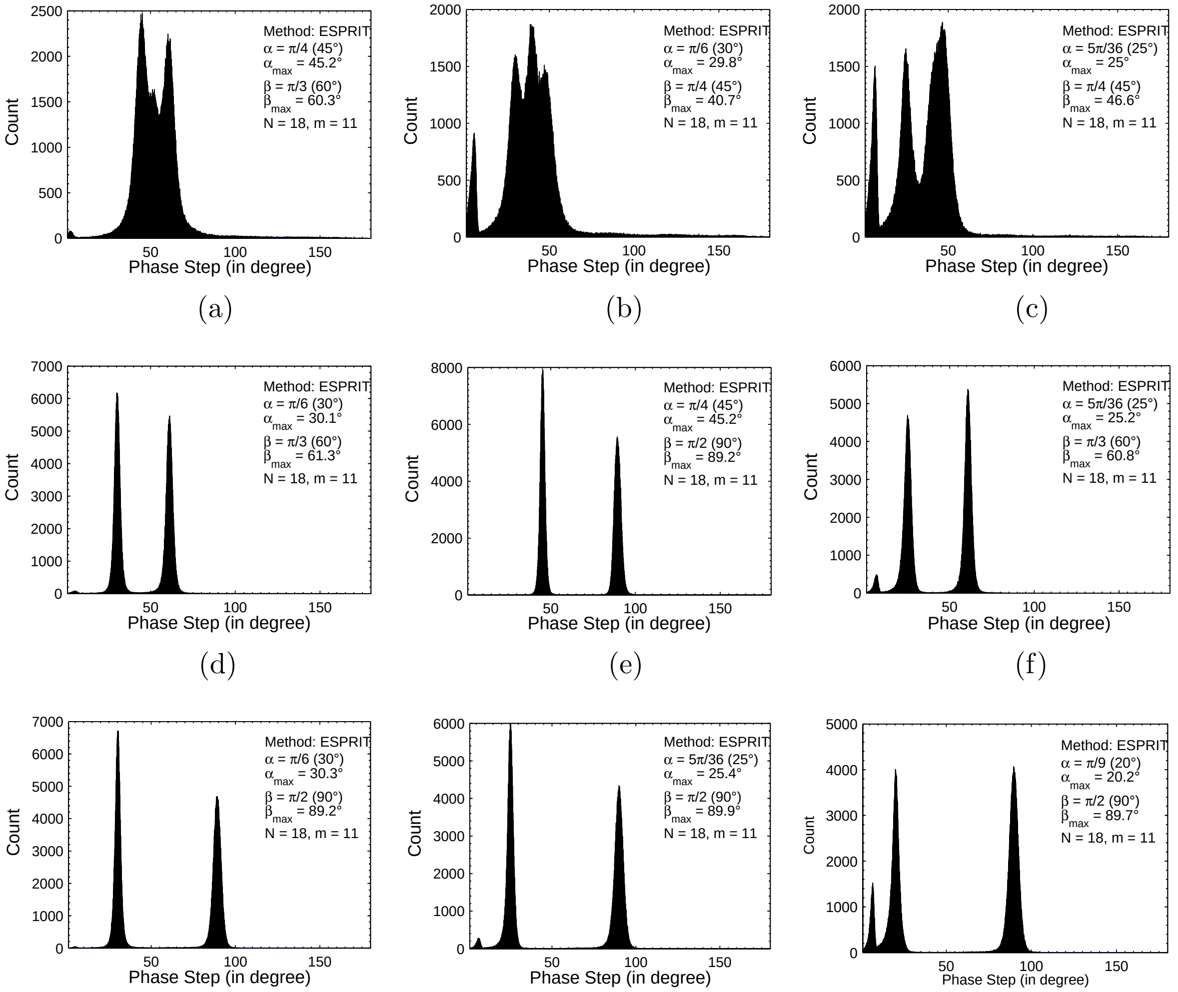

(a) (b) (c)

(d) (e) (f)

(g) (h) (i)

Fig. 9.10: The histogram plot for phase steps α and β obtained experimentally in holographic moiré using ESPRIT for $N = 18$ data frames

perform two different analysis corresponding to $N = 18$ and $N = 20$.

In the first case, i.e. for $N = 18$, we observe that for smaller separation between the phase step values, as shown in Figs. (9.10a)-(9.10c) the phase steps cannot be estimated reliably. The plots in Fig. (9.10) have been drawn based on the same process as mentioned earlier for the histogram plot in Figs. (9.2) and (9.3). The plots in Figs. (9.10d)-(9.10i) suggest the importance of larger separation between the phase steps. In the second case, we increase the number of data frames to $N = 20$. We observe substantial improvement in estimating the phase step values in Figs. (9.11a)-(9.11c) as compared to that in Figs. (9.10a)-(9.10c), respectively. One must note that the shape of the distribution becomes thinner as the number of data frames increases. This fact can be observed clearly by establishing a correspondence between Figs. (9.10d)-(9.10i) and Figs. (9.11d)-(9.11i), respectively. Hence, an increase in the number of data frames has a substantial bearing on the estimation of the phase steps. However, care should be taken that the PZT operates in a linear region to avoid the influence of the nonlinear response of the PZT movement.

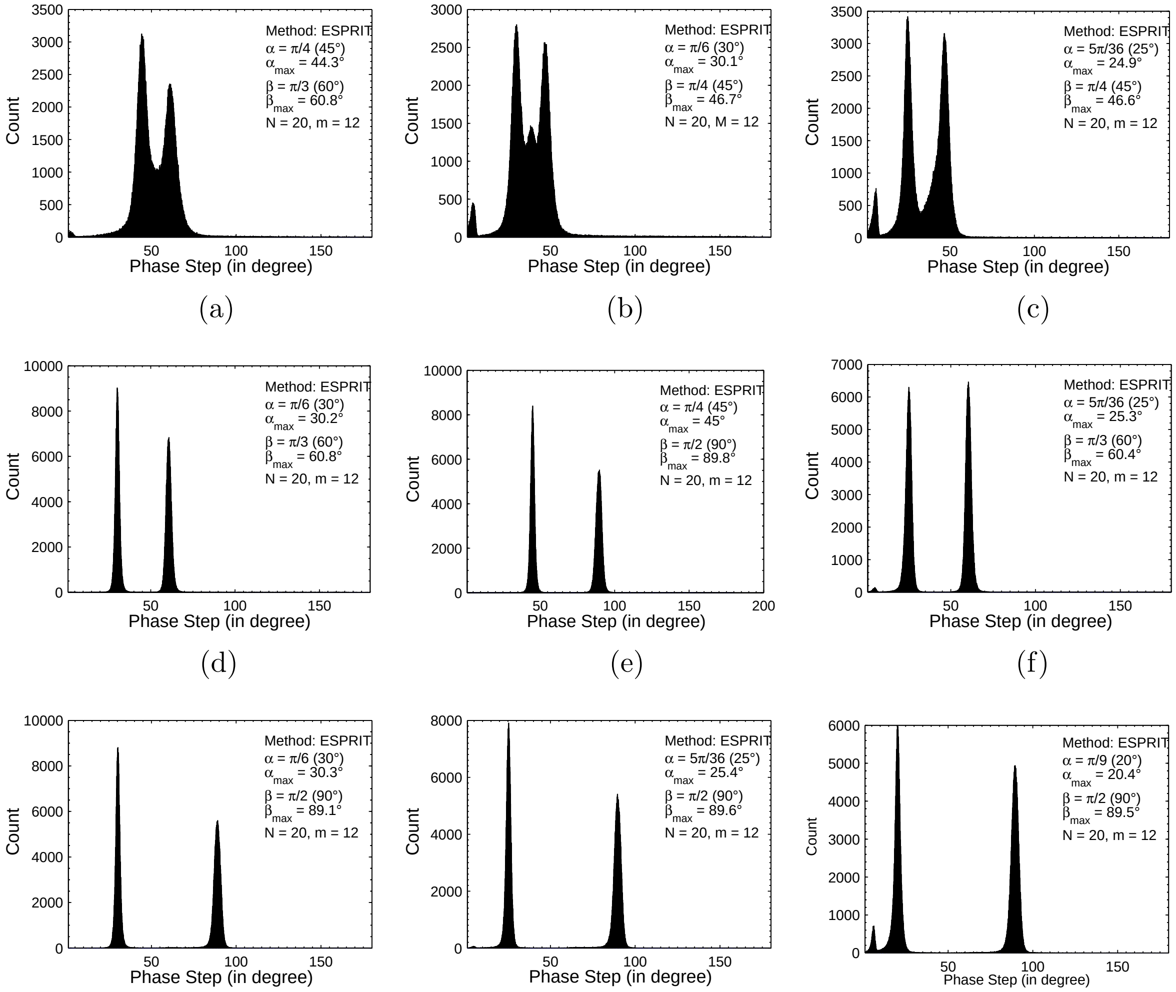

(a) (b) (c)

(d) (e) (f)

(g) (h) (i)

Fig. 9.11: The histogram plot for phase steps α and β obtained experimentally in holographic moiré using ESPRIT for $N = 20$ data frames

Figure (9.12a) shows a typical moiré fringe pattern obtained experimentally. The fringe patterns corresponding to the two interferometer systems are shown in Figs. (9.12b)-(9.12c). The phase steps obtained in Fig. (9.11h) (i.e. $\alpha = 25.4°$ and $\beta = 89.6°$) are used in the Vandermonde system of equations to compute the phase distributions φ_1 and φ_2. The wrapped phase maps corresponding to Figs. (9.12b)-(9.12c) are shown in Figs. (9.13a)-(9.13b), respectively, while the corresponding unwrapped phase maps are shown in Figs. (9.13c)-(9.13d), respectively.

9.8 Conclusions

To conclude, the present chapter presents a statistical study of high resolution methods in phase shifting interferometry for the estimation of single and multiple phase information. Through this chapter an attempt has been made to substantiate the simulation results with experiments. The chapter compares various bench marking algorithms with high resolution based methods. Experimental results show the feasibility of the high resolution methods. The following points

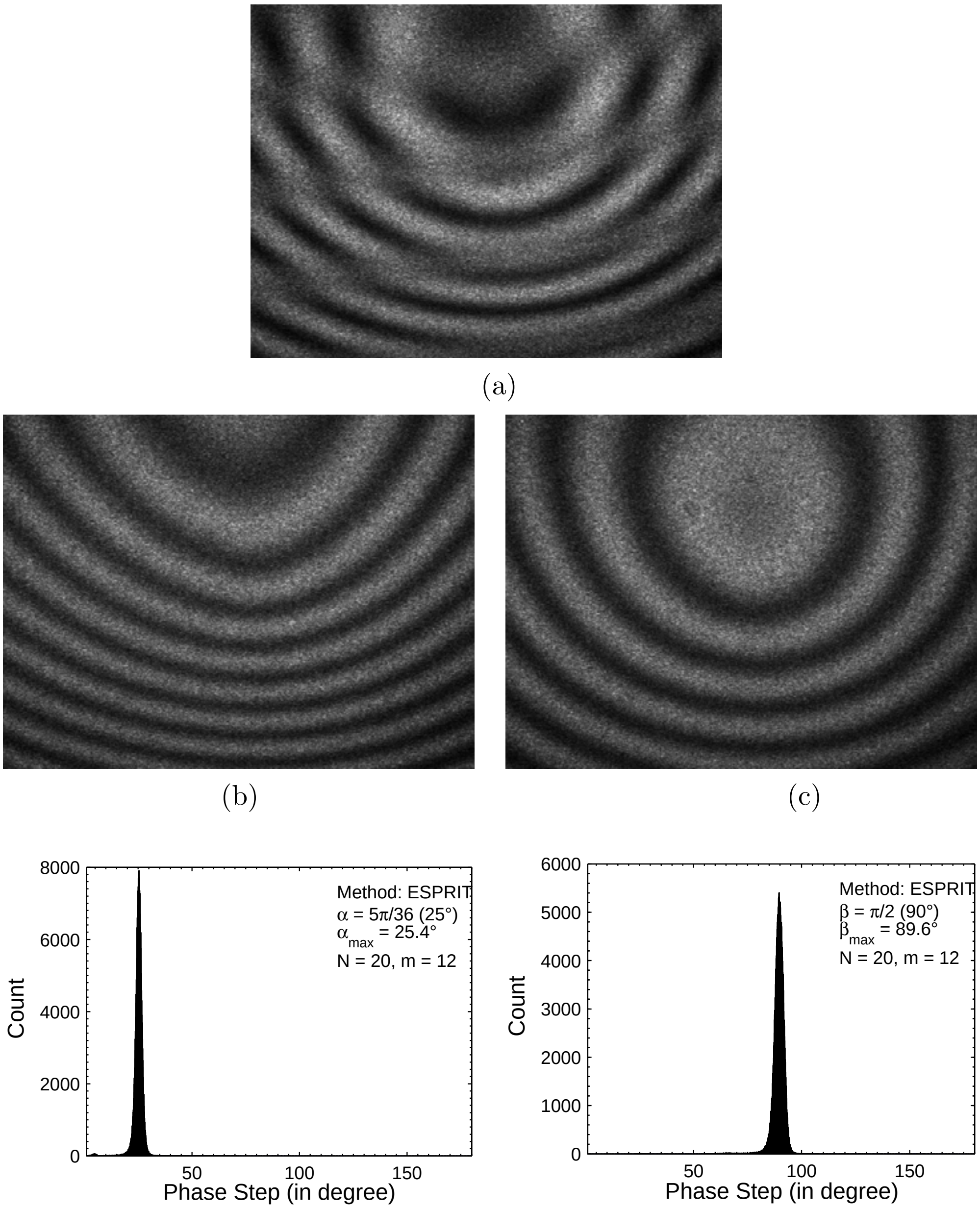

(a)

(b) (c)

(d) (e)

Fig. 9.12: a)A typical moiré fringe pattern in an experimental setup. b) and c) are the corresponding fringe maps in the two arms of the interferometer obtained after the out-of-plane and in-plane displacements have been given to the object

need to be mentioned regarding these methods

- In case of high resolution methods, ESPRIT based on rotational invariance property of the signal subspace performs better than the other methods. However, for higher phase step values (i.e. $\alpha \geq 60°$) all the methods perform almost the same statistically.
- In the case of both single PZT and dual phase shifting devices, the study reveals that an increase in the number of data frames yields better phase values. Although these methods

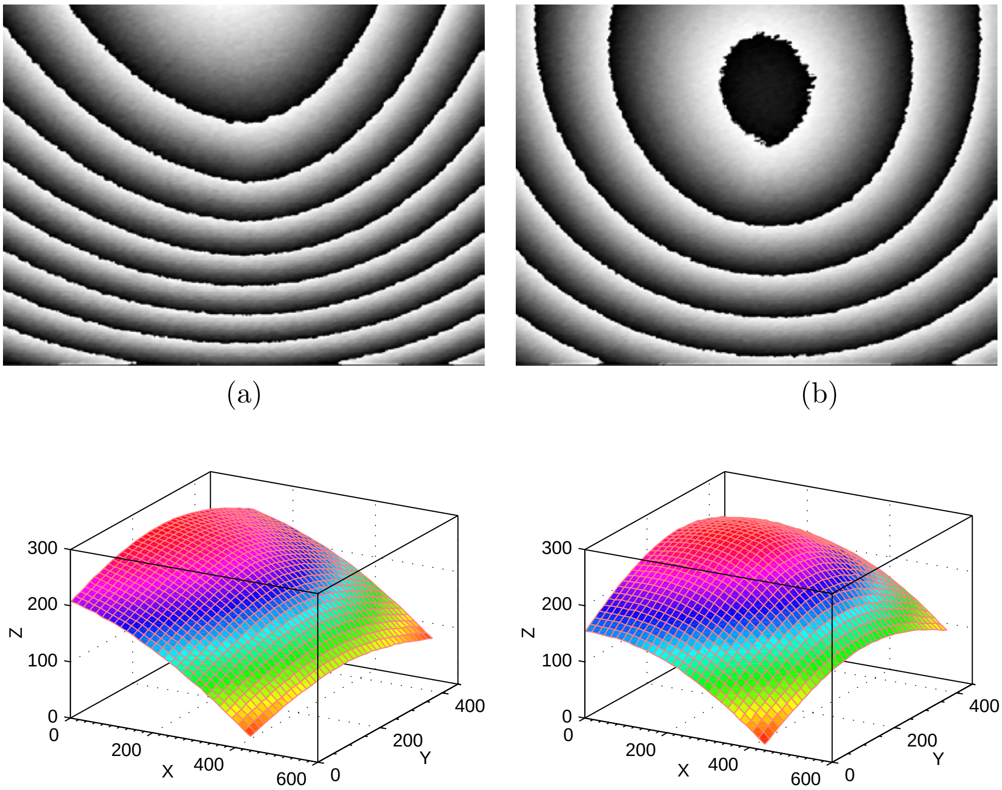

(a) (b)

(c) (d)

Fig. 9.13: Wrapped phase distributions corresponding to phase a) φ_1 b) φ_2. Unwrapped phase maps corresponding to wrapped phase c) φ_1 and d) φ_2.

estimate the phase step values pixel-wise, we suggest using a histogram approach so that a single phase step value obtained from a bin corresponding to the highest count can be used for the entire data frame in order to minimize the influence of various error sources.

- In the case of a single PZT, the ideal phase steps are between 30° and 160° and the number of data frames between 8 to 10 are sufficient. In the case of dual PZTs, the percentage separation between α and β greater than 100% should yield phase step estimates reliably for $N \geq 18$.
- Although not considered in the present chapter, attention should be first given to identifying the harmonic content of the recorded intensity waveform. This can typically be ascertained using robust signal processing tools such as singular value decomposition of the covariance matrix. Once the number of harmonics is known, a suitable Vandermonde system of equation can be designed for the estimation of phase information.
- For these methods to work efficiently, care should be taken to operate the PZT in the linear region. The nonlinear response can, otherwise, introduce substantial errors in phase step estimation.

Chapter 10

Conclusions and Discussions

The research is primarily driven by the desire to design a flexible and efficient method which is capable of accommodating multiple PZTs in an optical configuration. Before the advent of high resolution methods in configurations involving dual PZTs, such as, the holographic moiré , only the value of one component corresponding to the difference of displacement carried on the moiré was quantified, whereas the information carried by the carrier was lost. The current research, has thus, significantly contributed in overcoming the limitations exhibited by the present crop of phase shifting algorithms by enabling the quantification of information carried by the moiré and the carrier simultaneously. This has, in addition, led to the automation of moiré fringe analysis.

The high resolution methods have not only allowed the use of multiple PZTs, but have also facilitated the use of spherical wavefronts and arbitrary phase steps. These methods are robust performers in the presence of noise and nonsinusoidal wavefronts. Simulation and experimental results prove the feasibility of the proposed methods for cases involving single and dual PZTs.

Each successive method presented through Chapters 2 to 7, represents a significant advancement in the estimation of phase. The method based on the design of an annihilation filter yields phase steps directly from the signal data and needs a denoising procedure. It is a well known fact that solving covariance of a signal data rather than the signal data yields better results, because of the efficient mathematical tools such as eigenvalue decomposition. Thus, we proposed a state-space approach in Chapter 3 in which the phase steps are estimated from a covariance of signal data. This method yields better result than the annihilation filter method. We also proposed a new denoising approach before using state-space approach for the estimation of phase. However, both these methods need a denoising procedure, which adds to the computational cost. To get rid of the denoising procedure, we introduced MUSIC method which works directly on the covariance of the data and yields the phase steps using noise subspace. We also introduced min-norm algorithm which allows the estimation of phase steps from noise subspace. The min-norm algorithm yields phase step estimates by using a single vector from the noise subspace as compared to the MUSIC method which uses the whole set of noise subspace for the phase step estimation. Hence, min-norm is computationally efficient. However, with limited number of data frames, the noise influencing the measurement may not be Gaussian. Thus, we proposed ESPRIT, which allows the measurement of phase steps from the signal subspace rather than the noise subspace. We also proposed an optimally efficient method base on maximum-likelihood estimation for the estimation of phase. However, this method is computationally exhaustive and is not realizable in practical situations.

The exhaustive statistical analysis presented in chapters 8 and 9 shows that a careful selection of methods and phase steps are pertinent for obtaining accurate results. The analysis suggests that ESPRIT is the best method among all the high resolution methods in the case of single as well as dual PZTs. We also recommend that in the case of a single PZT, the ideal phase steps should be between 30° and 160° and the number of data frames between 8 to 10 are sufficient. In the case of dual PZTs, the percentage separation between α and β greater than 100% should yield phase step estimates reliably for $N \geq 18$. We also suggest selecting the best phase step values by plotting the histogram of the retrieved phase step values pixel-wise.

Further research should focus on identifying new configurations where dual PZTs can be applied for obtaining multiple phase information. The research also needs to be focussed in a direction where there is a possibility of accommodating more than two PZTs. For instance, if four PZTs are used in an optical step up, there is a possibility of estimating the three displacement components simultaneously. However, it still remains to be seen if these methods can perform as efficiently as they could for the case of dual PZTs.

Appendix A

Derivation for a Covariance Matrix

Let us consider a signal

$$I(n) = I_{dc} + \sum_{k=1}^{\kappa} a_k \exp(jk\varphi)\exp(jk\alpha n) + \sum_{k=1}^{\kappa} a_k \exp(-jk\varphi)\exp(-jk\alpha n) + \eta(n) \tag{A.1}$$

Here, $\eta(n)$ represents white Gaussian noise. The covariance of a function $I(n)$ is defined as [116–118]

$$r(p) = E[I(n)I^*(n-p)] \tag{A.2}$$

For simplicity, let us consider $\kappa = 1$ and rewrite Eq. (A.1) as

$$I(n) = I_{dc} + a_1 \exp(j\varphi)\exp(j\alpha n) + a_1 \exp(-j\varphi)\exp(-j\alpha n) + \eta(n) \tag{A.3}$$

Note that $I^*(n) = I(n)$, since the intensity is a real quantity. Thus, let us write $I^*(n-p)$ for $\kappa = 1$ as

$$\begin{aligned} I^*(n-p) = & I_{dc} + a_1 \exp(j\varphi)\exp[j\alpha(n-p)] + \\ & a_1 \exp(-j\varphi)\exp[-j\alpha(n-p)] + \eta^*(n-p) \end{aligned} \tag{A.4}$$

Substituting Eqs. (A.3) and (A.4) into Eq. (A.2), we obtain the following

$$r(p) = E\left\{ \begin{array}{c} I_{dc}^2 + I_{dc}a_1 \exp(-j\varphi)\exp(-j\alpha n) + I_{dc}a_1 \exp(j\varphi)\exp(j\alpha n) \\ \exp(j\alpha p)[a_1^2 + I_{dc}a_1 \exp(-j\varphi)\exp(-j\alpha n) + a_1^2 \exp(-j2\varphi)\exp(-j2\alpha n)] \\ \exp(-j\alpha p)[a_1^2 + I_{dc}a_1 \exp(j\varphi)\exp(j\alpha n) + a_1^2 \exp(j2\varphi)\exp(j2\alpha n)] \\ +\eta(n)\eta^*(n-p) \end{array} \right\} \tag{A.5}$$

Equation (A.5) can be written in the following compact form

$$r(p) = E\left[I_{dc}^2 + c_1 + \exp(j\alpha p)(a_1^2 + c_2) + \exp(-j\alpha p)(a_1^2 + c_3) + \eta(n)\eta^*(n-p)\right] \tag{A.6}$$

where, $c_1 = I_{dc}a_1 \exp(-j\varphi)\exp(-j\alpha n) + I_{dc}a_1 \exp(j\varphi)\exp(j\alpha n)$, $c_2 = I_{dc}a_1 \exp(-j\varphi) \times \exp(-j\alpha n) + a_1^2 \exp(-j2\varphi)\exp(-j2\alpha n)$, and $c_3 = I_{dc}a_1 \exp(j\varphi)\exp(j\alpha n) + a_1^2 \exp(j2\varphi)$
$\exp(j2\alpha n)$.
Let, $E[I_{dc}^2 + c_1] = A_0^2$, $E[a_1^2 + c_2] = A_1^2$, and $E[a_1^2 + c_3] = A_2^2$. Therefore,

$$r(p) = A_0^2 + A_1^2 \exp(j\alpha p) + A_2^2 \exp(-j\alpha p) + \sigma^2 \delta_{p,0} \tag{A.7}$$

In Eq. (A.7), $\sigma^2 \delta_{p,0}$ is the expectation for the Gaussian noise $\eta(n)$ and is given by

$$E[\eta(k)\eta^*(l)] = \sigma^2 \delta_{k,l} \tag{A.8}$$

In practice, expectation E in Eq. (4.1) is computed by averaging over finite number of frames. If a large number of frames is taken for averaging, the exponential terms containing n in c_1, c_2, and c_3, will oscillate uniformly between 0 and 2π. In this limit, the expectation of c_1, c_2, and c_3 will approach zero because $\int_0^{2\pi} \exp(j\Psi)\, d\Psi = 0$. However, if finite number of frames are taken for averaging, expectation c_1, c_2, and c_3, will have a small finite value different from zero. Hence, for κ harmonics in the intensity, the final derivation of covariance of $I(n)$ is given by

$$r(p) = E[I(n)I^*(n-p)] = \sum_{n=0}^{2\kappa} A_n^2 exp(jf_n p) + \sigma^2 \delta_{p,0} \tag{A.9}$$

Bibliography

[1] A. Patil, R. Langoju, and P. Rastogi, "High-resolution frequency estimation technique for recovering phase distribution in interferometers," *Optics Letters*, vol. 30, pp. 391–393, 2005.

[2] S. Y. Kung, "A toeplitz approximation method and some applications," *in Proceedings of the International Symposium on the Mathematical Theory of Networks and Systems, Santa Monica CA*, vol. 5-7, pp. 262–266, 1981.

[3] D. C. Ghiglia and M. D. Pritt, *Two-dimensional phase unwrapping: theory, algorithms, and software.* New York: John Wiley and Sons Ltd, 1998.

[4] R. H. Hudgin, "Wave-front reconstruction for compensated imaging," *Journal of Optical Society of America*, vol. 67, pp. 375–378, 1977.

[5] R. J. Noll, "Phase estimates from slope-type wave-front sensors," *Journal of Optical Society of America*, vol. 68, pp. 139–140, 1978.

[6] D. L. Fried, "Least-squares fitting a wave-front distortion estimates to an array of phase-difference measurements," *Journal of Optical Society of America*, vol. 67, pp. 370–375, 1977.

[7] http://www.grc.nasa.gov/WWW/OptInstr/pdi.html.

[8] J. Szumowski, W. R. Coshow, F. Li, and S. F. Quinn, "Phase unwrapping in the three-point dixon method for fat suppression mr imaging," *Radiology*, vol. 192, pp. 555–561, 1994.

[9] D. Massonnet, M. Rossi, C. Carmona, F. Adragna, G. Peltzer, K. Feigl, and T. Rabaute", "The displacement field of the landers earthquake mapped by radar interferometry," *Nature*, vol. 364, pp. 138–142, 1993.

[10] F. Chen, G. M. Brown, and S. Mumin, "Overview of three-dimensional shape measurement using optical methods," *Optical Engineering*, vol. 39, pp. 10–22, 2000.

[11] M. C. Amann, M. L. T. Bosch, R. Mallylä, and M. Rioux, "Laser ranging: a critical review of usual techniques for distance measurement," *Optical Engineering*, vol. 40, pp. 10–19, 2001.

[12] N. Li, P. Cheng, M. A. Sutton, S. R. McNeill, and Y. J. Chao.

[13] C. Reich, R. Ritter, and J. Thesing, “3-d shape measurement of complex objects by combining photogrammetry and fringe projection,” *Optical Engineering*, vol. 39, pp. 224–231, 2000.

[14] K. Creath, *Phase-shifting holographic interferometry, Holographic Interferometry, P. K. Rastogi, ed.* Berlin: Springer-Series in Optical Sciences, 1994.

[15] T. Kreis, *Holographic Interferometry: Principles and Methods.* Berlin: Academie Verlag, 1996.

[16] R. Rodriguez-Vera, “Optical gauging of diffuse surfaces by electronic speckle contouring,” *Optics and Lasers in Engineering*, vol. 26, pp. 101–114, 1997.

[17] Y. Zou, H. Diao, X. Peng, and H. Tiziani, “Geometry for contouring by electronic speckle pattern interferometry based on shifting illumination beams,” *Applied Optics*, vol. 31, pp. 6616–6621, 1992.

[18] R. Rodriguez-Vera, D. Kerr, and F. Mendoza-Santoyo, “Electronic speckle contouring,” *Journal of Optical Society of America A*, vol. 9, pp. 2000–2008, 1992.

[19] C. Joenathan, B. Pfister, and H. J. Tiziani, “Contouring by electronic speckle pattern interferometry employing dual beam illumination,” *Applied Optics*, vol. 29, pp. 1905–1911, 1990.

[20] N. Abramson, “Holographic contouring by translation,” *Applied Optics*, vol. 15, pp. 1018–1022, 1976.

[21] X. Xinjin, J. T. Atkinson, M. J. Lalor, and D. R. Burton, “Three-map absolute moiré contouring,” *Applied Optics*, vol. 35, pp. 6990–6995, 1996.

[22] X. Xinjin, M. J. Lalor, D. R. Burton, and M. M. Shaw, “Four-map absolute distance contouring,” *Optical Engineering*, vol. 36, pp. 2517–2520, 1997.

[23] J. E. Sollid, “Holographic interferometry applied to measurements of small static displacements of diffusely reflecting surfaces,” *Applied Optics*, vol. 8, pp. 1587–1595, 1969.

[24] N. Abramson, “The holo-diagram: a practical device for making and evaluating holograms,” *Applied Optics*, vol. 8, pp. 1235–1240, 1969.

[25] R. Jones and C. Wykes, *Holographic and Speckle Interferometry.* Cambridge: Cambridge University Press, 1983.

[26] J. N. Butters and J. A. Leendertz, “Speckle pattern and holographic techniques in engineering metrology,” *Optics and Laser Technology*, vol. 3, pp. 26–30, 1971.

[27] K. A. Stetson and W. R. Brohinsky, “Electro-optic holography and its application to hologram interferometry,” *Applied Optics*, vol. 24, pp. 3631–3637, 1985.

[28] J. A. Leendertz, “Interferometric displacement measurement on scattering surfaces utilizing speckle effect,” *Journal of Physics E*, vol. 3, pp. 214–218, 1970.

[29] J. A. Leendertz and J. N. Butters, “An image-shearing speckle-pattern interferometer for measuring bending moments,” *Journal of Physics E*, vol. 6, pp. 1107–1110, 1973.

[30] Y. Y. Hung and C. Y. Liang, "Image-shearing camera for direct measurement of surface strains," *Applied Optics*, vol. 18, pp. 1046–1051, 1979.

[31] Y. Y. Hung and C. G. Taylor, "Measurement of slopes of structural defections by speckle-shearing interferometry," *Experimental Mechanics*, vol. 14, pp. 281–285, 1974.

[32] D. E. Duffy, "Moiré gauging of in-plane displacement using double aperture imaging," *Applied Optics*, vol. 14, pp. 1778–1781, 1972.

[33] Y. Hung, R. Rowlands, and I. Daniel, "Speckle-shearing interferometric technique: a full-field strain gauge," *Applied Optics*, vol. 14, pp. 618–622, 1975.

[34] M. B. North-Morris, J. VanDelden, and J. C. Wyant, "Phase-shifting birefringent scatterplate interferometer," *Applied Optics*, vol. 41, pp. 668–677, 2002.

[35] http://www.phase shift.com/products/interferometer.shtml.

[36] G. Brown and F. Chen, "Interference in design," *SPIE's Optical Engineering Magazine*, vol. November, pp. 16–18, 2002.

[37] L. R. Watkins, S. M. Tan, and T. H. Barnes, "Determination of interferometer phase distributions by use of wavelets," *Optics Letters*, vol. 24, pp. 905–907, 1999.

[38] K. Qian, H. S. Seah, and A. Asundi, "Instantaneous frequency and its application in strain extraction in moirë interferometry," *Applied Optics*, vol. 42, pp. 6504–6513, 2003.

[39] K. Qian, "Windowed fourier transform for fringe pattern analysis," *Applied Optics*, vol. 43, pp. 2695–2702, 2004.

[40] ——, "Windowed fourier transform for demodulation of carrier fringe patterns," *Optical Engineering*, vol. 43, pp. 1472–1473, 2004.

[41] K. A. Goldberg and J. Bokor, "Fourier-transform method of phase-shift determination," *Applied Optics*, vol. 40, pp. 2886–2894, 2001.

[42] C. S. Guo, Z. Y. Rong, J. L. He, H. T. Wang, L. Z. Cai, and Y. R. Wang, "Determination of global phase shifts between interferograms by use of an energy-minimum algorithm," *Applied Optics*, vol. 42, pp. 6514–6519, 2003.

[43] Y. Ishii, J. Chen, and K. Murata, "Digital phase-measuring interferometry with a tunable laser diode," *Optics Letters*, vol. 12, pp. 233–235, 1987.

[44] Y. Ishii and R. Onodera, "Phase-extraction algorithm in laser-diode phase-shifting interferometry," *Optics Letters*, vol. 20, pp. 1883–1885, 1995.

[45] K. Tatsuno and Y. Tsunoda, "Diode laser direct modulation heterodyne interferometer," *Applied Optics*, vol. 26, pp. 37–40, 1987.

[46] R. Onodera, Y. Ishii, N. Ohde, Y. Takahashi, and T. Yoshino, "Diode laser direct modulation heterodyne interferometer," *IEEE Journal of Lightwave Technology*, vol. 13, pp. 675–681, 1995.

[47] Y. Bitou, H. Inaba, F.-L. Hong, T. Takatsuji, and A. Onae, "Phase-shifting interferometry with equal phase steps by use of a frequency-tunable diode laser and a fabry-perot cavity," *Applied Optics*, vol. 44, pp. 5403–5407, 2005.

[48] M. Yokota, A. Asaka, and T. Yoshino, “Stabilization improvements of laser-diode closed-loop heterodyne phase-shifting interferometer for surface profile measurement,” *Applied Optics*, vol. 42, pp. 1805–1808, 2003.

[49] P. Carré, “Installation et utilisation du comparateur photoëelectrique et interfërentiel du bureau international des poids et mesures,” *Metrologia*, vol. 2, pp. 13–23, 1966.

[50] G. Stoilov and T. Dragostinov, “Phase-stepping interferometry: five-frame algorithm with an arbitrary step,” *Optics and Lasers in Engineering*, vol. 28, pp. 61–69, 1997.

[51] P. Hariharan, P. E. Ciddor, and M. Roy, “Improved switchable achromatic phase shifters, part 2,” *Optics and Lasers in Engineering*, vol. 44, pp. 105 603–1–105 603–4, 2005.

[52] B. K. A. Ngoi, K. Venkatakrishnan, and N. R. Sivakumar, “Phase-shifting interferometry immune to vibration,” *Applied Optics*, vol. 40, pp. 3211–3214, 2001.

[53] O. Y. Kwon, “Multichannel phase-shifted interferometer,” *Optics Letters*, vol. 9, pp. 59–61, 1984.

[54] R. Smythe and R. Moore, “Instantaneous phase measuring interferometry,” *Optical Engineering*, vol. 23, pp. 361–365, 1984.

[55] C. R. Mercer, K. Creath, and N. Rashidnia, “A phase-stepped point diffraction interferometer using liquid crystals,” *in* Interferometry VII: Techniques and Analysis*, M. Kujawinska, R. J. Pryputniewicz, and M. Takeda, eds., Proc. SPIE*, vol. 2544, pp. 87–93, 1995.

[56] H. Medecki, E. Tejnil, K. A. Goldberg, and J. Bokor, “Phase-shifting point diffraction interferometer,” *Optics Letters*, vol. 21, pp. 1526–1528, 1996.

[57] J. Huang, T. Honda, N. Ohyama, and J. Tsuiiuchi, “Fringe scanning scatter plate interferometer using a polarized light,” *Optics Communications*, vol. 68, pp. 235–238, 1988.

[58] D. C. Su and L. H. Shyu, “Phase-shifting scatter plate interferometer using a polarization technique,” *Journal of Modern Optics*, vol. 38, pp. 951–959, 1991.

[59] http://en.wikipedia.org/wiki/Piezoelectriceffect.html.

[60] Y. Surrel, “Design of algorithms for phase measurements by the use of phase stepping,” *Applied Optics*, vol. 35, pp. 51–60, 1996.

[61] K. Hibino, B. F. Oreb, D. I. Farrant, and K. G. Larkin, “Phase shifting for nonsinusoidal waveforms with phase-shift errors,” *Journal of Optical Society of America A*, vol. 12, pp. 761–768, 1995.

[62] J. Schwider, R. Burow, K. E. Elssner, J. Grzanna, R. Spolaczyk, and K. Merkel, “Digital wave-front measuring interferometry: some systematic error sources,” *Applied Optics*, vol. 22, pp. 3421–3432, 1983.

[63] Y. Zhu and T. Gemma, “Method for designing error-compensating phase-calculation algorithms for phase-shifting interferometry,” *Applied Optics*, vol. 40, pp. 4540–4546, 2001.

[64] P. Hariharan, B. F. Oreb, and T. Eiju, “Digital phase-shifting interferometry: a simple error-compensating phase calculation algorithm,” *Applied Optics*, vol. 26, pp. 2504–2506, 1987.

[65] J. Schwider, O. Falkenstorfer, H. Schreiber, and A. Zoller, "New compensating four-phase algorithm for phase-shift interferometry," *Optical Engineering*, vol. 32, pp. 1883–1885, 1993.

[66] Y. Surrel, "Phase stepping: a new self-calibrating algorithm," *Applied Optics*, vol. 32, pp. 3598–3600, 1993.

[67] J. van Wingerden, H. J. Frankena, and C. Smorenburg, "Linear approximation for measurement errors in phase shifting interferometry," *Applied Optics*, vol. 30, pp. 2718–2729, 1991.

[68] K. G. Larkin and B. F. Oreb, "Design and assessment of symmetrical phase-shifting algorithms," *Journal of Optical Society of America A*, vol. 9, pp. 1740–1748, 1992.

[69] Y. Y. Cheng and J. C. Wyant, "Phase-shifter calibration in phase-shifting interferometry," *Applied Optics*, vol. 24, pp. 3049–3052, 1985.

[70] B. Zhao, "A statistical method for fringe intensity-correlated error in phase-shifting measurement: the effect of quantization error on the n-bucket algorithm," *Measurement Science Technology*, vol. 8, pp. 147–153, 1997.

[71] B. Zhao and Y. Surrel, "Effect of quantization error on the computed phase of phase-shifting measurements," *Applied Optics*, vol. 36, pp. 2070–2075, 1997.

[72] R. Józwicki, M. Kujawinska, and M. Salbut, "New contra old wavefront measurement concepts for interferometric optical testing," *Optical Engineering*, vol. 31, pp. 422–433, 1992.

[73] P. de Groot, "Vibration in phase-shifting interferometry," *Journal of Optical Society of America A*, vol. 12, pp. 354–365, 1995.

[74] C. Rathjen, "Statistical properties of phase-shift algorithms," *Journal of Optical Society of America A*, vol. 12, pp. 1997–2008, 1995.

[75] P. L. Wizinowich, "Phase-shifting interferometry in the presence of vibration: a new algorithm and system," *Applied Optics*, vol. 29, pp. 3271–3279, 1990.

[76] C. Joenathan and B. M. Khorana, "Phase measurement by differentiating interferometric fringes," *Journal of Modern Optics*, vol. 39, pp. 2075–2087, 1992.

[77] K. Kinnstaetter, A. W. Lohmann, J. Schwider, and N. Streibl, "Accuracy of phase shifting interferometry," *Applied Optics*, vol. 27, pp. 5082–5089, 1988.

[78] C. J. Morgan, "Least squares estimation in phase-measurement interferometry," *Optics Letters*, vol. 7, pp. 368–370, 1982.

[79] J. E. Grievenkamp, "Generalized data reduction for heterodyne interferometry," *Optical Engineering*, vol. 23, pp. 350–352, 1984.

[80] P. de Groot, "Derivation of algorithms for phase-shifting interferometry using the concept of a data-sampling window," *Applied Optics*, vol. 34, pp. 4723–4730, 1995.

[81] K. Hibino, B. F. Oreb, D. I. Farrant, and K. G. Larkin, "Phase-shifting algorithms for nonlinear and spatially nonuniform phase shifts," *Journal of Optical Society of America A*, vol. 4, pp. 918–930, 1997.

[82] J. Schmit and K. Creath, “Extended averaging technique for derivation of error compensating algorithms in phase shifting interferometry,” *Applied Optics*, vol. 34, pp. 3610–3619, 1995.

[83] J. E. Grievenkamp and J. H. Bruning, *Phase shifting interferometry, Optical Shop Testing, D. Malacara ed.* New York: Wiley, 1992.

[84] C. Ai and J. C. Wyant, “Effect of spurious reflection on phase shift interferometry,” *Applied Optics*, vol. 27, pp. 3039–3045, 1988.

[85] B. V. Dorrío and J. L. fernández, “Phase-evaluation methods in whole-field optical measurement techniques,” *Measurement Science and Technology*, vol. 10, pp. R33–R55, 1999.

[86] C. P. Brophy, “Effect of intensity error correlation on the computed phase of phase-shifting interferometry,” *Journal of Optical Society of America A*, vol. 7, pp. 537–541, 1990.

[87] S. Ellingsrud and G. O. Rosvold, “Analysis of data-based tv-holography system used to measure small vibration amplitudes,” *Journal of Optical Society of America A*, vol. 9, pp. 237–251, 1992.

[88] G. T. Reid, “Automatic fringe pattern analysis: a review,” *Optics and Lasers in Engineering*, vol. 7, pp. 37–68, 1986.

[89] K. Qian, H. S. Seah, and A. Asundi, “Determination of the best phase step of the carrë algorithm in phase shifting interferometry,” *Measurement Science Technology*, vol. 11, pp. 1220–1223, 2000.

[90] G. Lai and T. Yatagai, “Generalized phase-shifting interferometry,” *Journal of Optical Society of America A*, vol. 8, pp. 822–827, 1991.

[91] K. G. Larkin, “A self-calibrating phase-shifting algorithm based on the natural demodulation of two-dimensional fringe patterns,” *Optics Express*, vol. 9, pp. 236–253, 2001.

[92] C. T. Farrell and M. A. Player, “Phase step measurement and variable step algorithms in phase-shifting interferometry,” *Measurement Science and Technology*, vol. 3, pp. 953–958, 1992.

[93] ——, “Phase-step insensitive algorithms for phase-shifting interferometry,” *Measurement Science and Technology*, vol. 5, pp. 648–652, 1994.

[94] F. L. Bookstein, “Fitting conic sections to scattered data,” *Computer Graphics and Image Processing*, vol. 9, pp. 56–71, 1979.

[95] A. Fitzgibbon, M. Pilu, and R. B. Fisher, “Direct least square fitting of ellipses,” *Pattern Analysis and Machine Intelligence*, vol. 21, pp. 474–480, 1999.

[96] L. Z. Cai, Q. Liu, and X. L. Yang, “Phase-shift extraction and wave-front reconstruction in phase-shifting interferometry with arbitrary phase steps,” *Optics Letters*, vol. 28, pp. 1808–1810, 2003.

[97] X. Chen, M. Gramaglia, and J. A. Yeazell, “Phase-shifting extraction and wave-front reconstruction in phase-shifting interferometry with arbitrary phase shifts,” *Applied Optics*, vol. 39, pp. 585–591, 2000.

[98] G. S. Han and S. W. Kim, “Numerical correction of reference phases in phase-shifting interferometry by iterative least-squares fitting,” *Applied Optics*, vol. 33, pp. 7321–7325, 1994.

[99] W. Jüptner, T. Kreis, and H. Kreitlow, “Automatic evaluation of holographic interferograms by reference beam phase shifting, in w. f. fagan. ed., industrial applications of laser technology,” *Proceedings of Society of Photonics and Instrumentation Engineering*, vol. 1553, pp. 569–582, 1991.

[100] P. K. Rastogi, “Phase shifting applied to four-wave holographic interferometers,” *Applied Optics*, vol. 31, pp. 1680–1681, 1992.

[101] ——, “Phase-shifting holographic moiré: phase-shifter error-insensitive algorithms for the extraction of the difference and sum of phases in holographic moirë,” *Applied Optics*, vol. 32, pp. 3669–3675, 1993.

[102] P. K. Rastogi, M. Spajer, and J. Monneret, “In-plane deformation measurement using holographic moiré,” *Optics and Lasers in Engineering*, vol. 2, pp. 79–103, 1981.

[103] D. B. Neümann, “Comparative holography,” *Tech. Digest, testing Meeting on Hologram Interferometry and Speckle Metrology, Optical Society of America*, pp. Paper MB2–1, 1980.

[104] Z. Füzessy and F. Gyímesi, “Difference holographic interferometry: displacement measurement,” *Optical Engineering*, vol. 23, pp. 780–783, 1984.

[105] P. K. Rastogi, “Comparative holographic moiré interferometry in real time,” *Applied Optics*, vol. 23, pp. 924–927, 1984.

[106] ——, “Comparative holographic interferometry: a nondestructive inspection system for detection of flaws,” *Experimental Mechanics*, vol. 25, pp. 325–337, 1985.

[107] Z. Wang and B. Han, “Advanced iterative algorithm for phase extraction of randomly phase-shifted interferograms,” *Optics Letters*, vol. 29, pp. 1671–1673, 2004.

[108] A. Patil, R. Langoju, and P. Rastogi, “An integral approach to phase shifting interferometry using a super resolution frequency estimation method,” *Optics Express*, vol. 12, pp. 4681–4697, 2004.

[109] J. J. Fuchs, “Estimating the number of sinusoids in additive white noise,” *IEEE Transactions on Acoustics, Speech, and Signal Processing*, vol. 36, pp. 1846–1853, 1988.

[110] K. B. Hill, S. A. Basinger, R. A. Stack, and D. J. Brady, “Noise and information in interferometric cross correlators,” *Applied Optics*, vol. 36, pp. 3948–3958, 1997.

[111] M. Dendrinos, S. Bakamidis, and G. Carayannis, “Speech enhancement from noise: A regenerative approach,” *Speech Communication*, vol. 10, pp. 45–57, 1991.

[112] P. C. Hansen and S. H. Jensen, “Fir filter representation of reduced-rank noise reduction,” *IEEE Transaction on Signal Processing*, vol. 46, pp. 1737–1741, 1998.

[113] K. M. Hoffman and R. Kunze, *Linear Algebra, 2nd ed.* New Jersey: Englewood Cliffs: Prentice Hall, 1971.

[114] M. Marcus and H. Minc, *Vandermonde Matrix, in A Survey of Matrix Theory and Matrix Inequalities.* New York: Dover, 1992.

[115] A. Patil, R. Langoju, and P. Rastogi, "Model based processing of holographic moiré," *Optics Letters*, vol. 30, pp. 2870–2872, 2005.

[116] R. O. Schmidt, "Multiple emitter location and signal parameter estimation," *in Proceedings RADC, Spectral Estimation Workshop, Rome, NY*, pp. 243–258, 1979.

[117] G. Bienvenu, "Influence of the spatial coherence of the background noise on high resolution passive methods," *in Proceedings of the International Conference on Acoustics, Speech, and Signal Processing, Washington, DC*, pp. 306–309, 1979.

[118] T. Söderström and P. Stoica, "Accuracy of high-order yule-walker methods for frequency estimation of complex sine waves," *IEEE Proceedings-F*, vol. 140, pp. 71–80, 1993.

[119] A. Patil and P. Rastogi, "Subspace-based method for phase retrieval in interferometry," *Optics Express*, vol. 13, pp. 1240–1248, 2005.

[120] B. D. Rao and K. V. S. Hari, "Weighted subspace methods and spatial smoothing: analysis and comparison," *IEEE Transactions on Signal Processing*, vol. 41, pp. 788–803, 1993.

[121] A. Patil and P. Rastogi, "Phase determination in holographic moiré in presence of nonsinusoidal waveforms and random noise," *Optics Communications*, vol. 257, pp. 120–132, 2006.

[122] M. Kaveh and A. Barabell, "The statistical performance of the music and the minimum-norm algorithms in resolving plane waves in noise," *IEEE Transactions on Acoustics, Speech, and Signal Processing*, vol. ASSP-34, pp. 331–341, 1986.

[123] P. Stoica and R. Moses, *Introduction to Spectral Analysis.* New Jersey: Prentice Hall, 1997.

[124] A. Patil and P. Rastogi, "A min-norm approach for estimating phase distribution in an interferogram," *accepted for publication in Journal of Modern Optics*, 2006.

[125] ——, "Estimation of multiple phases in holographic moiré in presence of harmonics and noise using minimum-norm algorithm," *Optics Express*, vol. 13, pp. 4070–4084, 2005.

[126] R. Roy and T. Kailath, "Esprit-estimation of signal parameters via rotational invariance techniques," *IEEE Transactions on Acoustics, Speech, and Signal Processing*, vol. 37, pp. 984–995, 1989.

[127] A. Patil and P. Rastogi, "Phase shifting interferometry using covariance-based method," *Applied Optics*, vol. 44, pp. 5778–5785, 2005.

[128] ——, "Rotational invariance approach for the evaluation of multiple phases in interferometry in presence of nonsinusoidal waveforms and noise," *Journal of Optical Society of America A*, vol. 22, pp. 1918–1928, 2005.

[129] P. Stoica and A. Nehorai, "Music, maximum likelihood, and cramér-rao bound," *IEEE Trans. Acoust. Speech, Signal Processing*, vol. 37, pp. 720–741, 1989.

[130] B. Raphael and I. F. C. Smith, "A direct stochastic algorithm for global search," *Applied Mathematics and Computation*, vol. 146, pp. 729–758, 2003.

[131] K. C. Sharman and G. D. McClurkin, "Genetic algorithms for maximum likelihood parameter estimation," *Proc. IEEE Int. Conf. Acoust., Speech, Signal Processing*, vol. ICASSP-89, pp. 2716–2719, 1989.

[132] K. C. Sharman, "Maximum likelihood parameter estimation by simulated annealing," *Proc. IEEE Int. Conf. Acoust., Speech, Signal Processing*, vol. ICASSP-88, pp. 2741–2744, 1988.

[133] A. Patil, R. Langoju, and P. Rastogi, "Phase shifting interferometry using a robust parameter estimation method," *accepted for publication in Optics and Lasers in Engineering*, 2007.

[134] A. Patil and P. Rastogi, "Maximum-likelihood estimator for dual phase extraction in holographic moiré," *Optics Letters*, vol. 30, pp. 2227–2229, 2005.

[135] A. Patil, R. Langoju, and P. Rastogi, "A state-space approach in phase shifting interferometry," *accepted for publication in Optics Communications*, 2006.

[136] D. C. Rife and R. R. Boorstyn, "Single-tone parameter estimation from discrete-time observations," *IEEE Transactions on Information Theory*, vol. IT-20, pp. 591–598, 1974.

[137] http://mathworld.wolfram.com/VandermondeMatrix.html.

[138] A. Patil, B. Raphael, and P. Rastogi, "Generalized phase-shifting interferometry using a direct stochastic algorithm for global search," *Optics Letters*, vol. 29, pp. 1381–1383, 2004.

[139] B. Gutmann and H. Weber, "Phase-shifter calibration and error detection in phase-shifting applications: a new method," *Applied Optics*, vol. 32, pp. 7624–7631, 1998.

[140] J. Schmit and K. Creath, "Some new error-compensating algorithms for phase-shifting interferometry," *Optical Fabrication and Testing Workshop*, vol. 13 of OSA Technical Digest Series, Optical Society of America, Washington, DC., pp. PD–4, 1994.

[141] P. de Groot, "Long-wavelength laser diode interferometer for surface flatness measurement, in: Optical measurements and sensors for the process industries, in: C. gorecki, r. w. preater (eds.)," *Proc. Soc. Photo Opt. Instrum. Eng.*, vol. 2248, pp. 136–140, 1994.

[142] A. Kangas and T. S. P. Stoica, "Finite sample and modelling error effects on esprit and music direction estimators," *IEE Proceddings on Radar, Sonar and Navigation*, vol. 141, pp. 249–255, 1994.

Abhijit Patil

Applied Computing and Mechanics Laboratory,
Swiss Federal Institute of Technology, Lausanne,
Switzerland-1015.
abhijit.patil@epfl.ch

Personal Details:

Born:	19 January 1975.
Citizenship:	Indian

Education:

Ph. D.	Swiss Federal Institute of Technology
M. Tech.	Electrical Engineering (Instrumentation & Control), Indian Institute of Technology, Bombay, 2000. Grade: *9.01/10.*
B. E.	Instrumentation Engineering, Pune University, India. Grade: *First Class*

Professional Experience:

2002-Present	Research Assistant, Swiss Federal Institute of Technology.
2001–2002	Research Assistant, Nanyang Technological University, Singapore.
2000–2001	Trainee Engineer, Larsen & Tubro Ltd. India
1998–2000	Teaching Assistant, Indian Institute of Technology, Bombay.

Achievement:

- All India Rank 7th in Graduate Aptitude Test in Engineering 1998 for admission to Indian Institute of Technology.
- Swiss National Science Foundation Grant for research in the field of phase measurement techniques

Other Activities:

- Guest Editor for special issue on phase measurement in Optics & Lasers in Engineering.
- Reviewed several papers in Optics & Lasers in Engineering and Optics Communications.

Computer Skills:

C/C++, MATLAB, MAPLE, MATHEMATICA

Languages:

English, Hindi, Marathi

Publications in Peer-Reviewed Journals:

1. A. Patil, R. Langoju, and P. Rastogi, "A state space approach in phase shifting interferometry," Optics Communications **263**, 281-288 (2006).

2. R. Langoju, A. Patil, and P. Rastogi, "Chirp estimation method in phase shifting interferometry," Optics Letters **31**, 1982-1984 (2006).

3. R. Langoju, A. Patil, and P. Rastogi, "Phase-shifting interferometry in the presence of nonlinear phase steps, harmonics, and noise," Optics Letters **31**, 1058-1060 (2006).

4. A. Patil and P. Rastogi, "Phase determination in holographic moiré in presence of nonsinusoidal waveforms and random noise," Optics Communications **257**, 120-132 (2006).

5. A. Patil and P. Rastogi, "A min-norm approach for estimating phase distribution in an interferogram," Journal of Modern Optics **53**, 283-293 (2006).

6. A. Patil, R. Langoju, and P. Rastogi, "Constraints in dual-phase shifting interferometry," Optics Express **14**, 88-102 (2006), http://www.opticsexpress.org/abstract.cfm?URI=OPEX-14-1-88.

7. A. Patil, B. Raphael, and P. Rastogi, "Introduction of stochastic methods to phase-shifting interferometry," Journal of Modern Optics **52**, 33-44 (2005).

8. A. Patil and P. Rastogi, "Nonlinear regression technique applied to generalized phase-shifting interferometry," Journal of Modern Optics **52**, 573-582 (2005).

9. A. Patil, B. Raphael, and P. Rastogi, "A stochastic method for generalized data reduction in holographic moiré," Optics Communications **248**, 395-405 (2005).

10. A. Patil, R. Langoju, and P. Rastogi, "High-resolution frequency estimation technique for recovering phase distribution in interferometers," Optics Letters **30**, 391-393 (2005).

11. A. Patil and P. Rastogi, "Maximum-likelihood estimator for dual phase extraction in holographic moiré," Optics Letters **30**, 2227-2229 (2005).

12. A. Patil, R. Langoju, and P. Rastogi, "Model based processing of holographic moiré," Optics Letters **30**, 2870-2872 (2005).

13. A. Patil and P. Rastogi, "Subspace-based method for phase retrieval in interferometry," Optics Express **13**, 1240-1248 (2005), http://www.opticsexpress.org/abstract.cfm?URI=OPEX-13-4-1240.

14. A. Patil and P. Rastogi, "Estimation of multiple phases in holographic moiré in presence of harmonics and noise using minimum-norm algorithm," Optics Express **13**, 4070-4084 (2005), http://www.opticsexpress.org/abstract.cfm?URI=OPEX-13-11-4070.

15. A. Patil and P. Rastogi, "Rotational invariance approach for the evaluation of multiple phases in interferometry in presence of nonsinusoidal waveforms and noise," Journal of Optical Society of America A **22**, 1918-1928 (2005).

16. A. Patil and P. Rastogi, "Phase shifting interferometry by a covariance-based method," Applied Optics **44**, 5778-5785 (2005).

17. R. Langoju, A. Patil, and P. Rastogi, "Super-resolution Fourier transform method in phase shifting interferometry," Optics Express **13**, 7160-7173 (2005) http://www.opticsinfobase.org/abstract.cfm?URI=oe-13-18-7160

18. R. Langoju, A. Patil, and P. Rastogi, "Resolution-enhanced Fourier transform method for the estimation of multiple phases in interferometry," Optics Letters **30**, 3326-3328 (2005).

19. Patil A. and Rastogi P., "Approaches in generalized phase shifting interferometry," Optics and Lasers in Engineering **43**, 475-490 (2005).

20. A. Patil, B. Raphael, and P. Rastogi, "Generalized phase-shifting interferometry using a direct stochastic algorithm for global search," Optics Letters **29**, 1381-1383 (2004).

21. A. Patil, R. Langoju, and P. Rastogi, "An integral approach to phase shifting interferometry using a super-resolution frequency estimation method," Optics Express **12**, 4681-4697 (2004), http://www.opticsexpress.org/abstract.cfm?URI=OPEX-12-20-4681.

Publications in Peer-Reviewed Journals (in Press):

1. A. Patil, R. Langoju, and P. Rastogi, "Phase Shifting Interferometry using a Robust Parameter Estimation Method," Optics and Lasers in Engineering (in Press) 2006.

2. R. Langoju, A. Patil, and P. Rastogi, "A novel approach for characterizing the non-linear phase steps of the PZT in interferometry," Optics and Lasers in Engineering (in press) 2006.

3. R. Langoju, A. Patil, and P. Rastogi, "Predicting phase step in phase shifting interferometry in the presence of harmonics and noise," Applied Optics (in press) 2006.

Publications in Peer-Reviewed Journals (accepted):

1. R. Langoju, A. Patil, and P. Rastogi, "Accurate nonlinear phase step estimation in phase shifting interferometry," Optics Communications, (accepted) 2006.

2. R. Langoju, A. Patil, and P. Rastogi, "Estimation of multiple phases in interferometry in the presence of non-linear arbitrary phase steps," Optics Express, (accepted) 2006.

Publications in Peer-Reviewed Journals (submitted):

1. A. Patil, R. Langoju, and P. Rastogi, "Statistical study and experimental verification of high resolution methods in phase shifting interferometry," Journal of Optical Society of America A, (submitted) 2006.

2. R. Langoju, A. Patil, and P. Rastogi, “Real time phase step estimation in phase shifting interferometry,” Optical Engineering, (submitted) 2006.

Publications in Conferences:

1. Ganesha Udupa, Bryan K. Ngoi, H. C. F. Goh, M. N. Yusoff, A. V. Patil, “Characterization of nanodefects in silicon wafers by white light phase shifting interferometry”, Proc. SPIE Vol. **4829**, (341-343), 19th Congress of the International Commission for Optics: Optics for the Quality of Life; Giancarlo C. Righini, Anna Consortini; Eds.(2003).

Guest Editorials:

1. A. Patil and P. Rastogi, “Moving ahead with phase: Guest Editorial,” Optics and Lasers in Engineering (in Press) 2006.